Downloaded from orbit.dtu.dk on: Apr 29, 2024

DTU Library

Automated Image-Based Procedures for Adaptive Radiotherapy

Bjerre, Troels

Publication date:
2013

Document Version
Publisher's PDF, also known as Version of record

Link back to DTU Orbit

Citation (APA):
Bjerre, T. (2013). *Automated Image-Based Procedures for Adaptive Radiotherapy*. Technical University of Denmark. PHD-2013 No. 305

General rights
Copyright and moral rights for the publications made accessible in the public portal are retained by the authors and/or other copyright owners and it is a condition of accessing publications that users recognise and abide by the legal requirements associated with these rights.

- Users may download and print one copy of any publication from the public portal for the purpose of private study or research.
- You may not further distribute the material or use it for any profit-making activity or commercial gain
- You may freely distribute the URL identifying the publication in the public portal

If you believe that this document breaches copyright please contact us providing details, and we will remove access to the work immediately and investigate your claim.

Automated Image-Based Procedures for Adaptive Radiotherapy

Troels Bjerre

Kongens Lyngby 2013
PhD-2013-305

Technical University of Denmark
Department of Applied Mathematics and Computer Science
Matematiktorvet, Bygning 303B, DK-2800 Kongens Lyngby, Denmark
Phone +45 45253031, Fax +45 45881399
compute@compute.dtu.dk
www.compute.dtu.dk PhD-2013-305

Summary (English)

Fractionated radiotherapy for cancer treatment is a field of constant innovation. Developments in dose delivery techniques have made it possible to precisely direct ionizing radiation at complicated targets. In order to further increase tumour control probability (TCP) and decrease normal-tissue complication probability (NTCP), margins used to account for interfraction and intrafraction anatomical changes and motion need to be reduced. This can only be achieved through proper treatment plan adaptations and intrafraction motion management.

This thesis describes methods in support of image-based treatment replanning and real-time intrafraction guidance techniques. The selected contributions detail a number of findings and techniques, in particular:

- For ten head & neck cancer patients, changes in tumour density were well described by linear functions with patient-specific slope and intercept. This is of particular interest for proton therapy as delivered dose to a tissue and calculated dose distributions rely on density. Furthermore, tumour density changes might be indicative of treatment response.
- It is demonstrated how spatially varying elasticity parameters can be employed in image registration to encourage bone rigidity and local tissue volume change only in the gross tumour volume and the lungs. This is highly relevant in adaptive radiotherapy when modelling significant tumour volume changes.
- It is described how cone beam CT reconstruction can be modelled as a deformation of a planning CT scan of the same patient, using a non-

parametric diffusion based deformation model, opening the door to the use of a number of advanced non-parametric algorithms. An advantage of reconstruction by deformation is that no subsequent image registration is needed in order to obtain the deformation which can be employed for contour propagation in adaptive radiotherapy.

- MRI-radiotherapy devices have the potential to offer near real-time intra-fraction imaging without any additional ionising radiation. It is detailed how the use of multiple, orthogonal slices can form the basis for reliable 3D soft tissue tracking.

Summary (Danish)

Fraktioneret stråleterapi til behandling af cancer er et felt med konstant innovation. Udviklingen i dosisplanlægning og behandlingsteknik har gjort det muligt at levere ioniserende stråling præcist til komplicerede mål. For at øge chancen for tumorkontrol yderligere og sænke sandsynligheden for normalvævskomplikationer er det nødvendigt at reducere margener for inter- og intrafraktions anatomiske ændringer og bevægelse. Det kan kun opnås gennem passende ændringer af behandlingsplanen undervejs i behandlingsforløbet og håndtering af intrafraktionsbevægelser.

Denne afhandling beskriver metoder, der understøtter billedbaseret genplanlægning af behandling og realtids, intrafraktions-tilretningsteknikker. De udvalgte bidrag beskriver en række resultater og teknikker, deriblandt:

- For ti hoved-halscancerpatienter var ændringer i tumordensitet velbeskrevet af lineære funktioner med patientspecifik hældning og skæring. Dette er særligt relevant for protonterapi, hvor den leverede dosis til et væv og dosedistributioner, afhænger af densiteten. Derudover kan ændringer i tumordensitet, muligvis være indikativt for behandlingsrespons.
- Det bliver demonstreret, hvordan spatielt varierende elasticitetsparametre kan benyttes i billedregistrering, til at tilskynde knoglerigiditet samt lokale ændringer i vævsvolumen begrænset til tumorvolumener og lunger. Dette er meget relevant i adaptiv stråleterapi, når store volumenændringer modelleres.
- Det bliver beskrevet hvordan cone beam CT rekonstruktion kan modelleres som deformation af et planlægningsscan af den samme patient ved

brug af en ikke-parametrisk, difussionsbaseret deformationsmodel, hvilket åbner op for at bruge et antal avancerede ikke-parametriske algoritmer. En fordel ved rekonstruktion ved deformation er, at ingen efterfølgende billedregistrering er nødvendig for at estimere denne deformation, der kan bruges til propagering af indtegninger.

- MRI-stråleterapiapparater har potentialet til at muliggøre lav-latens intra-fraktions-billedoptagelse uden yderligere stråledosis. Det beskrives hvordan brugen af multiple ortogonale billedplaner kan udgøre en basis for '3D tracking' af blødt væv.

Preface

This thesis was prepared at the Department of Applied Mathematics and Computer Science, Technical University of Denmark (DTU) and the Department of Radiation Oncology, Rigshospitalet, University of Copenhagen, Denmark, in fulfilment of the requirements for acquiring a PhD degree. The project was funded by DTU, Rigshospitalet and The Lundbeck Foundation Centre for Interventional Research in Radiation Oncology (CIRRO).
The project was supervised by Professor Rasmus Larsen, Department of Applied Mathematics and Computer Science, DTU; Professor Lena Specht, Department of Oncology, Rigshospitalet, and Faculty of Health Sciences, University of Copenhagen; Dr. Marianne Aznar and Dr. Per Munck af Rosenschöld, Department of Radiation Oncology, Rigshospitalet, University of Copenhagen, and the Niels Bohr Institute, University of Copenhagen.
Part of the research was conducted at The Radiation Physics Laboratory, The University of Sydney, Sydney, Australia under the supervision of Professor Paul Keall.
This thesis comprises an introductory part and presents selected contributions representing scientific research carried out during the PhD project.

Lyngby, 01-October-2013

Troels Bjerre

Acknowledgements

I would like to thank my supervisors Rasmus, Marianne, Lena, and Per for their guidance throughout the extent of the project. In addition I would like to thank Paul Keall for his guidance and hospitality during my research stay at The University of Sydney. Furthermore I would like to thank Sjoerd Crijns from UMC Utrecht for assisting with MRI data acquisition. A special thanks goes to Mads Fogtmann who has been supportive, helpful, and have always had an answer to my questions. Finally, I would like to thank my family and friends for their understanding and support.

Contents

Summary (English) i

Summary (Danish) iii

Preface v

Acknowledgements vii

Acronyms and Abbreviations xiii

I Introduction 1

1 Background 5
1.1 Radiotherapy for treatment of cancer 6
1.1.1 Tumour formation 6
1.1.2 Tumour metastasis 7
1.1.3 Therapy modalities 8
1.1.4 Radiotherapy 9
1.2 Imaging modalities for radiotherapy planning 10
1.2.1 Computed tomography (CT) 11
1.2.2 Positron emission tomography (PET) and PET-CT fusion 14
1.2.3 Magnetic resonance imaging (MRI) and PET-MRI fusion 15
1.3 Radiotherapy planning 16
1.3.1 Delineation of volumes of interest (VOI) 18
1.3.2 Plan optimisation 19
1.4 Imaging modalities available in treatment room 21
1.4.1 CBCT 21
1.4.2 CT on rails and integrated CT systems 23

1.4.3 Integrated MRI-radiotherapy systems 24
1.5 Patient setup 25

2 Interfraction treatment plan adaptations 27
2.1 Library planning 29
2.2 Radiation induced tumour volume changes 31
2.3 Deformable intrasubject image registration 32
2.3.1 Parametric transformation models 33
2.3.2 Non-parametric transformation models 33
2.3.3 Objective functions 33
2.3.4 Regularisation 34
2.4 Treatment plan adaptations 35

3 Intrafraction motion management 41
3.1 Marker-based motion management 42
3.2 4D CT imaging and tomographic image registration 45
3.3 MRI low-latency guidance 46

4 Contributions 49

5 Discussion and conclusion 53

II Selected Peer-Reviewed Contributions 55

6 Modeling tumor size and density changes during chemoradiation therapy for head and neck cancer 57
6.1 Introduction 58
6.2 Methods 59
6.2.1 Data 59
6.2.2 Repeated measurements model 60
6.2.3 Model selection for ordinary least squares and repeated measurements analysis 63
6.3 Results 64
6.3.1 Investigation of tumor volume changes 64
6.3.2 Investigation of tumor radiodensity changes 65
6.3.3 Connection between tumor volume and radiodensity changes 69
6.4 Discussion & Conclusions 69

7 Spatially Varying Riemannian Elasticity Regularization: Application to Thoracic CT Registration in Image-Guided Radiotherapy 73
7.1 Introduction 74
7.2 Data 75
7.2.1 POPI-model: 4DCT 75

7.2.2 Hodgkin lymphoma case: Pre- and post-chemo computed tomography (CT) . . . 75
7.3 Method . . . 76
7.4 Results . . . 77
7.4.1 POPI-model . . . 77
7.4.2 Pre- and post-chemo CT . . . 77
7.5 Discussion & Conclusion . . . 80

8 Demons Registration of CT Volume and CBCT Projections for Adaptive Radiotherapy: Avoiding CBCT Reconstruction 83

9 Three-dimensional MRI-linac intra-fraction guidance using multiple orthogonal cine-MRI planes 87
9.1 Introduction . . . 88
9.2 Methods . . . 89
9.2.1 Qualitative evaluation . . . 91
9.2.2 Quantitative evaluation . . . 92
9.2.3 Data for qualitative evaluation . . . 92
9.2.4 Data for quantitative evaluation . . . 93
9.3 Results . . . 93
9.3.1 Qualitative evaluation . . . 93
9.3.2 Quantitative evaluation . . . 94
9.4 Discussion & Conclusions . . . 96

References 101

Acronyms and Abbreviations

ART	adaptive radiotherapy	6
BEV	beam's eye view	21
CBCT	cone beam CT	21
CPU	central procession unit	
CT	computed tomography	xi
CTV	clinical target volume	18
DIR	deformable image registration	32
DMLC	dynamic multileaf collimator	44
DNA	deoxyribonucleic acid	5
DOM	deformation from orbiting views	45
DVH	dose-volume histogram	19
EM	electromagnetic	43
EPID	electronic portal imaging device	21
FDG	2-deoxy-2-(^{18}F)fluoro-D-glucose	15
FFD	free-form deformation	33
fMRI	functional MRI	16
GPU	graphics procession unit	
GTV	gross tumour volume	18
Gy	Gray	6

HL	Hodgkin lymphoma	74
HNCA	head & neck cancer	27
HU	Hounsfield units	74
IGRT	image-guided radiation therapy	35
IMRT	intensity-modulated radiotherapy	19
IS	inferior-superior	89
linac	linear particle accelerator	10
MLC	multileaf collimator	10
MRI	magnetic resonance imaging	10
MRS	magnetic resonance spectroscopy	16
NCC	normalised cross-correlation	33
NTCP	normal-tissue complication probability	5
OAR	organs at risk	5
PA	posterior-anterior	89
PCA	principal component analysis	29
PET	positron emission tomography	
PET/CT	positron emission tomography/computed tomography	6
PET/MRI	positron emission tomography/magnetic resonance imaging	10
PRV	planning organs at risk volume	18
PTV	planning target volume	18
RF	radio frequency	15
RL	right-left	89
RT	radiotherapy	29
RTS	Respiratory Tracking System	42
SAD	sum of absolute differences	33
SAM	segment aperture morphing	38
SNR	signal-to-noise ratio	21
SSD	sum of squared differences	33
SWO	segment weight optimisation	38
TCP	tumour control probability	5
TRE	target registration error	74

Part I

Introduction

For every complex problem
there is an answer that is
clear, simple, and wrong.

H. L. MENCKEN

Chapter 1

Background

Cancer is a disease involving unregulated cell growth, tumour invasion of healthy tissue and metastatic spread to secondary sites. Depending on the site and stage, cancer may cause tissue destruction, organ compression, organ obstruction, infection, anaemia, pain and for many patients even death. Cancer remains one of the leading causes of death in both economically developed and developing countries. In 2008 the global incidence of cancer was approximately 12.7 million with a mortality of 7.6 million. Among females, breast cancer is the leading cause of cancer deaths worldwide, accounting for 23% of all cancer cases and 14% of the total cancer deaths. Lung cancer is the leading cause of cancer death among males, accounting for 17% of all cancer cases and 23% of the total cancer deaths. (Jemal et al. 2011)

In radiotherapy for treatment of cancer, targeted ionizing radiation is used to control or kill malignant tumour cells. Ionizing radiation inflicts damage to the genetic material of exposed cells, leading to cellular death. The tumour control probability (TCP) is proportional to the delivered radiation dose, within certain dose intervals (Verellen et al. 2007). Escalation of dose to the tumour volume is limited by the fact that radiation is also deposited in the surrounding healthy tissue and nearby organs at risk (OAR). Exploiting the fact that the capability of normal tissue to repair deoxyribonucleic acid (DNA) damage induced by low radiation doses is greater than that of tumour tissue, the long term normal-tissue complication probability (NTCP) is reduced by treatment fractionation. In

fractionated radiotherapy, the total dose is typically delivered in 25-35 fractions of 1.8-2.0 Gray (Gy) per day, allowing for the surrounding healthy tissue and OAR to repair some of the damage caused by the radiation between fractions.

The aim of radiotherapy is to deliver a prescribed dose, e.g. 70 Gy, to tumour cells while minimising the dose to all OAR. Radiotherapy is usually planned on the base of a positron emission tomography/computed tomography (PET/CT) scan that offers both anatomical and biological/functional information. This treatment plan is followed during delivery of each successive treatment fraction, making daily setup of a patient's position critical to accurate delivery. Prior to each daily fraction, image-guidance is employed to position the patient according to his/her treatment planning PET/CT scan in an effort to avoid changes to the prescribed dose distribution. Exact positioning, however, may not account for possible interfraction changes in the anatomy, including general weight loss, tumour shrinkage/progression, oedema, bladder filling, bowel peristalsis, etc. These changes are traditionally accounted for by adding appropriate margins to the target volume. Wider margins ensure that the prescribed dose is delivered to the intended volume but also inevitably increases dose to OAR, thereby increasing the NTCP.

In adaptive radiotherapy (ART) the aim is to decrease the need for wide margins by adapting the treatment plan to changes in anatomy as they occur during a course of fractionated radiotherapy. ART employs image-based procedures for interfraction treatment plan adaptations as well as for intrafraction motion compensation.

The following sections introduce adaptive radiotherapy as well as key concepts relevant to the field.

1.1 Radiotherapy for treatment of cancer

1.1.1 Tumour formation

Cancer is a disease characterised by unregulated (autonomous) cell growth, invasion and disruption of nearby tissues, and lymphogeneous or haematogenous spread to distant parts of the body (metastasis). Cancer is caused by changes of cell genes that regulate cell growth and differentiation. Two types of genes may be altered: proto-oncogenes and/or tumour supressor genes. When altered, proto-oncogenes may become oncogenes which encode proteins that promote cell division and survival. Over-expression or amplification of these genes promote

tumour formation. Tumour supressor genes inhibit cell division and survival. Mutations to these genes may lead to inactivation and promotion of tumour formation. In many cancers the TP53 gene that encodes tumour protein 53 (p53) is altered. Cells with a defective p53 tumour suppressor gene do not undergo programmed cell death (apoptosis). Typically, it takes more than a single genetic change for a cell to become malignant. (Specht 2012)

Genetic changes leading to tumour formation can be caused by the following (Specht 2012):

Chemical agents Tobacco smoking is the cause of most lung cancers, but also associated with oral, nasal, pharyngeal, laryngeal, kidney, bladder and pancreatic cancers. Other noteworthy chemicals associated with cancer include asbestos (mesothelioma), aniline dye (bladder cancer), wood dust (sino nasal cancer), aflatoxin (liver cancer), alkylating cytostatics (leukemia).

Physical agents Ionizing radiation increases the risk of cancers in the irradiated area. Sources include background radiation, mainly from radon, and X-ray imaging. Ultraviolet light increases risk of melanomas and skin cancer. Chronic mechanical irritation of mucous membranes (prosthetics in the oral cavity, kidney stones, gall stones, etc.) or chronic inflammation (chronic ulcerative colitis, leg ulcers, etc.) can also lead to cancer.

Infections Human papillomavirus (HPV) is the cause of 70% of cervical cancers as well as oropharyngeal cancers. Epstein-Barr virus is contributory factor in the development of B cell lymphomas, such as Hodgkin's lymphoma and naspharyngeal carcinomas. Hepatitis B and C can cause hepatocellular carcinomas.

Immunological factors Immunosuppression due to e.g. AIDS or the use of immunosuppressive drugs following organ transplants can contribute to the development of especially lymphomas.

Hereditary factors A number of genetic defects increase the risk of certain cancer types, e.g. mutations of the BRCA1/BRCA2 genes (breast cancer), mutations of the APC gene (colon cancer).

1.1.2 Tumour metastasis

Metastasis is the spread of neoplastic cells from a primary malignant tumour to a non-adjacent organ or part of the body, where they become established as

secondary tumours. The most important types of metastases are (Nowak et al. 2004)

Haematogenous metastasis Aggressively invasive tumours easily penetrate the thin endothelial cell layer of capillaries and veins. The low intercellular adhesiveness of tumours allow cell emboli to separate from the tumour and be carried in the blood stream. The emboli are ultimately carried to the pulmonary or other organ's capillaries where they lodge and develop as secondary tumours.

Lymphogeneous metastasis When invasive tumours penetrate lymphatic vessels and emboli dislodge, they can lodge in the reticular tissue of upstream lymph nodes.

Metastasis via body cavities Tumour invasion can penetrate the surface of the organ and spread to other organs through body cavities such as the peritoneum. Abdominal tumour spread is aided by gravity as well as peristaltic and diaphragm movement.

1.1.3 Therapy modalities

In general, treatment depends on cancer type, and spread. If feasible, therapy is curatively intended. In cases where cancer is widespread and cure is not possible, therapy is palliative. Antitumour therapy focuses on the removal or destruction of the tumour. All techniques aim to maximise tumour cell killing while minimising normal tissue damage. The most important therapy modalities are (Nowak et al. 2004; Specht 2012):

Surgery Surgery physically removes the involved tissues from the body. For clearly demarcated benign tumours in non-critical tissues surgery is a curative treatment. For malignant tumours with irregular margins, invasive growth patterns and/or metastatic involvement, complete surgical removal is more complicated and adjuvant therapy might be necessary for curative treatment.

Radiotherapy In radiotherapy, ionizing radiation is used to induce tumour cell death. For clinical use, electromagnetic radiation (X-ray or Gamma radiation) or particle radiation (electron, beta particle, or proton radiation) are employed.

Systemic therapy Systemic therapies include treatment with cytotoxic or cytostatic drugs, targeting rapidly dividing cells, as well as some newer biological therapies that for example target proteins expressed only by cancer

cells or modify the immunological response, and hormone therapy that block the effect of hormones in some hormone sensitive cancers.

1.1.4 Radiotherapy

The primary biological effect of ionizing radiation is damage to cellular DNA. While free electrons can directly damage DNA molecules it is more likely to interact with a water molecule and produce a free radical which in turn can indirectly damage nearby DNA molecules. The cellular response to damaged DNA depends on cell type and radiation dose. A number of factors influence cell response (Specht 2012):

Repair mechanisms Irradiated cells are to a varying degree able to repair part of the inflicted damage as long as the total dose is delivered in smaller quantities (fractions) and given they have sufficient time to complete the repairs (approximately six hours). Tumour cells and normal tissues with acute radiation reaction, e.g. bone marrow and intestinal epithelium, exhibit limited repair. Some normal tissue types that display significant late effects to radiation exhibit substantial repair of DNA damage at low radiation levels. It is thus advantageous to deliver the total dose in smaller fractions of typically 1.8-2.0 Gy in order to achieve a profound effect on tumour tissue with limited late effects to normal tissue.

Cell proliferation In fractionated radiotherapy, surviving cells are able to proliferate in between fractions. Consequently, it is important to keep time between fractions to a minimum.

Oxygenation Hypoxic cells are relatively radiation resistant.

Cell cycle Cells sensitivity to radiation varies throughout the cell cycle. The sensitivity is greatest late in the Gap 1 phase and Synthesis phase, and least in the Gap 2 phase and early in the mitosis.

Cells that are damaged to such a degree that they cannot survive and divide may undergo different processes:

- Apoptosis or programmed cell death through damage to the mitochondria with activation of the caspase cascade.
- Necroptosis through hyperactivation of an enzyme involved in DNA repair.

- Mitotic catastrophe, caused by aberrant cell cycle progression or mitosis. Such cells may then go into senescense or die by apoptosis or necroptosis.
- Autophagy, characterized by sequestration of cell components in autophagic vesicles where they are degraded, providing material for new synthesis processes.
- Senescence, where cells enter a state of permanent cell cycle arrest, while remaining active in terms of metabolism.

Photon therapy employing linear particle accelerators (linacs) is currently the predominant radiotherapy modality. Figure 1.1 shows a linear accelerator. Linear accelerators increase the velocity of charged subatomic particles or ions along a linear beamline, by means of a series of oscillating electric potentials. In external beam radiotherapy devices, monoenergetic electron beams between 4 and 25 MeV are directed at a high-density, water-cooled tungsten target to produce high-energy photons with a spectrum up to and including the electron energy. The photon treatment beam passes through, and is shaped by, a multileaf collimator (MLC), focusing the radiation towards the target volume. Figure 1.2 shows how the photon beam is collimated by the MLC. The patient is positioned on the couch. The gantry rotates around the patient, enabling the treatment beam to target the tumour from all sides and thereby focusing the delivered radiation dose.

Figure 1.3 shows a flowchart for a typical course of radiotherapy. Prior to initiating treatment, a set of 3D planning images are obtained and volumes of interest are delineated. The treatment plan is optimized according to desired doses to delineated volumes. During a course of fractionated radiotherapy it may become necessary to update the treatment plan due to changes in patient anatomy. (Grégoire et al. 2011)

1.2 Imaging modalities for radiotherapy planning

For many tumour sites, radiotherapy is planned based on 3D positron emission tomography/computed tomography (PET/CT) scans. A PET/CT scan is a fusion of a CT scan that provides anatomical information, and a PET scan that provides biological/functional information. For some tumour types and locations it is beneficial to acquire 3D magnetic resonance imaging (MRI) scans as well, as MRI offers better soft tissue contrast than CT. MRI images can be fused to PET/CTs using image registration (see Section 2.3). Recently positron emission tomography/magnetic resonance imaging (PET/MRI) scanners have become available as well.

Figure 1.1: The Varian Clinac®iX linac radiotherapy device with integrated CBCT scanner. Image courtesy of Varian Medical Systems, Inc. All rights reserved.

1.2.1 Computed tomography (CT)

In computed tomography (CT) imaging, X-ray technology is employed to visualise tissue density. Tomography signifies volume imaging in the sense that 3D information about the scanned subject is acquired. In traditional X-ray transmission imaging, photons with wavelengths ranging between 0.01 and 10.0 nm and energies between 100 eV and 100 keV are generated and directed towards the subject under investigation. At kV energies, photoelectric absorption is dominant, depending on (and about proportional to) atomic number, while at MV energies, Compton scattering is dominant, depending mainly on electron density. Opposite the X-ray source, the unabsorbed photons are registered on photographic film or by scintillation detectors. In conventional X-ray images, volumetric information is lost when acquiring a transmission image of a 3D subject on a 2D image plane. A given point on the 2D image plane describes the integral attenuation along the beam line between that point and the X-ray point source. In CT imaging, projections are obtained from a multitude of imaging angles, making it possible to perform a mathematically based tomographic reconstruction of the 3D information otherwise lost (Cormack 1963; Hounsfield 1972; Hounsfield 1973). The CT scan offers 3D information about tissue density

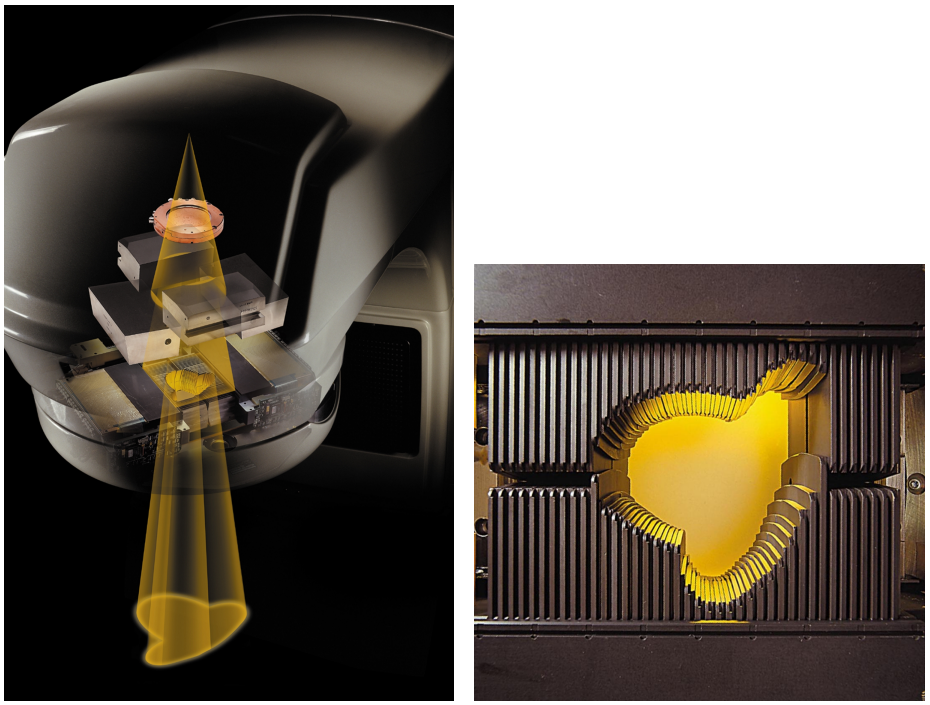

Figure 1.2: **Left:** An external beam radiotherapy device shaping the X-ray beam with a multileaf collimator (MLC). **Right:** Close-up of an MLC. Images courtesy of Varian Medical Systems, Inc. All rights reserved.

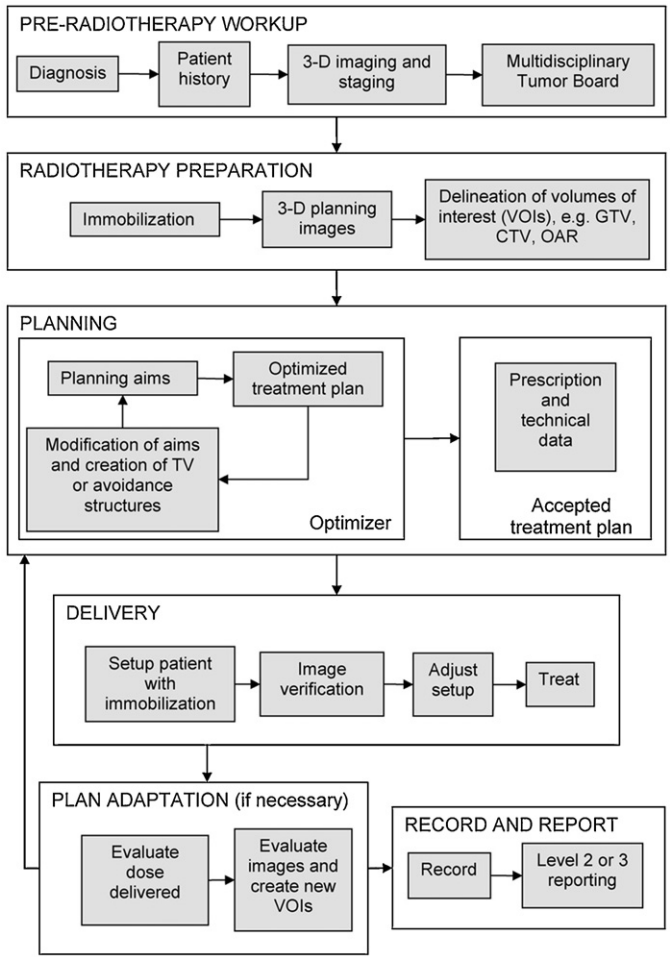

Figure 1.3: Flowchart of a typical course of radiotherapy. Reprinted from Grégoire et al. 2011 with permission.

Substance	HU
Air	-1000
Lung	-500
Fat	-100 to -50
Water	0
CSF	15
Kidney	30
Blood	30 to 45
Muscle	10 to 40
Grey matter	37 to 45
White matter	20 to 30
Liver	40 to 60
Bone	700 (trabecular bone) to 3000 (compact bone)

Table 1.1: Hounsfield units of selected tissues and substances.

on the Hounsfield scale, as defined by Brooks et al. 1980. The Hounsfield unit (HU) is related to the linear attenuation coefficient of the tissue by

$$\mathrm{HU} = 1000 \times \left(\frac{\mu}{\mu_{water}} - 1 \right) \tag{1.1}$$

Table 1.1 lists HU values of selected tissues. An important drawback with CT imaging is the ionizing dose delivered to the patient, ranging from 1-10 mSv Shrimpton et al. 2006. For a more comprehensive introduction to CT imaging see e.g. Beutel et al. 2000.

1.2.2 Positron emission tomography (PET) and PET-CT fusion

In PET imaging, a 3D image of biological activity within the body is produced through the detection of gamma rays that are emitted when injected radioisotope tracers decay and release positrons.

First, the patient is injected with a radioisotope tracer. As the radioisotope decays, positrons are emitted. As the positrons collide with electrons, two photons (gamma rays) are emitted in opposite directions. The photons are detected in a ring of discrete scintillation detectors surrounding the patient. As the two photons are emitted at a 180° angle, the line of response is between the two detectors on the ring recording the event. Localisation of the event along this line can be calculated from the very small time difference in detection. (Robertson et al. 1972; Phelps et al. 1975; Cherry et al. 1997; Schmand et al. 1998)

Total photon emission is attenuated by the tissue, much like in CT. Since high density tissue is more likely to absorb photons, and since emission from deep within the body is more attenuated than emission from the outer layers, attenuation correction is critical to avoid errors in the 3D reconstruction. The correction is based on a 3D map of tissue density. For this purpose, a CT scan is used.

Ido et al. 1978; Phelps et al. 1979 described the synthesis and first use of the 2-deoxy-2-(^{18}F)fluoro-D-glucose (FDG) tracer. It is the most utilized radioisotope tracer for radiotherapy treatment planning. Since tumours have a high glucose uptake, due to increased cell proliferation, this glucose analogue is concentrated in tumours. FDG tracers are used for functional analysis of brain, heart and lungs as well. Using PET, it becomes easier to see whether the primary tumour has metastasised.

A combined PET/CT scanner was first described by Beyer et al. 2000. Until then the scans were acquired using separate devices. Combined scanners are beneficial for optimal alignment of the scans for the fusion. Figure 1.4 shows a fusion of a CT and a PET scan.

1.2.3 Magnetic resonance imaging (MRI) and PET-MRI fusion

In magnetic resonance imaging (MRI) the magnetic properties of hydrogen atoms in water and fat molecules are exploited in order to produce detailed tomography images with high soft-tissue contrast. Unlike CT, it even provides contrast between soft tissues with same density, making it well suited for imaging of tumours.

The subject is positioned in a powerful magnetic field, aligning the spin axis of the magnetic hydrogen atom nuclei in the human body along the magnetic field. A little more than half of the nuclei are aligned parallel to the field, in a low energy state. A little less than half are aligned anti-parallel to the magnetic field, 180° rotated, in a high-energy state. There is a linear relationship between the magnetic field strength and the energy difference between the low and high energy states. The same goes for field strength and spin excess - the excess number of spins in the low energy state.

When applying a radio frequency (RF) field (an oscillating magnetic field), perpendicular to the main magnetic field, at the proton precession frequency (the resonance frequency), some excess spins in the low energy state transition into the high energy state, producing a flip of the net magnetization. When the

RF field is turned off, a signal is induced in a receiver coil as the excess spins transition back to the low energy state. Hydrogen atoms in different tissues have different magnetic properties, hence different resonance frequencies, making it possible to create fat- or water-weighted images, for example.

As the precession frequency is dependent on the main field strength, different parts of the body can be examined by different RFs when applying gradients to the main field. Hence, a 3D image can be constructed.
(Damadian 1971; Lauterbur 1973; Mansfield 1977; Damadian et al. 1976)

Judenhofer et al. 2008 described the first prototype combined PET/MRI scanner. These systems are already commercially available. As PET must be attenuation corrected it is still being investigated how this is best done using the MRI image that, unlike CT, does not inherently provide tissue attenuation information (Hofmann et al. 2009). In addition, PET/MRI has some advantages over PET/CT:

- PET/MRI systems are very promising in terms of alignment precision between the functional and anatomical image information. While PET/CT is acquired sequentially, PET/MRI can be acquired simultaneously.
- Unlike CT, MRI does not add additional radiation dose.
- In addition to structural information, MRI offers a variety of tissue contrasts, water diffusion imaging, magnetic resonance spectroscopy (MRS), and functional MRI (fMRI) where the haemodynamic response is quantified. Judenhofer et al. 2008; Kjær et al. 2013; Dirix et al. 2009; Smith et al. 2004

Figure 1.4 compares the PET/CT and PET/MRI for a patient with cervical cancer.

1.3 Radiotherapy planning

Patients present to the oncology department with a suspicion of cancer[1] and they are subsequently referred for site-specific diagnostic and staging studies, including imaging with CT or PET/CT for cases where functional imaging is expected to be beneficial. In some cases, where soft tissue contrast is important, such as for brain or cervix cancers, an additional MRI might be acquired.

[1] At Rigshospitalet, patients present with a diagnosis as they are referred from regional hospitals.

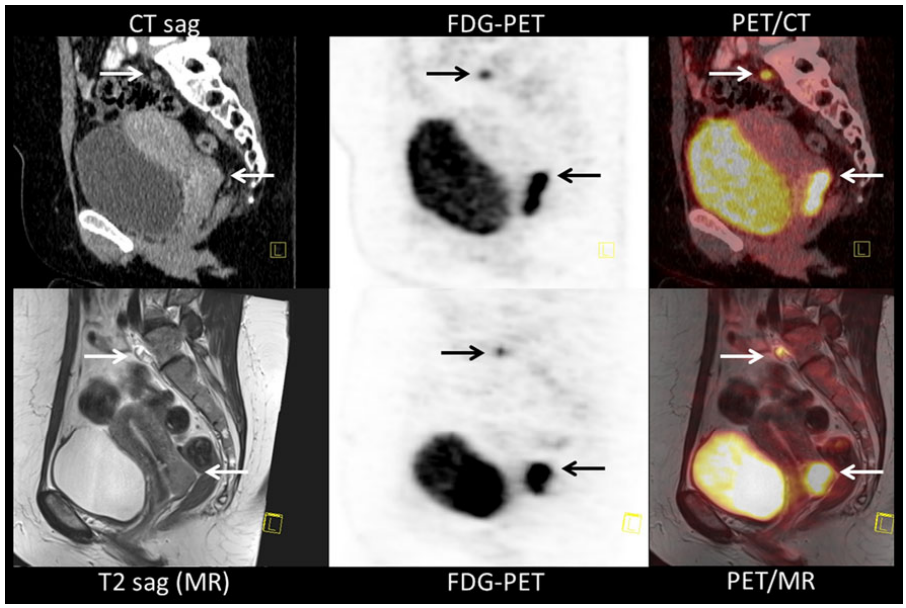

Figure 1.4: Imaging of a patient with cervical cancer. **Top:** PET/CT shows the hypermetabolic primary tumour in the cervix, posterior to the urinary bladder, as well as an involved lymph node, both indicated with arrows. **Bottom:** PET/MRI reveals the same findings but with a more precise definition of the primary tumour. Reprinted from Kjær et al. 2013 with permission.

Recently, a PET/MRI scanner has been installed at Rigshospitalet, but it is not yet used for routine clinical imaging. During these scans the patient is immobilised, often also with a custom moulded head fixation mask. It is important that the patient maintains the same posture for both imaging and treatment in order to achieve the planned dose delivery distribution.

After a patient has undergone a complete staging work-up, a multi-disciplinary discussion takes place in order to determine the best treatment options for the patient. For localised and clearly outlined tumours with no metastases it might be possible to remove the tumour by surgical resection. For patients with local and regional disease radiotherapy is often an option, with or without additional systemic treatment. For patients with disseminated disease some form of systemic treatment is needed, but for most solid tumours this treatment is not curative if given alone.

1.3.1 Delineation of volumes of interest (VOI)

The target volume outline is manually delineated in each transaxial slice of the 3D structural CT scan with aid from the functional information from the PET scan.

Three target volumes are delineated on the planning CT scan; the gross tumour volume (GTV), the clinical target volume (CTV) and the planning target volume (PTV). All organs at risk (OAR) and their associated planning organs at risk volume (PRV) are also defined (Grégoire et al. 2011; Halperin et al. 2008):

GTV This volume is comprised by the primary tumour and clinically detectable, involved regional lymph nodes and the distant metastases, if any. Information from the PET scan is very important for locating all metastases.

CTV This volume contains the GTV as well as suspected subclinical malignant disease. Since tumours are known to demonstrate microscopic infiltrations, tissue boundaries that are seemingly clear on the scans are affected by some uncertainty (Daisne et al. 2004). Statistical data and clinical knowledge about lymph node drainage patterns for different tumour sites may be utilised as well (Boehmer et al. 2006; Roels et al. 2006; Grégoire et al. 2000).

PTV This volume contains the GTV and CTV and adds a margin to account for geometric uncertainties such as (Herk 2004; Nijkamp et al. 2012)

- The limited resolution of the imaging modalities, so-called partial volume effects (Links et al. 1998).
- Setup accuracy.
- Physiological factors such as organ motion, i.e. bladder filling, rectal filling, peristalsis, breathing-related lung motion etc.

PRV This volume contains the OAR as well as all geometric uncertainties related to its position and contour.

1.3.2 Plan optimisation

As previously stated, the goal of radiotherapy is to deliver a prescribed dose to the tumour in order to maximise the tumour control probability (TCP). In this context, it should be noted that dose is usually prescribed to PTV, which contains both the CTV and GTV. In intensity-modulated radiotherapy (IMRT), the dose is delivered from a multitude of angles by means of a rotating gantry of the linac. Furthermore, MLC position is modified in order to modulate the intensity of radiation within each beam. Under supervision, the treatment planning software optimises treatment angles and MLC position according to the planning objectives. Figure 1.5 shows treatment plans with visualised treatment beams for prostate and lung cancer cases.

The quality of a plan is usually evaluated in terms of cumulative dose-volume histograms (DVHs). These histograms indicate the percentage of the volumes that receive the prescribed dose (Lyman 1985; Lyman et al. 1987; Lyman et al. 1989). Figure 1.6 shows a typical DVH for a lung cancer patient. The DVH curves indicate that most of the PTV and GTV receives the prescribed dose, while the OAR are spared from receiving high doses.

Given the DVH based objectives, the plan is optimised using specialised software that employs advanced mathematics for optimisation. Algorithms such as the Monte Carlo method are employed for calculating the resulting dose distribution, see e.g. Reynaert et al. 2007; Chetty et al. 2007; Shepard et al. 2002. The treatment plan parameters that are optimised may include the selected beam angles[2], collimator angles, beam energy, MLC position, relative weighting of each beam, and presence of wedges. The limitation of a DVH is that it does not indicate a location of a certain dose. It is necessary for the treating radiation oncologist to view isodose volumes on axial CT slices to know precisely where the hot and cold spots occur, and to evaluate for adequate coverage of their target volumes.

[2]Often not included as it offers to many degrees of freedom.

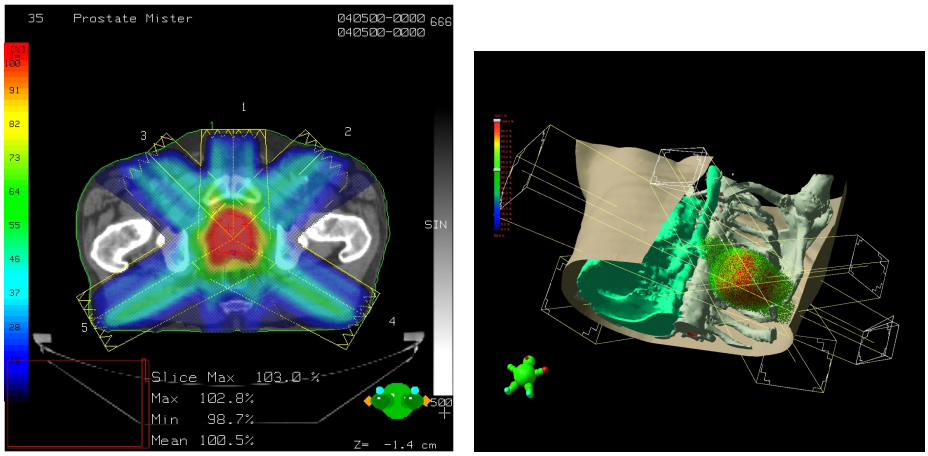

Figure 1.5: **Left:** An IMRT treatment plan for a patient with prostate cancer, generated using Eclipse^{TM} treatment planning software. The area of high dose (red) corresponds precisely to the tumour area being treated. **Right:** A lung cancer treatment plan generated using Eclipse^{TM} treatment planning software. Images courtesy of Varian Medical Systems, Inc. All rights reserved.

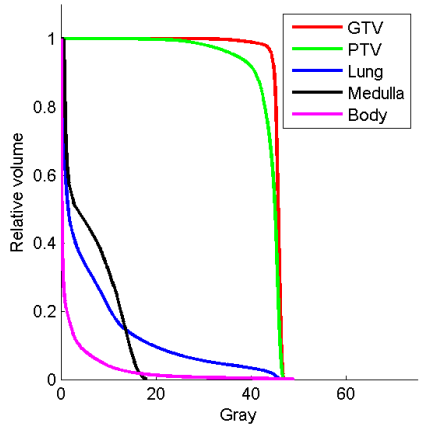

Figure 1.6: Example of a dose-volume histogram (DVH) for a patient with lung cancer. Reprinted from Hollensen 2012 with permission.

1.4 Imaging modalities available in treatment room

In addition to the linac, in-room image-guidance may be accomplished by multiple modalities including integrated cone beam CT (CBCT), CT on rails, integrated CT or integrated MRI in form of MRI-linac systems.

1.4.1 CBCT

An integrated kV CBCT-linac system was first described by Jaffray et al. 2002, see Figure 1.7 Compared to a normal CT scanner, the beam is cone-shaped instead of fan-shaped. The detector is a flatpanel and not a curved line array, meaning that a full volume is imaged with one rotation. As one rotation takes at least 60 seconds due to safety regulations, breath-hold scans are not feasible. The resulting conventionally reconstructed tomographies of thorax will have motion blurring due to breathing and cardiac motion. To some extent, Section 3.2 deals with motion blurring effects.

CBCT provides a 3D assessment of patient anatomy and positioning. If acquired daily, CBCT allows evaluation of interfraction changes in patient anatomy such as bladder filling and rectal distension, which may cause significant changes in dosimetric coverage. In addition CBCT allows volumetric comparison to the planning CT to aid in determining when a replanning CT becomes necessary.

At around 10-30 mGy, the dose is the same or higher than a conventional CT (Islam et al. 2006; Walter et al. 2007).

Both MV and kV CBCT systems are available. MV CBCT systems use the linac treatment beam as X-ray source and an electronic portal imaging device (EPID) flat panel detector, see e.g. Swindell et al. 1983; Midgley et al. 1998. While an advantage of MV imaging is that it provides the beam's eye view (BEV), Groh et al. 2002 concludes that kV CBCT offers significant performance advantages over MV CBCT in terms of image contrast and signal-to-noise ratio (SNR) per unit dose for visualization of soft-tissue structures. kV CBCT adds less dose than MV CBCT (Walter et al. 2007).

Compared to conventional CT, CBCT often suffers from a number of quality issues and artifacts such as motion blurring caused by the previously mentioned long rotation time, a higher level of scatter noise related to the cone-beam geometry, beam hardening effects caused by the use of wide spectrum (unfiltered) X-ray sources, and ring artefacts due to detector or geometry imperfections (Schulze et al. 2011). Many of these artefacts can be corrected for, see e.g.

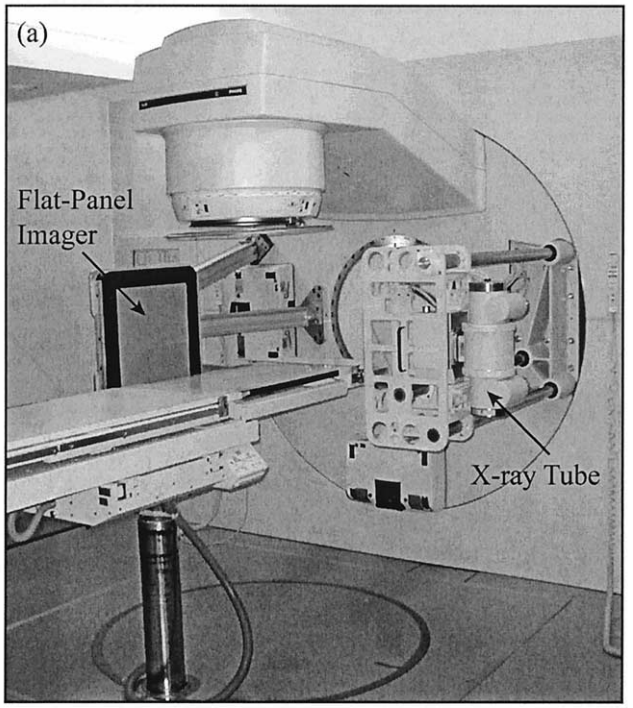

Figure 1.7: A medical linear particle accelerator (linac) modified for kV cone beam CT (CBCT). A kV X-ray tube has been mounted on a retractable arm at 90° with respect to the treatment source. A large-area, 41×41 cm flat-panel detector is mounted opposite the kV X-ray tube on a fixed mount. Reprinted from Jaffray et al. 2002 with permission.

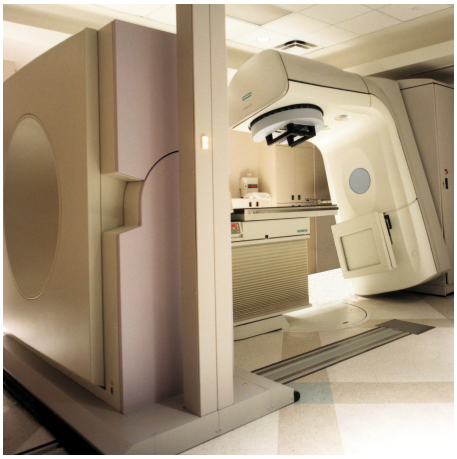


Figure 1.8: **Left:** The Siemens Primatom system. Image courtesy of Siemens AG. All rights reserved.
Right: The Accuray TomoTherapy TomoHD system. Image courtesy of Accuray, Inc. All rights reserved.

(Zhang et al. 2010; Hsieh et al. 2000; Sonke et al. 2005; Siewerdsen et al. 2006; Wang et al. 2009; Jia et al. 2010). As some of the correction methods are based on iterative algorithms and are thus time consuming, they are often not available in clinical settings.

1.4.2 CT on rails and integrated CT systems

Figure 1.8 shows a Siemens Primatom system consisting of a Primus linac and a Somatom sliding gantry CT (CT-on-rails) scanner. The couch can be rotated, allowing for transport of the immobilised patient from the CT gantry to the linac. The figure also shows an Accuray TomoTherapy system integrating both CT and linac in the gantry.

Both types of systems are capable of acquiring standard CT scans before the delivery of each fraction. The reconstructed images can be used for both patient setup and interfraction treatment plan adaptations. Since it is the same image modality as is normally used for planning scans, the images are easily compared and evaluated either manually or automatically. (Uematsu et al. 1996; Uematsu et al. 1998)

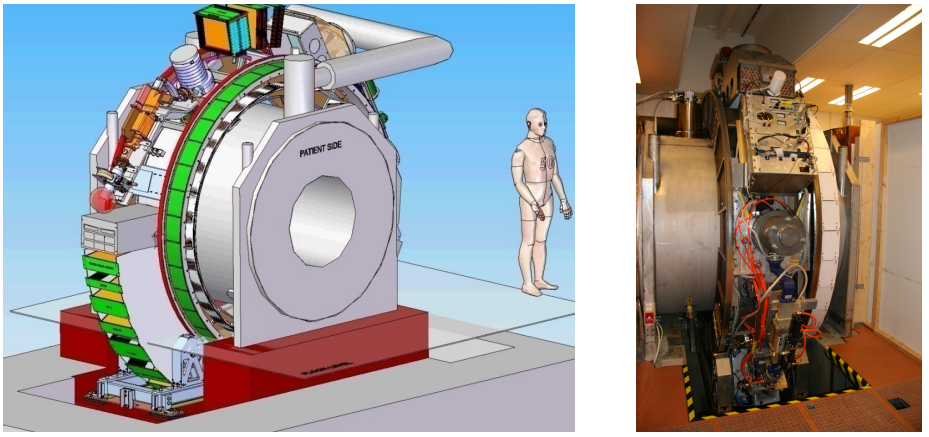

Figure 1.9: The UMC Utrecht prototype MRI-linac. Reprinted from Crijns 2013 with permission.

1.4.3 Integrated MRI-radiotherapy systems

Recently, integrated MRI-radiotherapy systems have been investigated and are currently under development, see e.g. Lagendijk et al. 2008; Raaymakers et al. 2009; Fallone et al. 2009; Dempsey et al. 2011; Dempsey et al. 2005. One such system is already available for purchase from ViewRay, Inc. Figure 1.9 shows the UMC Utrecht prototype system. Figure 1.10 shows the ViewRay system.

These systems integrate an MRI scanner with a linac therapy device (ViewRay uses three Cobalt sources instead of a linac). Like an ordinary MRI scanner, it is possible to obtain volumetric images. Like the CBCT and CT systems, these can be used for daily treatment plan adaptation according to changes in patient anatomy, see Section 2. Furthermore the systems are capable of intrafraction imaging on a sub-second time scale. This is useful for treatment beam gating or guidance, see Section 3.

Compared to X-ray based imaging, daily MRI imaging contributes with no extra dose to the patient.

Figure 1.10: The ViewRay MRI/cobalt therapy device. Image Courtesy of ViewRay, Inc. All rights reserved.

1.5 Patient setup

Ahead of each fraction delivery, the patient is usually immobilised and rigidly positioned by means of isocentric laser guidance based on skin markings placed pre-treatment. Even though the patient is set up according to external skin markings, the internal anatomy might deviate from when the planning CT scan was acquired, and the target may be displaced. Immobilisation does reduce setup errors, but still, mean setup displacement errors on the scale of 4-10 mm have been reported (Hurkmans et al. 2001; Clippe et al. 2003; Bray et al. 2012).

A patient's position can be verified using the in-room treatment modalities, by rigid image registration of daily images to the planning CT scan (Bel et al. 1993; Boer et al. 2001; Clippe et al. 2003). Using such methods, translation and rotation can be determined. While conventional CT does produce images of better quality than CBCT, transferring the patient from the the CT scanner to the linac can introduce motion associated setup error. For linacs with integrated imaging, verification can often be performed during delivery as well, and the treatment can be stopped or paused if the patient moves. Verification can be based on both bony and soft tissue landmarks. Due to lack of contrast, soft tissue verification is usually only possible for lung tumours.

Chapter 2

Interfraction treatment plan adaptations

One of the greatest challenges in modern radiotherapy is modifying a plan to match tumour response during treatment. Figure 2.1 shows an example of pronounced anatomic changes during treatment of a head & neck cancer (HNCA) patient. The delineated volumes of interest clearly do not align to the anatomy three weeks into the treatment. With current imaging, delivery and treatment planning technology it is possible to shape and deliver dose with a level of accuracy and precision that is unsuitable due to the magnitude of daily setup errors and changes in anatomy. In the near future, proton therapy will be implemented on a large scale, highlighting the importance of higher delivery accuracy.

In adaptive radiotherapy (ART), the treatment plan is corrected according to anatomical changes in tumour and normal tissue anatomy. The concept of ART is not new. Technical limitations as well as additional work load of staff are holding back full-scale clinical implementation. For ART to make its way into routine clinical use, fast, reliable, automatic methods need to be developed.

This chapter describes approaches and technologies to support ART.

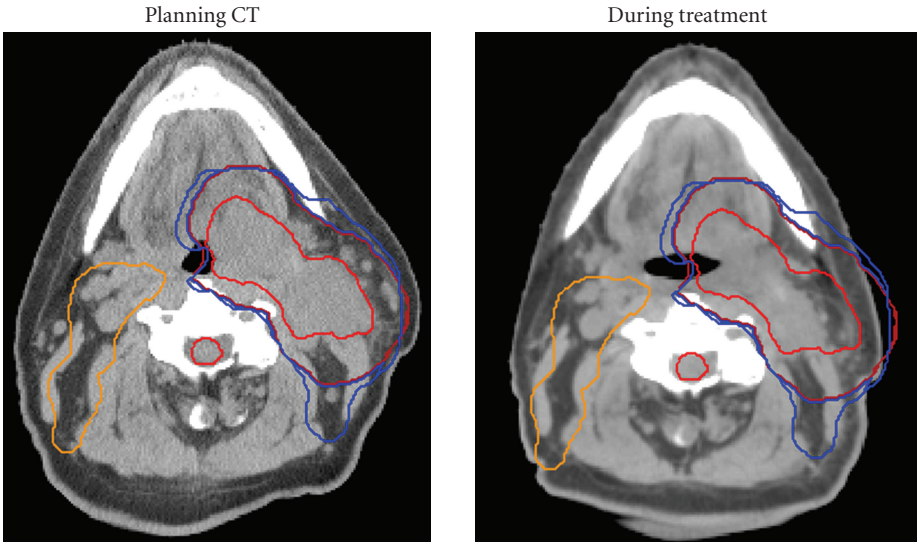

Figure 2.1: Anatomic changes can be pronounced during treatment. In this example, planning CT scan and CTV contours are shown on the left. On the right, a mid-course CT (three weeks into treatment) demonstrates significant reduction in gross tumour (thick red line). Baseline CTVs have been overlaid via rigid image registration. These match current anatomy poorly and in fact extend past the skin contour into air. Reprinted from Schwartz et al. 2011 with permission.

2.1 Library planning

Depending on tumour site, daily changes in anatomy may primarily be due to different levels of organ filling and organ motion. The bladder changes shape and volume dependent on filling. Furthermore, variations in rectal volume cause displacement of the bladder. In order to achieve a consistent bladder volume, the patient will usually be asked to void before each fraction delivery. Despite attempts to control bladder volume, significant interfraction changes have been documented (Turner et al. 1997; Fokdal et al. 2004). For bladder cancer, a 'plan of the day' or 'library of plans' approach has been investigated by e.g. Burridge et al. 2006; Chai et al. 2010; Murthy et al. 2011; Meijer et al. 2012. A 'library of plans' is created ahead of treatment and the most appropriate plan from the library is chosen prior to the delivery of each fraction, based on daily imaging.

Burridge et al. 2006 created three plans with diverse margins in the superior direction. They chose the best plan based on daily CBCT scans. The average small bowel volume that could be spared by choosing between the three plans was 31 ± 23 cm^3.

Murthy et al. 2011 created 6 plans based on an empty bladder planning CT scan. The plans used 6 different isotropic PTV margins. Figure 2.2 shows one example of a planning CT with isotropic margins.

Meijer et al. 2012 acquired two planning CT scans, one with empty bladder and one with full bladder. The GTV was delineated in both scans and from these, 3 additional GTV volumes were created by interpolation and one by extrapolation. Prior to delivery of a fraction, the most appropriate plan was selected according to the bladder shape, based on CBCT imaging. The authors conclude that a highly conformal dose distribution was delivered to all bladder cancer patients with promising clinical results. Figure 2.3 shows a daily CBCT scan with the library of 6 GTV contours overlayed.

Chai et al. 2010 modelled patient-specific bladder deformation patterns from the first five daily CBCT scans performed during fractionated radiotherapy (RT) employing principal component analysis (PCA). They conclude that their statistical shape based segmentation approach robustly handles the relatively poor CBCT image quality and allows for fast and reliable automatic segmentation of the bladder for selection of the appropriate plan from the library of plans.

The benefit of the library planning approach is that all plans can be prepared in advance. When comparing Figure 2.2 and 2.3 described above it is clear that a library of plans should be tailored for each individual patient whenever possible as a library of isotropic margins does not describe the range of anatomical vari-

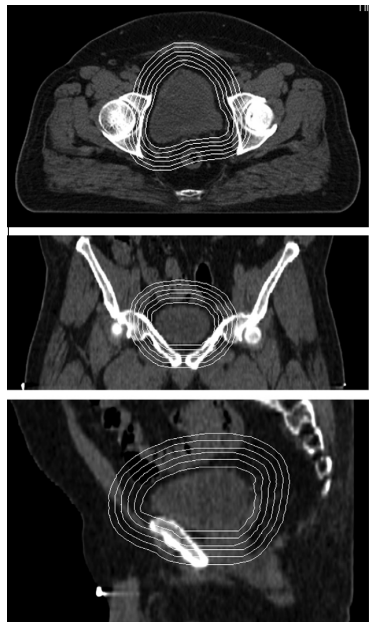

Figure 2.2: Planning CT scan in axial, coronal and sagittal planes with six isotropic PTV margins. Reprinted from Murthy et al. 2011 with permission.

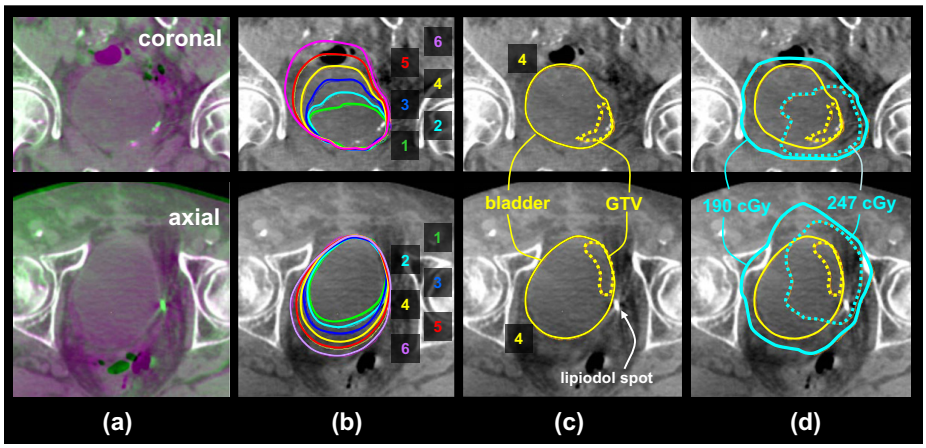

Figure 2.3: Coronal and axial images of the treatment procedure: (a) automatic bone registration (purple planning CT, green CBCT), (b) plan selection based on bladder volume at CBCT, (c) manual registration of the GTV using lipiodol markers, (d) target coverage verification. Reprinted from Meijer et al. 2012 with permission.

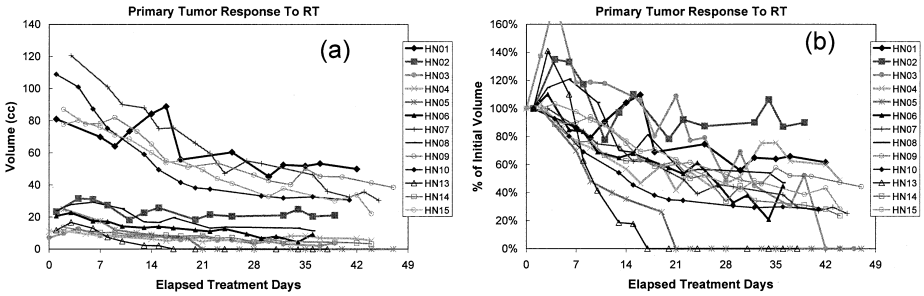

Figure 2.4: Primary tumour response to radiotherapy for HNCA patients expressed as GTV volume changes over time. All volume changes follow a similar trend. GTVs decreased at a median rate of 0.2 cm^3 or 1.8% of initial volume per day of treatment. Reprinted from Barker et al. 2004 with permission.

ations particularly well. However, any library of plans might not accommodate all anatomical variations encountered during treatment.

2.2 Radiation induced tumour volume changes

In addition to daily anatomical variations of OAR, tumours exhibit volume changes to a varying degree during the course of radiotherapy. This is particularly true in head and neck, lymphoma and gynaecological cancers (Barker et al. 2004; Girinsky et al. 2006; Yahalom 2005; Lim et al. 2008; Mayr et al. 2010). For a study including HNCA patients, Barker et al. 2004 showed that gross tumour volumes decreased at a median range of 0.2 cm^3 per treatment day, with volume changes ranging between 0.01-2.0 cm^3/day, corresponding to a relative change of 1.8% of the initial volume per day. The median total tumour volume change was 70%, ranging between $9.9 - 92\%$. The median centre of volume displacement was 3.3 mm, ranging between 0-17 mm. Figure 2.4 shows the volume response curves for GTVs and lymph nodes $> 2cm^3$ in volume.

Looney et al. 1975; Kovacs et al. 1976 demonstrated that following irradiation, the growth rate of tumours is approximately linear (and negative) on a logarithmic scale, after an initial delay in response.

The consequence of maintaining a large initial PTV throughout treatment, when tumour volume changes are significant, is that normal tissue and potentially OAR might be irradiated with high dose.

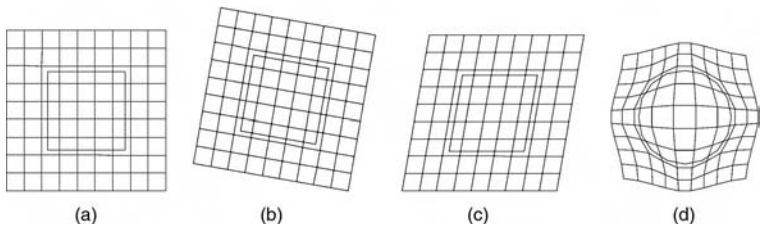

Figure 2.5: **(a)** Identity transformation. **(b)** Rigid transformation. **(c)** Affine transformation. **(d)** Deformable transformation. Reprinted from Hajnal et al. 2010 with permission.

2.3 Deformable intrasubject image registration

The concept of deformable image registration (DIR) is important to the field of adaptive radiotherapy (ART). Most protocols for adaptation of the treatment plan rely on it. DIR can be used to determine a non-rigid spatial transformation that establishes meaningful correspondence between images of a patient acquired at different points in time and/or acquired with different imaging modalities.

In DIR, a target image T is deformed by a transformation ϕ in order to satisfy an objective function that maximises similarity with a reference image R. This is often achieved by finding the transformation that minimises a *dis*similarity measure $\mathcal{D}$ between R and the transformed target image $T \circ \phi$ as

$$\min_{\phi} \left(\mathcal{D}(R, T \circ \phi) + \mathcal{R}(\phi) \right), \tag{2.1}$$

where $\mathcal{R}$ is a regularisation term, penalising transformations that are for one reason or the other unlikely.

The transformation is a deformation field of vectors that for each pixel/voxel in the reference image map to the corresponding point in the target image. As most images used in radiotherapy are three dimensional, the deformation field is three dimensional as well. A CT or MRI scan can easily hold $512 \times 512 \times 200 = 52.4 \cdot 10^6$ voxels. As each deformation vector itself is three dimensional, the total number of estimated parameters would in this case be $157 \cdot 10^6$.
(Hajnal et al. 2010)

2.3.1 Parametric transformation models

Direct optimisation of the image registration problem is ill-posed due to the number of estimated parameters. Instead of direct optimisation of the dense deformation field, the transformation is often modelled by more compact deformation models with fewer parameters that employ interpolation to determine the dense deformation field. Such models include, but are not limited to, the free-form deformation (FFD) (b-spline) model (Rueckert et al. 1999), thin-plate splines (Rohr et al. 2001), radial basis functions (Fornefett et al. 2001), finite-element model (Xuan et al. 2006), and piece-wise linear transformations (Arsigny et al. 2003).

2.3.2 Non-parametric transformation models

In addition to the parametric models, image registration can be non-parametrically modelled. Horn et al. 1981 modelled registration using equations from physics for motion of incompressible fluids. Thirion 1998 modelled registration as a diffusion process. This method is often called demons registration.

2.3.3 Objective functions

Feature-based objective functions aim to minimise the distance between landmarks. An Euclidean distance measure is often employed. As both manual and automatic landmark extraction in three-dimensional medical images is generally non-trivial, feature-based objective functions are seldomly used for time critical applications. (Joshi et al. 2000; Lowe 2004)

Intensity-based objective functions evaluate the intensity difference between the reference image and the deformed target image. When registering images that are acquired with the same imaging modality and are characterised by similar intensity distributions, a normalised sum of absolute differences (SAD), sum of squared differences (SSD) or normalised cross-correlation (NCC) objective function can be sufficient (Hajnal et al. 2010). More computationally demanding objective functions such as correlation ratio (Roche et al. 1998) and mutual information (Wells et al. 1996; Maes et al. 1997) are suitable for registration of images acquired with different modalities.

2.3.4 Regularisation

While the objective functions drives the registration process, it is often necessary to add a regularisation term in order to constrain the resulting deformation map and avoid undesirable characteristics. When modelling an intrasubject anatomical change with deformable registration, a diffeomorphic deformation field is preferred, that is, a smooth, non-folding, invertible field. This is often achieved by constraining the first derivative of the dense deformation field. Local rigidity can be achieved by imposing local orthogonality of the Jacobian matrix (Loeckx et al. 2004). Volume preservation can be achieved by constraining the determinant of the Jacobian matrix to unity (Rohlfing et al. 2003).

Biological studies have shown that biological tissue behaves similar to rubber. That is, they are nearly incompressible and compliant to shear, see e.g. Hu 2006; Sarma et al. 2003. Regularisation that imposes a rubber-like deformation prior is suitable for intrasubject image registration when images are acquired temporally close. In radiation oncology, patients are likely to exhibit significant general weight loss as well as tumour shrinkage, local oedema and tissue loss in proximity to the tumours during radiotherapy. These volume changes make use of a strict incompressibility constraint unsuitable. Relaxing the incompressibility constraint transforms the rubber prior into a more general elasticity prior. Linear elasticity matching (Broit 1981) has been widely used for image registration but the lack of local rotation invariance can hinder optimal matching. Especially in HNCA imaging, the neck posture (bending in the neck) may cause the linear elasticity prior to over-regularize the deformation. The Riemannian elasticity prior is a *simple* weighted quadratic penalty on the Hencky strain tensor which inherits local rotational invariance while the infinity energy limit approaches the black-hole deformation, signifying that collapsing tissue to an infinitesimally small volume takes infinite energy (Pennec et al. 2005). Figure 2.6 illustrates the concept of rotational invariance. The local deformation can be decomposed into an orthonormal tensor representing the rotation and a positive definite symmetric tensor representing the stretch. While biological tissue is elastically anisotropic, anisotropic modeling requires many parameters which cannot be estimated from CT scans alone. Assuming isotropic behaviour, the number of parameters can be reduced to two; the usual Lamé parameters μ, λ. The isotropic Riemannian elasticity is given as

$$\mathcal{R}_{rie}(\mu, \lambda; \phi) = \frac{\mu}{4} \sum_{i=1}^{N} \log^2 \varepsilon_i + \frac{\lambda}{8} \left(\sum_{i=1}^{N} \log \varepsilon_i \right)^2 , \tag{2.2}$$

where μ controls the amount of elastic potential due to shearing, and λ controls the amount of elastic potential due to local compression or expansion. ε_i are the

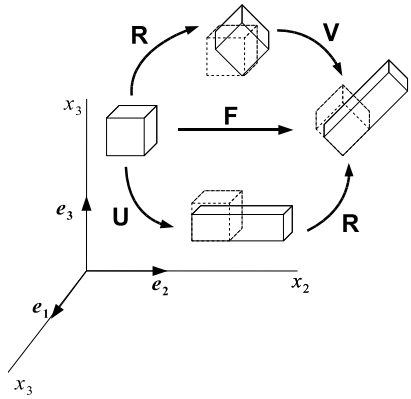

Figure 2.6: Rotational invariance illustrated. The local deformation can be decomposed into an orthonormal tensor representing the rotation and a positive definite symmetric tensor representing the stretch. Reprinted from Hansen 2009 with permission.

principal stretches. In contrast to linear elasticity and Saint-Vernant Kirchoff elasticity λ is solely related to local volume change (Hansen 2009).

2.4 Treatment plan adaptations

Some tumours exhibit variations that are primarily due to permanent changes in anatomy that cannot be predicted or planned for in advance. These include tumour annihilation, general weight loss, oedema, etc.

Figure 2.7 shows a typical workflow for treatment plan adaptation. Either a daily CT, CBCT or MRI scan is compared to the original planning scan. If needed, the daily scan forms the basis for propagation of contours of the target and OAR structures and subsequent treatment replanning to reflect the anatomical changes. In the literature this regime is generally referred to as image-guided radiation therapy (IGRT), although image guidance is used for treatment planning, patient setup as well as intrafraction guidance. The contour propagation from the 3D planning scan to a replanning scan can be automated by establishing correspondence between the images by means of image registration.

In short, replanning relies heavily on fast and accurate in-room imaging, fast and reliable deformable image registration of the daily scan to the planning scan, and fast treatment planning software.

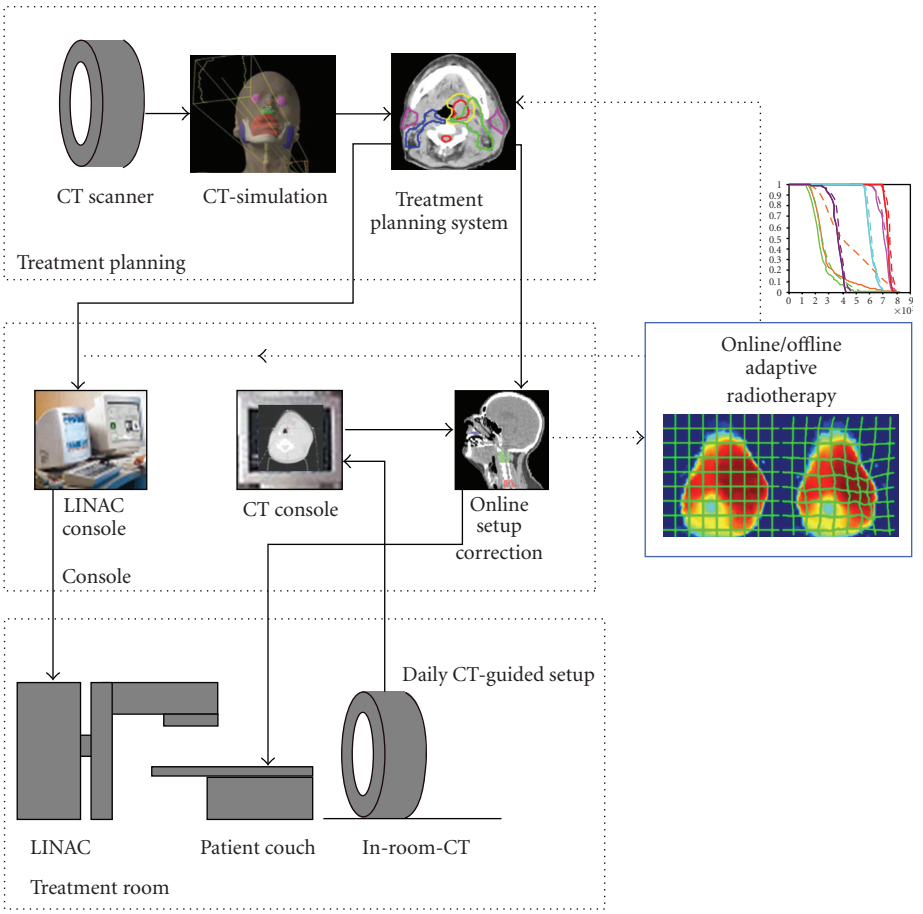

Figure 2.7: A workflow diagram for in-room CT or CBCT-guided adaptive radiotherapy. The first level of treatment modification is a simple couch shift to correct for daily setup errors (CT-guided IGRT). Nonrigid changes in tumour volumes and normal organs can then be corrected via an online or offline adaptive replanning process (dotted lines). Reprinted from Schwartz et al. 2011 with permission.

Figure 2.8 provides an example of deformable image registration with a Riemannian elasticity prior of a planning and replanning CT scan for a HNCA case with the purpose of automatic contour propagation. Contours propagated by deformable and rigid registration are compared to manual re-contouring. It can be seen how the rigid structures do not line up after rigid registration. Contours propagated using deformable registration resemble the manually propagated contours.

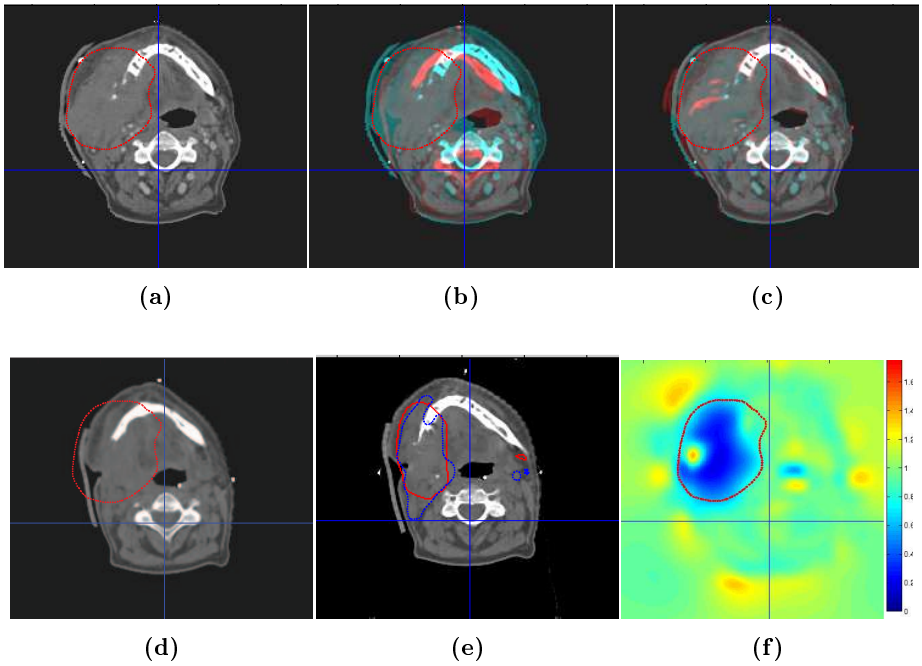

Figure 2.8: Example of contour propagation using deformable image registration with a Riemannian elasticity prior for a HNCA patient (Bjerre et al. 2012). **(a)** Planning CT scan with GTV contour (···). **(b)** Overlay of planning CT and rigidly registered replanning CT. **(c)** Overlay of planning CT and deformably registered replanning CT. **(d)** Replanning CT, rigidly registered to planning CT, with original contour. **(e)** Replanning CT with automatically adapted GTV contour (-) and manual replanning contour (···). **(f)** Jacobian determinant of the deformation field. Blue colour signifies volume shrinkage, red volume expansion, green no volume change.

Mohan et al. 2005 suggested a method for treatment plan adaptations that modifies the beam shape and intensity according to the new position and shape of the target and OARs without the use of traditional, time consuming replanning. A

daily CT scan was acquired and the contours were propagated from the planning CT. As this was a proof-of-concept study this was done manually, but would ultimately have to be done using deformable image registration of the volume images. The beam shape is modified according to the changes in target/OAR position and shape on projections from the BEV. For deformable registration of these 2D projection images they used the demons algorithm (Thirion 1998). The authors state that for the investigated prostate and HNCA examples this method yielded a good approximation of thorough replanning compared to other alternatives.

Feng et al. 2006 suggested a technique that directly modifies the MLC aperture shape of each segment based on the 2D vectors orthogonal to the beam direction generated by collapsing 3D deformation vectors along the beam line. The 3D deformation field was determined using a FFD registration method.

Ahunbay et al. 2008 suggested a technique that directly modifies the MLC segment shape based on daily images to avoid full replanning. Daily CT images were acquired using in-room CT-on-rails. A robust and semi-automatic tool was employed for rapid modification of PTV and OARs delineations to fit new location and shape of volumes. The beam shape was adjusted using a segment aperture morphing (SAM) algorithm where MLC leaf shifts are calculated based on the BEV of the original and new target projections. The segment weight for the new apertures are optimised using a segment weight optimisation (SWO) algorithm in order to optimise the dose distribution according to the plan objectives. The procedure took less than 10 minutes on a daily basis. The authors conclude that the dose distribution as given by DVHs is comparable to that achieved by thorough re-planning. Compared with the technique suggested by Mohan et al. 2005, this technique directly adjusts beam/segment shapes. Using the same method but with MIMVISTA deformable image registration software for contour propagation, Ahunbay et al. 2009 carried out a study including HNCA patients.

As most of this research is still in a proof-of-principle stage, there are few studies providing statistics on the effect of introducing ART techniques in the clinic. For 113 breast tumour patients, Hurkmans et al. 2012 performed a replanning scan 10 days into the treatment. By means of replanning, the volume receiving more than 95% of the boost dose could be reduced by 19%. The authors observed no changes in mean dose to the heart. They concluded that the procedure proved to be efficient and effective, leading to a clinically significant reduction of the high dose volume.
Schwartz et al. 2011 performed daily automated replanning of 22 HNCA patients. Their preliminary clinical outcomes document functional recovery and preservation of disease control at 1-year follow-up.

While recent research has been focused on reducing the time spent on contour propagation and treatment replanning by means of approximative methods, the advances in computational power as well as code optimisation and parallelisation might eventually close the gap to thorough replanning. It is notable that there is an apparent lack of studies comparing the accuracy of emerging commercial solutions (that are often 'black box' methods) and techniques described in the literature.

Chapter 3

Intrafraction motion management

In addition to daily changes, some sites of cancer are susceptible to significant intrafraction changes in anatomy. In addition to patient motion on the treatment table due to pain and/or anxiety, the abdominal and thoracic organs exhibit periodic anatomical changes caused by respiratory and cardiac motion (Bortfeld et al. 2004). In a review of 20 liver cancer patients, Kitamura et al. 2003 documented $[4 \pm 4, 9 \pm 5, 5 \pm 3]$ mm tumour motion amplitude in the left-right, craniocaudal and anterior-posterior direction respectively. For 54 renal cancer patients, van Sörnsen de Koste et al. 2006 reported predominantly craniocaudial motion. Mean motion was 9.8 mm for left kidney and 9.0 mm for the right, with maximum excursions of 30 and 20 mm respectively.

Respiratory tumour motion can be accounted for by means of patient-specific target margins based on 4D planning CT scans. 4D CT scans are comprised of 3D CT images at discrete phases of the respiratory cycle. It can be achieved by binning projections based on an external respiratory signal (Vedam et al. 2003a). Through detection of mid-ventilation tumour position and oscillation pattern the PTV margins can be reduced (Wolthaus et al. 2008; Hughes et al. 2008; Korreman et al. 2012; Aznar et al. 2013).

Alternatively, motion can be directly accounted for through the use of gating-

based or motion compensating methods, the purpose being to further reduce target margins.

This chapter describes approaches and technologies to support intrafraction motion management.

3.1 Marker-based motion management

Ideally, in order to compensate for intrafraction tumour and OAR motion and deformation, soft tissue tracking based on real-time volume imaging should be applied. This is, however, not feasible using X-ray based imaging. Thus, motion tracking based on implantable and external markers is the current state of the art when it comes to intrafraction motion compensation. Employing implantable gold fiducial makers, 3D internal marker and thus tumour position and motion can be determined from two orthogonal X-ray images. As constant X-ray imaging adds significant dose to the patient these systems are normally not used for constant tracking during treatment delivery. Markers on the outside of the body can be used to monitor breathing motion as well. A correlation between motion of the external marker and motion of the tumour can be established by monitoring marker motion while acquiring 4D scans, in which the tumour can subsequently be identified or by tracking an internal implantable fiducial marker using conventional X-ray. As such these external markers function as surrogates for tumour motion tracking. Figure 3.1 illustrates the configuration of X-ray sources and detectors used for motion tracking. (Seppenwoolde et al. 2007; Jin et al. 2008)

Marker-based motion tracking is readily available from commercial systems such as the Accuray CyberKnife Synchrony Respiratory Tracking System (RTS) or the BrainLab ExacTrac. The tracking accuracy of the CyberKnife system based on external markers and x-ray verification every 60 seconds is around 2 mm (Seppenwoolde et al. 2007). The ExacTrac system offers similar or slightly better accuracy (Jin et al. 2008).

While the ExacTrac system offers beam gating based on the respiratory signal, the CyberKnife system, based on a robotic arm linac enables motion compensated delivery (Adler Jr et al. 1997; Adler Jr et al. 1999; Schweikard et al. 2000; Chang et al. 2003). In beam gated delivery, the beam is switched off when the tumour moves out of the beam field. Using gated delivery it is possible to reduce margins (Hugo et al. 2003; Korreman et al. 2008) and escalate dose (Wagman et al. 2003), although Korreman et al. 2008 concluded that margins can only be reduced if respiratory baseline shifts and variations

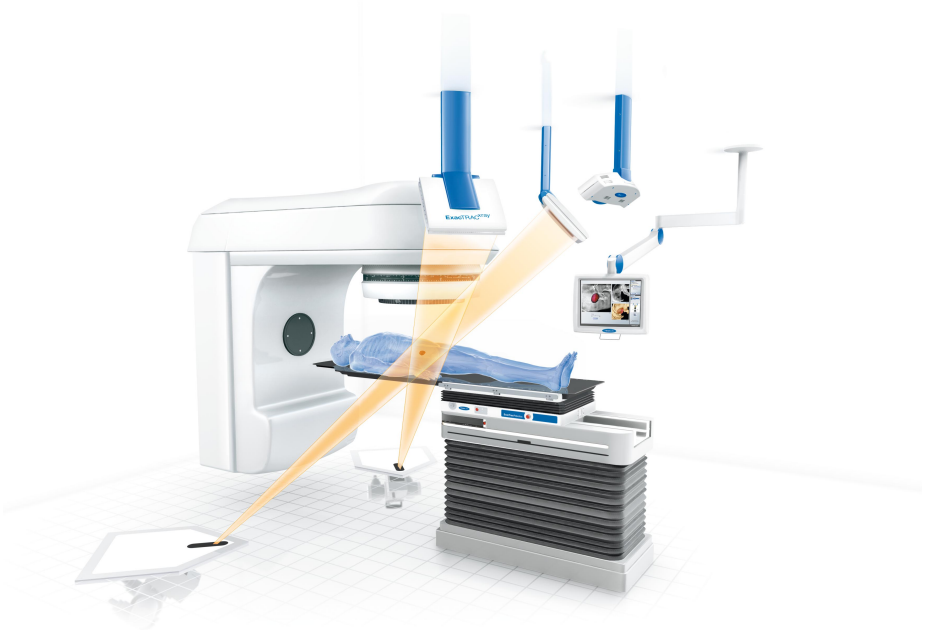

Figure 3.1: The BrainLab ExacTrac system. The two X-ray sources can be used for tracking an implanted gold fiducial marker. Image Courtesy of BrainLab, Inc. All rights reserved.

in external/internal motion correlation are accounted for, for example by use of respiratory correlated image guidance.

While beam gating is simpler than motion compensated delivery and might offer comparable accuracy, the total delivery time will be prolonged for the same beam-on time (Fox et al. 2007).

D'Souza et al. 2005 conducted experiments with a robotic couch, moving the patient according to breathing pattern in other to keep tumour location constant in relation to the linac. Besides being uncomfortable for the patients, such a system might inflict additional patient motion in itself.

As an alternative to radiopaque markers and X-ray imaging, electromagnetic (EM) transponders can be implanted near tumours and form the basis for low-latency tumour tracking without need for additional ionizing radiation (Sawant et al. 2009). Compared to the methods combining intermittent X-ray based tracking of an internal marker and constant feedback from an external surrogate, EM based systems provide constant feedback directly from the internal marker

in real time.

Generally, use of implantable markers is undesirable as it is an invasive procedure adding risk of infection, stress of the patient and additional labour. Often, the marker is not implanted in the tumour itself, but in nearby soft tissue due to the risk of spreading tumour cells during the procedure. During the treatment, a marker might migrate in the tissue causing a changed relation to tumour position. In addition, studies have reported poor correlation between internal and external markers for some tumour sites. Feng et al. 2009 reported poor correlation between the position of pancreatic tumours and the abdominal wall when breathing, as well as substantial deformation of tumour borders. For patients with lung tumours, Koch et al. 2004 reported good correlation (0.87 ± 0.23) between lung-vessel motion in the superior-inferior direction and poor correlation (0.44 ± 0.27) in the anterior-posterior direction. Significant intersubject variability was observed. The authors concluded that the motion of an external fiducial may not correlate fully with, or predict, internal lung motion.

Another general concern is that OAR motion might be uncorrelated or not accounted for when adapting the field based on tumour position alone. This factor needs to be taken into consideration during planning.

4D planning scans can form the basis of a 4D treatment plan where tumour position and shape are correlated to breathing phases as well as position of an external marker (Vedam et al. 2003b). Keall et al. 2005 demonstrated how such a 4D plan can be used for dynamic multileaf collimator (DMLC) based motion tracking. DMLCs are dynamic in the sense that they can adapt treatment beam shape during fraction delivery. A real-time external marker respiration signal is fed to the DMLC controller and the DMLC is adjusted according to position and shape for the corresponding breathing phase. To keep workload down, the target contours were defined on the end-inspiration CT image and deformed to the remaining breathing cycle scans using deformable image registration. For the test case they reported dose reductions for the spinal cord, heart and lungs.

If breathing pattern changes during treatment, 4D replanning might be indicated. As weekly or daily 4D CT does add significant dose to the patient, 4D MRI might be more appropriate for that purpose, depending on tumour site as well as availability.

3.2 4D CT imaging and tomographic image registration

4D CT scans are normally acquired using conventional scanning hardware. Fan-beam based CT scanners acquire one axial slice at a time. When acquiring and reconstructing 4D scans, a number of axial slices are sequentially acquired for each axial position and subsequently sorted into a limited number of breathing phase bins. Inaccurate sorting might lead to tissue discontinuity artifacts in the reconstructed CT volumes. This is especially seen at mid-inspiration or mid-expiration phases (Zeng et al. 2007).

Lyksborg et al. 2010 estimated a CT reference volume as well as a 4D B-spline deformation field using an optimisation method that included scan re-binning estimation.

Zeng et al. 2007 proposed to model motion, based on CBCT projections, as deformation of a prior 3D CT scan. Using this deformation from orbiting views (DOM) method, motion is modelled from slowly rotating X-ray cone-beam projection views and not through the use of markers. A breath-hold CT scan is deformed using a B-spline deformation model in order to optimise similarity between modeled projection views of the deformed volume and actual projections acquired at different breathing cycles. An advantage over traditional 4D CT is that discontinuity artifacts are avoided since correlation between internal anatomy and position of an external marker is not assumed.

However, the development in CT scanner hardware, with the recent advent of scanners with 320 detector rows, 16 cm axial coverage and 0.275 second rotation time is likely to reduce this particular kind of artefact.

Sarrut et al. 2006a proposed to acquire only inhale and exhale breath-hold scans and simulate intermediary breathing phase volumes by deformable image registration of the breath-hold scans with subsequent vector field interpolation. The benefit of this approach is reduced imaging dose, compared to acquiring all axial slices at all breathing phases. As motion during acquisition is limited during breath-hold, motion blurring should be reduced compared to free breathing acquisition. If the 4D scan is to be used for planning of DMLC based delivery one disadvantage of this approach is the lack of correspondence between simulated breathing phase anatomy and the position of an external marker. The same holds for the DOM reconstruction method.

Li et al. 2011 demonstrated that low-latency 3D tumour localisation based on single CBCT projections is possible. Deformation vector fields between a ref-

erence breathing phase and other breathing phases can be represented by a few eigenvectors and coefficients obtained by PCA. Now, for each acquired cone-beam projection, PCA coefficients are estimated that correspond to a deformation of the 3D volume producing a computed projection similar to the actual projection. The disadvantage of this method might be limited modelling capability when encountering motion patterns not previously experienced.

3.3 MRI low-latency guidance

In recent years, integrated MRI-radiotherapy systems have been developed as described in Section 1.4.3. These systems offer fast intrafraction imaging suitable for both beam gating (Crijns et al. 2011) and motion compensation (Ries et al. 2010; Cerviño et al. 2011; Crijns et al. 2012; Yun et al. 2012b; Yun et al. 2012a).

For tumour tracking, acquisition of high-quality live 3D images and subsequent low-latency DIR would be optimal. This is currently not feasible due to the lack of appropriate MRI acquisition sequences and DIR algorithms.

Crijns et al. 2012 tracked 1D motion using a DMLC equipped MRI-linac prototype. Motion tracking was based on edge detection on pencil-beam navigators Stam et al. 2012. This work primarily aims to prove that fast imaging, motion detection and DMLC control for motion compensated delivery is possible using MRI-linac systems.

Cerviño et al. 2011 suggested the use of template matching for real-time lung tumour tracking in sagittal cine-MRI scans. An inherent drawback of tracking a 3D structure in a 2D plane is the inability to detect out-of-plane motion. They suggest addressing out-of-plane motion by surrogate tracking of the diaphragm. Yun et al. 2012b investigated the use of an intra-fractional lung tumour auto-contouring algorithm for a phantom study using sagittal cine-MRI planes. Yun et al. 2012a describes how the auto-contouring algorithm of Yun et al. 2012b can be extended with an artificial neural network (ANN)-based motion prediction algorithm.

Ries et al. 2010 performed 3D target tracking by combining 2D-plane imaging with prospective slice tracking based on pencil-beam navigator sequences. The effect of the update latency was reduced using a Kalman-predictor for trajectory anticipation. One limitation they find is that since the detected beam signal is predominantly spin-density weighted, it suffers from poor tissue contrast, which can potentially lead to poor tracking performance.

In the future, MRI-radiotherapy systems could facilitate non-invasive, non-surrogate based, low-latency tumour motion tracking with no additional imaging radiation dose. While 'real-time' deformation in a 2D plane could be determined, such information will in many cases be of limited value due to the unknown out-of-plane deformation. Information on 3D deformation can not be achieved directly due to current limitations in hardware and/or lack of appropriate MRI sequences. It might be possible to model lung deformation using PCA and infer 3D deformation in a fashion similar to that described by Li et al. 2011 for cone-beam projections.

Chapter 4

Contributions

This PhD study comprises the following peer-reviewed contributions:

T. Bjerre, M.F. Hansen, A.K. Due, S. Korreman, L. Specht and R. Larsen. 'Tumor annihilation modeling for non-diffeomorphic registration of planning and follow-up CT scans'. In: *Radiotherapy and Oncology*, 96 (2010), pp. S335-S336.

T. Bjerre, M.F. Hansen, W. Sapru, P. Munck af Rosenschöld, M. Aznar, L. Specht and R. Larsen. (2011). 'Contour Propagation With Riemannian Elasticity Regularization'. In: *International Journal of Radiation Oncology * Biology * Physics*, 81.2 (2011), pp. S807.

T. Bjerre, M.O. Fogtmann, M. Aznar, P. Munck af Rosenschöld, L. Specht and R. Larsen. 'Spatially varying Riemannian elasticity regularization: Application to thoracic CT registration in image-guided radiotherapy'. In: *Biomedical Imaging (ISBI), 2012 9th IEEE International Symposium on*, pp. 1224-1227.

T. Bjerre, M. Aznar, P. Munck af Rosenschöld, L. Specht, R. Larsen, M.O. Fogtmann. 'Demons registration of CT volume and CBCT projections for adaptive radiotherapy: Avoiding CBCT reconstruction'. In: *Radiotherapy and Oncology*, 103 (2012), pp. S561-S562.

M.M. Clausen, A.E. Hansen, T. Larsson, P. Munck af Rosenschöld, T. Bjerre, M.C. Aznar, A. Kjær, A.T. Kristensen, F.J. McEvoy, S.A. Engelholm. 'Influence of tracer and imaging time-point on radiotherapy dose painting of spontaneous canine tumours'. In: *Radiotherapy and Oncology* 103 (2012), pp. S498.

T. Bjerre, T. Kim, P. Munck af Rosenschöld, M. Aznar, L. Specht, R. Larsen and P. Keall. 'A Feasible Real-time Multiplane MRI-linac Guidance Strategy'. In: *International Journal of Radiation Oncology * Biology * Physics*, 84.3 (2012), pp. S719.

T. Bjerre, S. Crijns, P. Munck af Rosenschöld, M. Aznar, L. Specht, R. Larsen and P. Keall. 'Three-dimensional MRI-linac intra-fraction guidance using multiple orthogonal cine-MRI planes'. In: *Physics in medicine and biology*, 58.14 (2013), pp. 4943-4950.

T. Bjerre, K. Conradsen, M. Aznar, P. Munck af Rosenschöld, L. Specht, R. Larsen. 'Modeling tumor size and density changes during chemoradiation therapy for head and neck cancer'. In: Submitted.

Chapters 6, 7, 8 and 9 present selected peer-reviewed contributions. They are all re-formatted according to the template of this thesis and are available in original form online and in print.

In the following, introductions to these select contributions are given.

Modeling tumor size and density changes during chemoradiation therapy for head and neck cancer

The purpose of this work was to investigate changes in total GTV volume and density for 10 HNCA patients during IGRT. For the investigated tumours, changes in logarithmic volume were described well by a linear function with patient-specific slope and intercept. While changes in GTV volume have previously been documented, changes in GTV density have not. Changes in density were well described by a linear function with patient-specific slope and intercept. Density changes are relevant as delivered dose to a tissue and calculated dose distributions rely on density. Furthermore, tumour density changes might be indicative of treatment response in the same sense as volume changes are.

Spatially Varying Riemannian Elasticity Regularization: Application to Thoracic CT Registration in Image-Guided Radiotherapy

This work explores how spatially varying elasticity parameters can be employed in image registration in order to encourage bone rigidity and local tissue volume change only in the GTV and the lungs. This is highly relevant for image registration in ART, especially when modelling significant tumour volume changes.

Demons Registration of CT Volume and CBCT Projections for Adaptive Radiotherapy: Avoiding CBCT Reconstruction

This work is related to research described in Section 3.2. CBCT quality is usually sub-par to that of CT. As such, it is feasible to model the CBCT reconstruction as a deformation of a planning CT of the same patient. Previous efforts have employed B-spline deformation models. Here, a non-parametric diffusion based deformation model is employed as a proof-of-concept. This opens the door to the use of more advanced non-parametric image registration algorithms such as diffeomorphic demons (Vercauteren et al. 2009) or the use of specialised anisotropic regularisation for modelling sliding organs (Pace et al. 2011). The described framework employs a parallel implementation of the forward- and back-projector described by Long et al. 2010.

A significant advantage of modelling the CBCT reconstruction as a deformation of a planning CT, is that no sub-sequent image registration is needed in order to obtain the deformation which can subsequently be employed for contour propagation in ART.

Three-dimensional MRI-linac intrafraction guidance using multiple orthogonal cine-MRI planes

This work is related to intrafraction image guidance with MRI-radiotherapy devices. As these devices offer close to real-time imaging without any additional ionising radiation to the patient, constant image-based guidance is possible without any undesirable effects for patients. An added benefit of MRI based tracking is that it is possible without the need for implanting fiducial markers.

Previous research on this topic has demonstrated how single plane cine-MRI can be used for tumour tracking. Here, it is demonstrated how multiple, orthogonal slices can form the basis for reliable 3D soft tissue tracking.

Chapter 5

Discussion and conclusion

As anatomical and functional imaging of tumours improve, so does our investigation into adaptive radiotherapy planning and intrafraction motion management. Both techniques allow for reduced treatment margins and dose escalation to the target volume. Improved image-guidance is the necessary basis for increases in TCP and reductions in NTCP.

This thesis presents selected contributions with applications in support of robust CT and CBCT based treatment replanning and real-time MRI based intrafraction guidance.

In the contribution titled "Modeling Tumor Size and Density Changes in Head and Neck Cancer during Treatment with IGRT", it is shown that changes in tumour density were well described by linear function with patient-specific slope and intercept, for ten head & neck cancer (HNCA) patients. This might be of particular interest for proton therapy as delivered dose to a tissue and calculated dose distributions rely on density. Furthermore, tumour density changes might be indicative of treatment response.

In the contribution titled "Spatially Varying Riemannian Elasticity Regularization:
Application to Thoracic CT Registration in Image-Guided Radiotherapy", it is demonstrated how spatially varying elasticity parameters can be employed in

image registration to encourage bone rigidity and local tissue volume change only in the GTV and the lungs. This is highly relevant in adaptive radiotherapy (ART) when modelling significant tumour volume changes. While the results were promising, one concern is that additional modelling parameters are introduced which need to be optimised.

In the contribution titled "Demons Registration of CT Volume and CBCT Projections for Adaptive Radiotherapy: Avoiding CBCT Reconstruction", it is described how CBCT reconstruction can be modelled as a deformation of a planning CT scan of the same patient, using a non-parametric diffusion based deformation model, opening the door to the use of a number of advanced non-parametric algorithms. An advantage of reconstruction by deformation is that no additional image registration is needed in order to obtain the deformation which can subsequently be employed for contour propagation in ART.

In the contribution titled "Three-dimensional MRI-linac intra-fraction guidance using multiple orthogonal cine-MRI planes", it is demonstrated how MRI-radiotherapy devices have the potential to offer near real-time intrafraction imaging without any additional ionising radiation. It is detailed how the use of multiple, orthogonal slices can form the basis for reliable 3D soft tissue tracking. An important limitation of this method is that local rigidity is assumed. As such, the method does not account for any deformations, nor will it be possible without intrafraction volume imaging. This, however, is true for all intrafraction tracking methods that do not model deformation based on prior volume imaging.

For large-scale treatment plan adaptation to be feasible, in-room imaging, image registration, and replanning procedures need to be both fast and robust. In reality, these qualities are often contradictory and the greatest challenges are to secure reliable contour propagation and high quality replanning while keeping preparation time down in order to minimise patient discomfort and maximise clinical efficiency. With the advent of comparatively inexpensive CPU/GPU scientific computing clusters, implementation and clinical use of robust but computationally expensive algorithms might be feasible in the near future. Parallel programming is still an evolving field that is highly likely to provide significant contributions before long.

In recent years effort has been increased in the field of intrafraction guidance. Commercial systems based on tracking of internal and external markers are readily available but research into next generation devices and systems is ongoing. Currently, MRI guidance seem to be the next logical evolutionary step in the pursuit of real-time image-based guidance, as it has the potential to enable constant image-based target tracking without subjecting the patient to additional ionizing radiation.

Part II

Selected Peer-Reviewed Contributions

Chapter 6

Modeling tumor size and density changes during chemoradiation therapy for head and neck cancer

T. Bjerre, K. Conradsen, M. Aznar, P. Munck af Rosenschöld, L. Specht, R. Larsen. 'Modeling tumor size and density changes during chemoradiation therapy for head and neck cancer'. In: Submitted.

Abstract

Introduction: We analyze and model changes in tumor radiodensity as well as tumor size for ten head and neck cancer patients during their course of treatment based on PET/CT planning scans and CT replanning scans. **Methods:** We compare (up to) second order polynomial regression models for repeated measurements with patient specific as well as population specific parameters. **Results:** For the patients included in this study, changes in both tumor size and radiodensity were well described with linear regression models with patient specific bias and slope. **Conclusions:** Significant changes in both volume and

radiodensity were observed. In addition to tumor volume changes, tumor radiodensity changes might need to be taken into account if/when re-planning patients in adaptive photon radiotherapy and could be of substantial importance in adaptive proton therapy as dose distributions are highly dependent on changes in tissue density.

6.1 Introduction

Image-guided intensity-modulated radiation therapy (IG-IMRT) planning often relies on both anatomical and functional imaging. In fractionated radiotherapy, a patient's treatment course may span up to 8 weeks. Image-guidance is typically employed during the treatment course to position the patient according to their treatment planning PET-CT scan in effort to avoid changes to the prescribed dose distribution. Exact positioning, however, may not account for possible interfraction changes in the anatomy, including general weight loss, tumor shrinkage/progression, oedema, bladder filling, bowel peristalsis, etc. These changes are traditionally accounted for by adding appropriate margins to the target volume. Wider margins ensure that the prescribed dose is delivered to the intended volume but also inevitably increases dose to organs at risk (OAR), thereby increasing the normal-tissue complication probability (NTCP). (Verellen et al. 2007)

Regular interfraction treatment plan adaptations can be used to improve target accuracy, and thereby increase conformality by minimizing the use of margins. Treatment plan adaptation can occur on different time-scales: real-time to account for acute changes such as breathing motion, and periodic to account for more gradual changes such as weight loss.

Patients are typically positioned on the treatment table using laser guidance based on external anatomy. Image-guidance is then used to verify the internal anatomy. For this purpose, 2D transmission scans acquired using the onboard cone-beam CT (CBCT) scanner are co-registered to the planning CT scan. While reconstructed 3D CBCT scans offer information about anatomical changes they are often not easily co-registered to CT scans for direct comparison as they do not provide the same image contrast, and often have beam-hardening, metal or motion artifacts. Ding et al. 2007 concluded that CBCT images are suitable for analyzing significant changes in anatomy and determine dosimetric consequences for photon radiation therapy, while it is a challenging task to accurately delineate tumor and organs using CBCT images due to the image quality. Additional planning CT may be necessary to perform IMRT re-planning at present in order to accurately delineate tumor and organs.

In head and neck cancer (HNCA) it is critical to minimize margins in order to spare nearby OAR. Most important to spare is the spinal cord, which should be kept below 50 Gy. Other organs important for the patientsâ€™ quality of life are the parotid and the submandibular salivary glands, which should be kept below a mean dose of 26 and 46 Gy, respectively. The mandible, the constrictor muscles of the pharynx, and the larynx are also important organs to spare.

Tumor size, but not density, is a response evaluation criterion in solid tumors (RECIST). However, when tumor tissue responds and becomes necrotic, the tumor volume might be unchanged while the density changes. While some studies have investigated tumor density changes during the course of chemotherapy (Choi et al. 2004; Faivre et al. 2011), studies of systematic monitoring of density changes during the course of (chemo)radiotherapy have not been performed to our knowledge. Knowledge about tumor density changes during radiotherapy might be valuable for treatment monitoring. Furthermore, significant tissue attenuation changes might influence adaptive treatment planning.

In this study we analyze and model changes in tumor size as well as tumor (radio)density for ten HNCA patients during their course of treatment. We base our observations on CT scans acquired regularly during the course of the treatment as true Hounsfield unit (HU) values are needed to study density changes.

6.2 Methods

6.2.1 Data

This study includes ten HNCA patients: three oropharyngeal cancers (patients 1,4,6), two oral cavity cancers (patients 2, 7), two hypopharyngeal cancers (patients 3, 9), two laryngeal cancers (patients 8,) and one cancer of unknown primary (patient 5). All patients were treated with chemoradiotherapy.

For each patient, PET-CT planning scans were acquired as well as 2-4 re-planning CT scans for each patient during the course of the treatment (14-39 days after first fraction). For each patient the gross tumor volume (GTV) was delineated on the planning PET-CT. The GTV delineations were subsequently propagated from the planning CT to each re-planning CT using manual contouring by an experienced radiation oncologist. Manual contouring was performed by pasting the set of contours from the planning CTs onto the re-scans and sub-

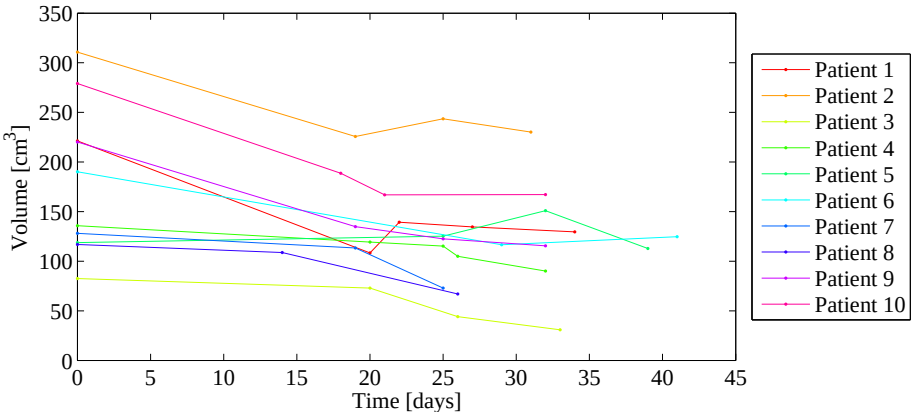

Figure 6.1: Delineated tumor volumes as a function of time during treatment

sequently adapting them to reflect actual anatomical changes. For the planning PET-CT scans, the delineated GTVs were between 83 and 311 cm^3.

For each patient, Figure 6.1 shows the delineated tumor volume as a function of time (days). The measured volumes are normalized by logarithmic transformation, in order to reduce the dependence on delineation accuracy that inherently has greater influence on smaller volumes than larger ones. Furthermore, Looney et al. 1975 and Kovacs et al. 1976 demonstrated that following irradiation, the growth rate of tumors is approximately linear (and negative) on a logarithmic scale, after an initial delay in response. Figure 6.2 shows the logarithmic tumor volumes as a function of time.

Preliminary investigations showed that the histogram of HU values of the GTVs followed a Gaussian distribution. For each delineated volume, a Gaussian distribution function was fitted to the histogram of HU values and the Gaussian distribution mean value was used as a representation of the tumor radiodensity. For each patient, Figure 6.3 shows the development of tumor radiodensity over time.

6.2.2 Repeated measurements model

For the acquired data of logarithmic tumor volumes and tumor densities we perform an analysis of variance investigation for repeated measurements using SAS software. The aim of the analysis was to investigate how time-dependence can be modelled for changes in logarithmic tumor volume and tumor density.

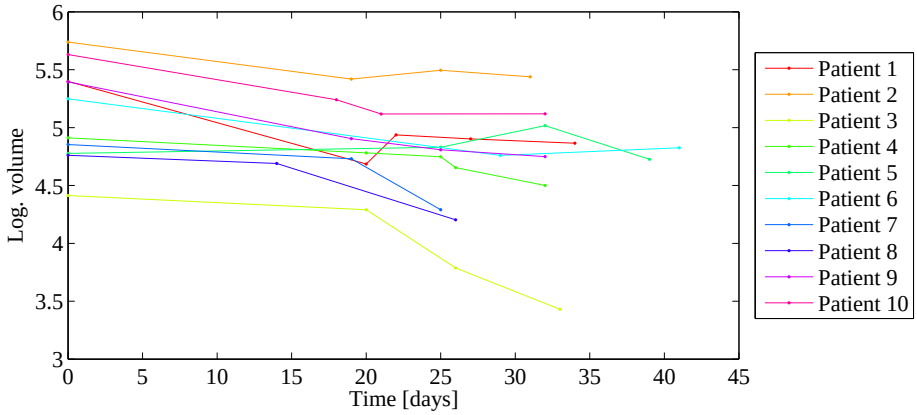

Figure 6.2: Logarithmic tumor volumes as a function of time during treatment

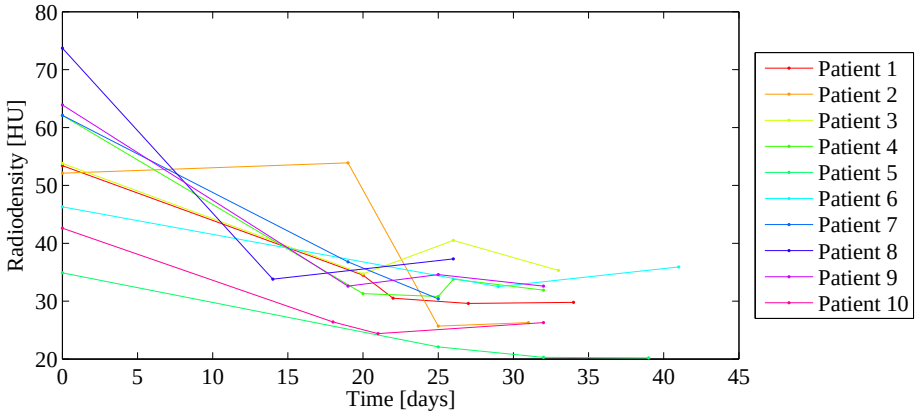

Figure 6.3: Tumor radiodensity as a function of time during treatment

We compare (up to) second order polynomial regression models with patient specific parameters as well as models with population specific parameters.

The basic model for changes in logarithmic tumor volume and tumor density for patient i, where $i = 1, ..., k$ is

$$\boldsymbol{Y}_i = \begin{bmatrix} Y_{i,1} \\ \vdots \\ Y_{i,n_i} \end{bmatrix} = \begin{bmatrix} 1 & t_{i,1} & {t_{i_1}}^2 \\ \vdots & \vdots & \vdots \\ 1 & t_{i,n_i} & {t_{i,n_i}}^2 \end{bmatrix} \begin{bmatrix} \alpha_i \\ \beta_i \\ \gamma_i \end{bmatrix} + \boldsymbol{\varepsilon}_i \tag{6.1}$$

or

$$\boldsymbol{Y}_i = \boldsymbol{x}_i \boldsymbol{\theta}_i + \boldsymbol{\varepsilon}_i \tag{6.2}$$

where $\boldsymbol{\varepsilon}_i$ has the variance-covariance matrix

$$D(\boldsymbol{\varepsilon}_i) = \boldsymbol{R}_i = \sigma^2 \begin{bmatrix} 1 & \dots & \rho^{|t_{i,1} - t_{i,n_i}|} \\ \vdots & & \vdots \\ \rho^{|t_{i,1} - t_{i,n_i}|} & \dots & 1 \end{bmatrix} \tag{6.3}$$

We assume that $\boldsymbol{Y}_i$ is normally distributed with mean $\boldsymbol{x}_i \boldsymbol{\theta}_i$ and variance-covariance matrix $\boldsymbol{R}_i$, and that $\boldsymbol{Y}_1, ..., \boldsymbol{Y}_k$ are independent. This gives the combined model

$$\begin{bmatrix} \boldsymbol{Y}_1 \\ \vdots \\ \boldsymbol{Y}_k \end{bmatrix} = \begin{bmatrix} \boldsymbol{x}_1 & \dots & 0 \\ \vdots & & \vdots \\ 0 & \dots & \boldsymbol{x}_k \end{bmatrix} \begin{bmatrix} \boldsymbol{\theta}_1 \\ \vdots \\ \boldsymbol{\theta}_k \end{bmatrix} + \begin{bmatrix} \boldsymbol{\varepsilon}_1 \\ \vdots \\ \boldsymbol{\varepsilon}_k \end{bmatrix} \tag{6.4}$$

or

$$\boldsymbol{Y} = \boldsymbol{x}\boldsymbol{\theta} + \boldsymbol{\varepsilon} \tag{6.5}$$

with

$$D \begin{bmatrix} \boldsymbol{\varepsilon}_1 \\ \vdots \\ \boldsymbol{\varepsilon}_k \end{bmatrix} = \begin{bmatrix} \boldsymbol{R}_1 & \dots & 0 \\ \vdots & & \vdots \\ 0 & \dots & \boldsymbol{R}_k \end{bmatrix} = \boldsymbol{R} \tag{6.6}$$

The random variable $\boldsymbol{Y}$ is then multivariate normally distributed, $\boldsymbol{Y} \in N_K(\boldsymbol{x}\boldsymbol{\theta}, \boldsymbol{R})$ where K it the total number of observations across all patients. Thus we may use standard likelihood theory for estimation of parameters and testing of hypotheses.

For modeling changes in logarithmic tumor volumes as well as changes in tumor density (expressed in Hounsfield units) we investigate each of the models displayed in table 6.1.

Model	Fixed effects mean values	Number of mean value parameters	Description
M_1	$\alpha_i + \beta_i t_{i,y} + \gamma_i {t_{i,j}}^2$	30	Individual bias Individual slope Individual quad. term
M_2	$\alpha_i + \beta_i t_{i,y} + \gamma {t_{i,j}}^2$	21	Individual bias Individual slope Shared quad. term
M_3	$\alpha_i + \beta_i t_{i,y}$	20	Individual bias Individual slope No quad. term
M_4	$\alpha_i + \beta t_{i,y}$	11	Individual bias Shared slope No quad. term
M_5	α_i	10	Individual bias No slope No quad. term

Table 6.1: Investigated models for changes in logarithmic tumor volumes as well as changes in tumor densities

6.2.3 Model selection for ordinary least squares and repeated measurements analysis

The most general model for a polynomial fit of the data measured on the 10 patients is an individually-fitted quadratic functions. However, for three of the patients there were only three data points collected. The quadratic functions therefore obtain a perfect fit. In total, the quadratic model has 30 parameters (plus uncertainty parameters) and we have 39 observations. Although we know in advance that this might be over-modeling the data, it is indeed possible to estimate all parameters. However, since a possible small value of the residual sum of squares very likely will be due to the over-fitting, we include models with quadratic terms only from inquisitive reasons with the prior knowledge that M_1 and M_2 are probably unreasonable for this number of data points.

We consider the models $M_1 - M_5$ obtained by increasing simplification of the previous models. We may perform a formal successive testing of hypothesis and alternatives

$$\mathrm{H}_0\text{: } E(\boldsymbol{Y}) \in M_t \text{ against } \mathrm{H}_1\text{: } E(\boldsymbol{Y}) \in M_{t-1}/M_t \text{ for } t = 1, ..., 4 \tag{6.7}$$

The hypothesis testing is done both by means of the usual F-test statistic known

from the general linear model, corresponding to $\rho = 0$ in the repeated measurements model, and by means of the asymptotic results for the likelihood ratio test statistic which in this case basically says that -2 log (likelihood ratio test statistic Q) under the null hypothesis will be asymptotically χ^2 distributed with degrees of freedom equal to the decrease in number of 'free' parameters from the more elaborate to the simpler model.

6.3 Results

6.3.1 Investigation of tumor volume changes

Table 6.2 presents the result of the GLM analysis using least squares fits with independent residuals. Table 6.3 presents the results of the repeated measurements analysis using maximum likelihood fits with autocorrelated residuals.

Model	# of mean value parameters	Degrees of freedom	Residual SS	F-statistic f	P(F > f)
M_1	30	9	0.108		
M_2	21	18	0.481	3.43	0.04
M_3	20	19	0.481	0.002	0.96
M_4	11	28	0.886	1.78	0.14
M_5	10	29	2.05	37.7	0.00

Table 6.2: Least squares fits with independent residuals for tumor volume changes. Model M_3 and M_4 are accepted.

Model	# of mean value parameters	Degrees of freedom	-2 log likelihood	Successive difference, sd	P(χ^2 > sd)
M_1	30		-119		
M_2	21	9	-60.8	58.0	0.000
M_3	20	1	-60.8	0.010	0.920
M_4	11	9	-37.1	23.7	0.005
M_5	10	1	-4.50	32.4	0.000

Table 6.3: Maximum likelihood fits with autocorrelated residuals (repeated measurements analysis) for tumor volume changes. Model M_3 is accepted.

It follows from Table 6.2 and 6.3 that we accept M_3 using both methods with 95% confidence[1] but only the classical GLM approach accepts M_4. As already stated above we are clearly in a repeated measurements situation, and as such we put the stronger emphasis on the result in table 6.3 and proceed to conclude that model M_3 is the simplest model adequately describing the development of the logarithmic tumor volumes. The estimated parameters for model M_3 for repeated measurements are presented in Table 6.4. Figure 6.4 shows the tumor volumes with M_3 regression models fitted. Figure 6.5 shows the distribution and cumulative distribution of $\hat{\beta}_i$ values for the M_3 repeated measurements model for tumor volume changes. Note that a normal distribution is assumed.

Patient	$\hat{\alpha}_i$	stderr$(\hat{\alpha}_i)$	$\hat{\beta}_i$	stderr$(\hat{\beta}_i)$
1	5.30	0.103	-0.016	0.004
2	5.71	0.105	-0.010	0.005
3	4.53	0.105	-0.028	0.005
4	4.95	0.105	-0.011	0.004
5	4.80	0.106	0.014	0.004
6	5.21	0.108	-0.012	0.004
7	4.90	0.109	-0.019	0.006
8	4.83	0.103	-0.021	0.006
9	5.36	0.105	-0.021	0.005
10	5.58	0.102	-0.017	0.005

Table 6.4: Estimated patient specific parameters (bias and slope) for tumor volume changes for M_3 repeated measurements model.

It follows that the main difference between the two situations is that the estimated errors on the parameters are smaller in the repeated measurements model, also explaining why we have stronger significance in that case. Furthermore we have for the estimated variance-covariance matrix, $D(\boldsymbol{\varepsilon}_i)$, that

$$\hat{\sigma}^2 = 0.012, \text{stderr}\left(\hat{\sigma}^2\right) = 0.003$$
$$\hat{\rho} = -0.238, \text{stderr}\left(\hat{\rho}\right) = 0.844$$

6.3.2 Investigation of tumor radiodensity changes

Table 6.5 presents the result of the general linear model (GLM) analysis of tumor radiodensity changes, using least squares fits with independent residuals. Table 6.6 presents the results of the repeated measurements analysis using maximum likelihood fits with autocorrelated residuals. We here take M_3 as starting point for our analysis as M_1 and M_2 over-model the data.

[1] As the test statistics are higher than 0.05

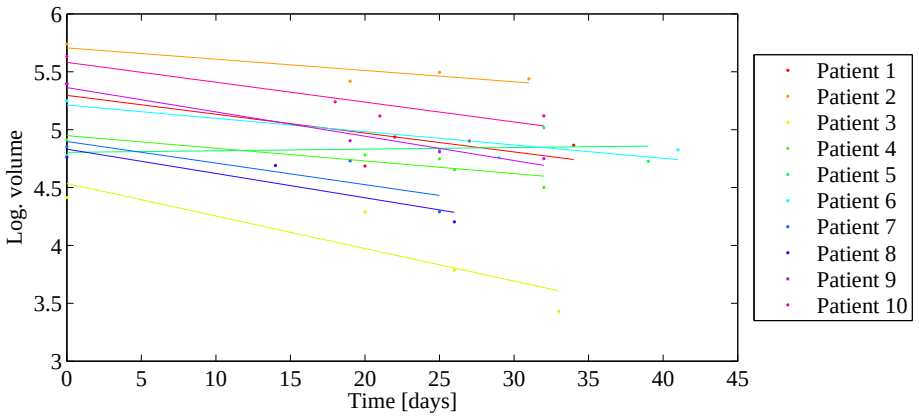

Figure 6.4: Delineated tumor volumes as a function of time during treatment, with M_3 linear regression models with patient specific bias and slope fitted.

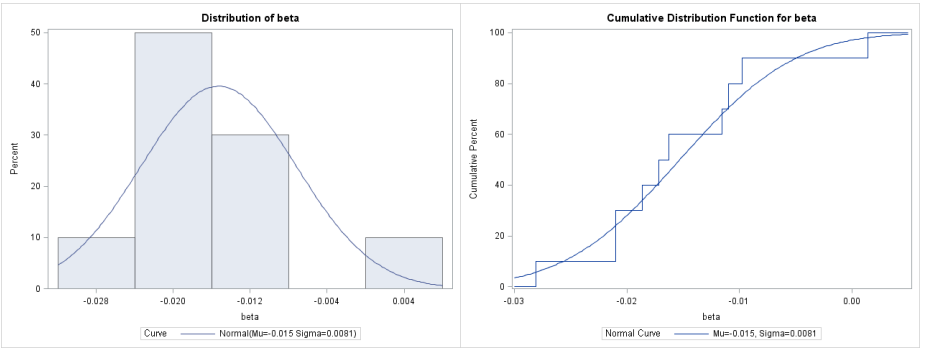

Figure 6.5: Distribution and cumulative distribution of $\hat{\beta}_i$ values for the M_3 repeated measurements model for tumor volume changes.

Model	# of mean value parameters	Degrees of freedom	Residual SS	F-statistic f	P(F > f)
M_3	20	19	971	6.34	
M_4	11	28	1657	1.49	0.221
M_5	10	29	4828	53.6	0.000

Table 6.5: Least squares fits with independent residuals for tumor radiodensity changes. Model M_3 and M_4 are accepted.

Model	# of mean value parameters	Degrees of freedom	-2 log likelihood	Successive difference, sd	$P(\chi^2 > sd)$
M_3	20		236		
M_4	11	9	256	20.3	0.016
M_5	10	1	292	36.6	0.000

Table 6.6: Maximum likelihood fits with autocorrelated residuals (repeated measurements analysis) for tumor radiodensity changes. Model M_3 is accepted.

It follows from Table 6.5 and 6.6 that only the classical GLM approach accepts M4. Since we clearly are in a repeated measurements situation, we put the stronger emphasis on the result in Table 6.6, and thus we conclude that model M_3 is the simplest model adequately describing the development of the logarithmic tumor radiodensity.

The estimated parameters for M_3 for repeated measurements are presented in Table 6.7. Figure 6.6 shows tumor radiodensities as a function of time, during treatment, with M_3 regression models fitted. It follows that the main difference between the two modeling approaches is that the estimated errors on the parameters are smaller in the repeated measurements model, also explaining why we have stronger significance in that case. Figure 6.7 shows the distribution and cumulative distribution of $\hat{\beta}_i$ values for the M_3 repeated measurements model for tumor radiodensity changes. Note that a normal distribution is assumed.

Patient	$\hat{\alpha}_i$	stderr$(\hat{\alpha}_i)$	$\hat{\beta}_i$	stderr$(\hat{\beta}_i)$
1	51.3	4.65	-0.757	0.196
2	56.2	4.74	-0.889	0.215
3	52.0	4.72	-0.550	0.203
4	59.0	4.74	-1.03	0.199
5	34.1	4.78	-0.404	0.170
6	45.1	4.86	-0.295	0.167
7	61.9	4.90	-1.28	0.271
8	67.5	4.62	-1.44	0.271
9	60.5	4.70	-1.03	0.210
10	39.7	4.57	-0.561	0.217

Table 6.7: Estimated patient specific parameters (bias and slope) for tumor radiodensity changes for M_3 repeated measurements model.

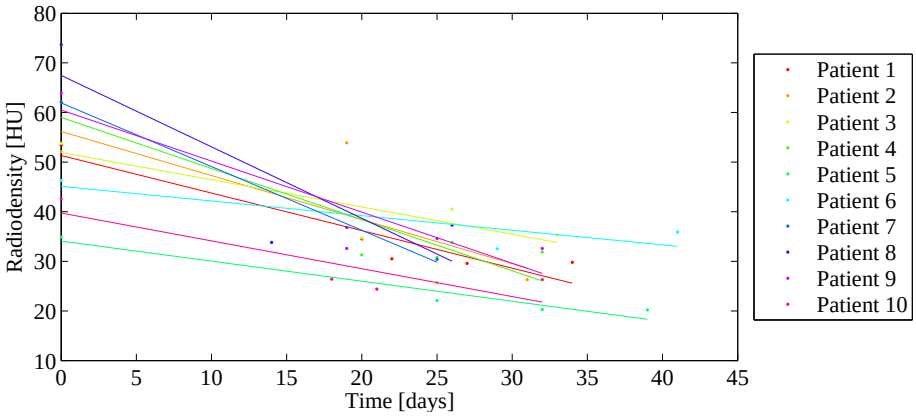

Figure 6.6: Tumor radiodensities as a function of time, during treatment, with M_3 linear regression models with patient specific bias and slope fitted.

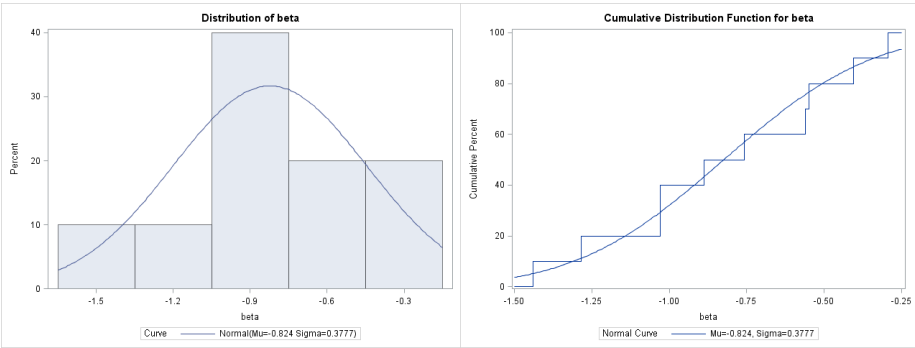

Figure 6.7: Distribution and cumulative distribution of $\hat{\beta}_i$ values for the M_3 repeated measurements model for tumor density changes.

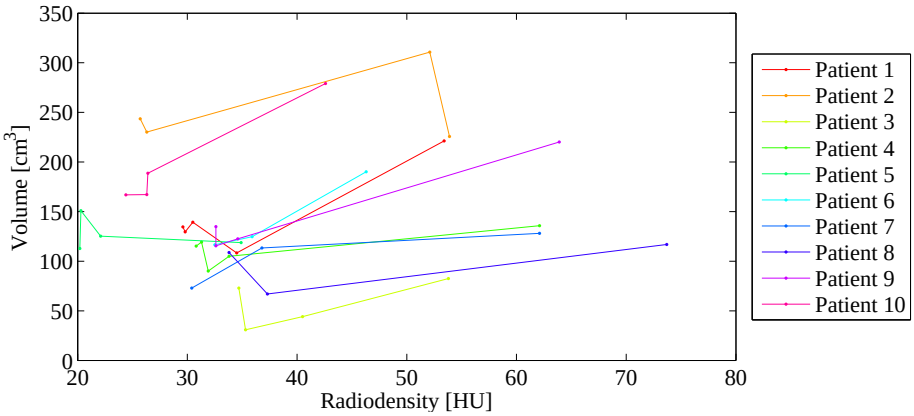

Figure 6.8: Tumor volume against tumor radiodensity for each patient.

6.3.3 Connection between tumor volume and radiodensity changes

Figure 6.8 shows tumor volume against tumor radiodensity for each patient. Figure 6.9 shows tumor volume plotted against radiodensity modeling residual for each patient, with a fitted linear regression line.

6.4 Discussion & Conclusions

We have modelled changes in tumor radiodensity and logarithmic tumor volume. Both datasets were best described using simple linear models with individual bias and slope, when modeled using a repeated measurement framework. This means that we see significant changes in both volume and radiodensity and that these changes do not happen at the same rate for all patients. Interestingly, using a GLM approach resulted in the acceptance of a simpler model (for this data set) than the repeated measurements approach. As the data clearly reflects a repeated measurements situation, we put the stronger emphasis on that result. It was clear from Figure 6.8 that tumor volumes do not decrease in size as a result of an increase in (radio)density. For all patients, even the one where tumor volume increased slightly, we observed a decrease in tumor radiodensity. From Figure 6.9 it can be seen that there is no correlation between tumor volume and tumor radiodensity that is not explained by the common correlation to the independent variable, time.

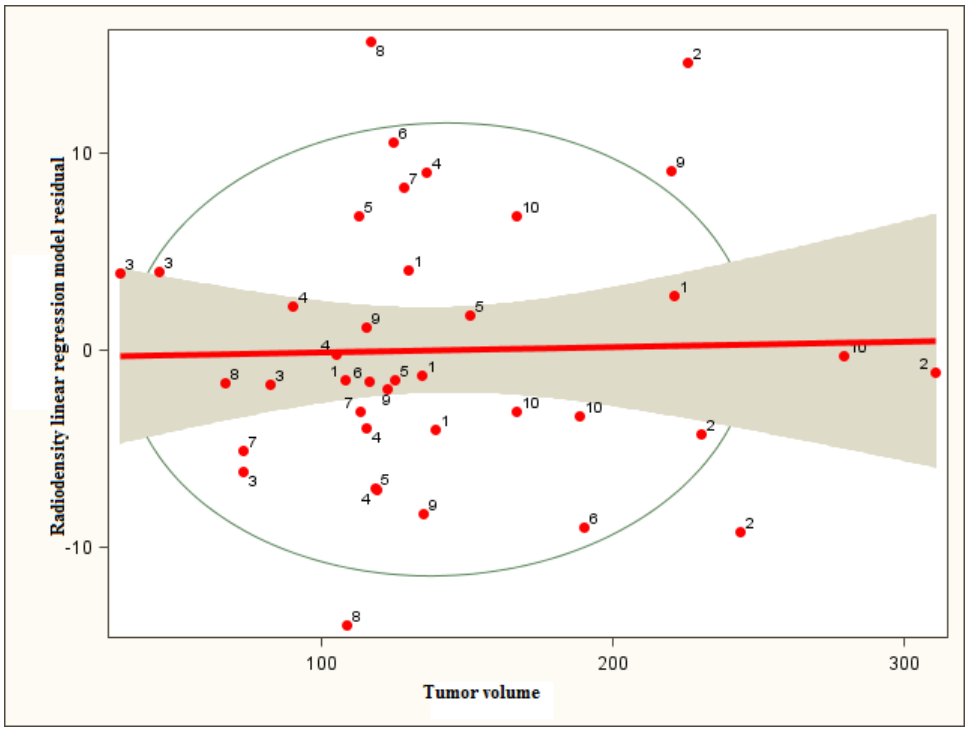

Figure 6.9: Tumor volume against radiodensity modeling residual for patient $i = 1, ..., 10$ indicated with numbers in the figure. A fitted linear regression line with 95% confidence interval is shown in red. The 75% prediction ellipsoid is shown in green.

It is noteworthy that tumor radiodensity changes during the course of radiotherapy have not previously been investigated, and that such changes might need to be taken into account if/when re-planning patients in adaptive photon radiotherapy, in addition to tumor volume changes. Tumor density changes might also be of substantial importance for proton therapy, as dose distributions are highly dependent on actual tissue density.

Chapter 7

Spatially Varying Riemannian Elasticity Regularization: Application to Thoracic CT Registration in Image-Guided Radiotherapy

T. Bjerre, M.O. Fogtmann, M. Aznar, P. Munck af Rosenschöld, L. Specht and R. Larsen. 'Spatially varying Riemannian elasticity regularization: Application to thoracic CT registration in image-guided radiotherapy'. In: *Biomedical Imaging (ISBI), 2012 9th IEEE International Symposium on*, pp. 1224-1227.

Abstract

For deformable registration of CT scans in IGRT we apply Riemannian elasticity regularization. We explore the use of spatially varying elasticity parameters to

encourage bone rigidity and local tissue volume change only in the GTV and the lungs. We evaluate the method on the point-validated 4DCT breathing thorax POPI-model and demonstrate its use and properties in registration of pre- and post-chemo CT scans for contour propagation in a Hodgkin lymphoma (HL) case showing significant tumor shrinkage. For the POPI-model we achieved a total mean target registration error (TRE) of 0.92 ± 0.49 mm. Using spatially varying regularization for the HL case, deformation was limited to the GTV and lungs.

7.1 Introduction

In IGRT, dose distribution is planned based on manual contouring of the tumor and critical normal tissues on a pre-treatment PET/CT scan. Conventional RT treatment is fractionated; patients receive a daily fraction of the total planned dose. Throughout the course of treatment, spatial changes of the patient may cause residual positional errors even after translational and rotational image guided corrections. Such changes include tumor shrinkage (Erridge et al. 2003; Barker et al. 2004), weight loss, organ filling and change in posture, all of which cause tissue deformation, ultimately disturbing the planned dose distribution. Hansen et al. 2006 concluded that adaptive replanning is essential for IMRT treatment for HNCA cancer to ensure proper dose to target volumes and critical tissues.

Manual tumor re-contouring on a daily basis is unfeasible due to the massive amount of physician time and effort required. Adaptive RT techniques allow for automatic, but preferably supervised, correction of these spatial changes on a daily basis. Contours of the GTV and critical tissues can be propagated by use of image registration, and the dose distribution can be updated accordingly.

Image registration is the process of determining a spatial transformation that establishes meaningful correspondence between all points in a pair or set of images; in this case between the planning PET/CT and a subsequent CT or CBCT scan. In general, image registration comprises 3 main aspects. **1**. Selecting an image transformation model, T. **2**. Selecting an objective function $\mathcal{F}_{obj}$, including an image (dis)similarity measure $\mathcal{D}$ and a regularization term $\mathcal{R}$ ensuring a plausible, invertible transformation. **3**. Selecting an optimization strategy for the objective function.

Here, we explore the use of the Riemannian elasticity model for regularization, proposed by Pennec et al. 2005. Based on a Hounsfield units (HU) threshold segmentation, Ruan et al. 2006 applied spatially varying regularization encour-

aging bone rigidity and Kabus et al. 2007 used spatially varying elasticity. In a similar fashion, we use spatially varying tissue regularization parameters, enabling us to encourage local rigidity and volume change. Specifically, we seek to exploit the a priori knowledge that volume change is likely to happen in the GTV.

We evaluate spatially varying Riemannian elasticity regularization on the POPI-model, a point-validated 4DCT breathing thorax data set, and further illustrate its use on a HL case with pre- and post-chemotherapy CT scans.

7.2 Data

7.2.1 POPI-model: 4DCT

The POPI-model is a point-validated 4DCT image data set of a breathing thorax. The dataset was acquired at the Léon Bérard Cancer Center & CREATIS lab, Lyon, France. It is available at `http://www.creatis.insa-lyon.fr/rio/popi-model` and is described by Vandemeulebroucke et al. 2007. The data set consists of ten volume images, each in a different phase of one breathing cycle. The images are cropped to volumes of $482 \times 360 \times 141$ voxels at a resolution of $0.98 \times 0.98 \times 2.0$ mm, including only the thorax. Forty landmarks have been manually annotated in each of the images. Performance is evaluated by calculating the TRE as the euclidean distance between the points annotated in the target scan and the deformed points from the reference scan (first phase). For images downsampled to a resolution of $2 \times 2 \times 2$ mm, a mean TRE for all scans of 1.24 ± 0.42 was achieved using a non-parametric Demons method from Sarrut et al. 2006b, inspired by Thirion 1998. A mean TRE of 1.04 ± 0.53 mm was achieved using a parametric, multi-scale implementation by Delhay et al. 2007 of the FFD deformation model by Rueckert et al. 1999. Glocker et al. 2011 reports a mean TRE of 0.96 ± 0.57 mm (on the downsampled data) using a discrete graph-based, multi-scale FFD method.

7.2.2 Hodgkin lymphoma case: Pre- and post-chemo CT

A HL patient with a very large mediastinal tumor burden was staged with a FDG PET/CT scan before the initiation of chemotherapy. Later, the patient was referred to RT, where a planning CT scan was acquired. In HL, the RT target volume is the PET-positive volume as it was defined on the staging (pre-chemotherapy) scan. However, between the staging and planning scan, the

tumor burden is likely to have been reduced considerably, the patient is likely to have lost weight and the posture is likely to vary. Automatic deformable registration and propagation of the PET-positive contour to the RT planning CT would be a valuable aid to the physician, when defining the radiation target volume.

7.3 Method

We applied a SSD driven FFD B-spline model (Rueckert et al. 1999) to register the staging and planning CT scans allowing for a subsequent mapping of the GTV contour to the planning CT. The use of the cubic B-spline deformation model is motivated partly by the existence of direct analytic continuous derivatives and partly by the inherent dimensionality reduction. We believe that the B-spline deformation model has enough descriptive power to capture the *true* underlying deformations between the scans as we are estimating the mapping between images of the same subject. In a multi-level framework, an L-BFGS (Liu et al. 1989) algorithm was applied to solve the matching problem, i.e.

$$\min_{\phi} \mathcal{D}(R, T \circ \phi) + \mathcal{R}(\phi), \tag{7.1}$$

where $\mathcal{D}$ is the SSD (di)similarity measure, R is the reference (staging CT), T is the target (planning CT), ϕ is the B-spline transformation and $\mathcal{R}$ is the regularization term.

Biological studies, e.g. (Hu 2006; Sarma et al. 2003), show that biological tissue is similar to rubber; nearly incompressible and compliant to shear. Thus a rubber-like deformation prior is suitable for same-subject registration when images are acquired temporally close. However, cancer patients are likely to have significant weight loss, have tumor shrinkage and tissue loss in proximity to the tumor regions which makes the incompressibility constraint invalid. Relaxing the incompressibility constraint transforms the rubber prior into a more general elasticity prior.

Linear elasticity matching (Broit 1981) has been widely used for spatial normalization but the lack of local rotation invariance can hinder optimal matching. Especially in HNCA imaging, the neck posture (bending in the neck) may cause the linear elasticity prior to over-regularize the deformation. We applied an *isotropic* Riemannian elasticity prior by Pennec et al. 2005, with spatially varying elasticity parameters as a trade-off between modelling capability and simplicity. The Riemannian elasticity prior is a *simple* weighted quadratic penalty on the Hencky strain tensor which inherits local rotational invariance and the

infinity energy limit approaches the *black-hole* deformation. While biological tissue is elastically anisotropic, anisotropic modeling requires many parameters which cannot be estimated from CT scans alone. Instead, isotropic behaviour is assumed, reducing the number of parameters to two – namely the usual Lamé parameters μ, λ, giving the isotropic Riemannian elasticity

$$\mathcal{R}_{rie}(\mu, \lambda; \phi) = \frac{\mu}{4} \sum_{i=1}^{N} \log^2 \varepsilon_i + \frac{\lambda}{8} \left(\sum_{i=1}^{N} \log \varepsilon_i \right)^2 , \tag{7.2}$$

where μ controls the amount of elastic potential due to shearing, and λ controls the amount of elastic potential due to local compression or expansion. ε_i are the principal stretches. In contrast to linear elasticity and Saint-Vernant Kirchoff elasticity λ is solely related to local volume change (Hansen 2009). The Lamé parameters are set experimentally for each tissue type (bone, soft tissue, lung) which are segmented from the planning CT using HU intensity thresholding. In addition, the Lamé parameters are set *low* in the GTV to allow for considerable shrinkage. The image maps of Lamé parameters are smoothed to get smooth elastic potential transitions.

7.4 Results

7.4.1 POPI-model

For the FFD transformation model, Glocker et al. 2011 used multi-level control point spacing of $40, 20, 10, 5$ mm. We have used two registration levels with 20 and 10 mm spacing. Additional registration levels did not improve performance. Level 1 used downsampling to $4 \times 4 \times 4$ mm and level 2 used downsampling to $2 \times 2 \times 2$ mm. Table 7.1 presents the registration results using both spatially constant and varying regularization. For spatially varying regularization, the provided segmentation of the lung was used together with a HU-based bone segmentation for assigning local Lamé regularization parameters. Rigidity was encouraged only for bone, by setting $\mu_{\text{bone}} \gg \mu_{\text{soft tissue}}, \mu_{\text{lung}}$. Volume change was encouraged only for lung by setting $\lambda_{\text{lung}} \ll \lambda_{\text{soft tissue}}, \lambda_{\text{bone}}$.

7.4.2 Pre- and post-chemo CT

For spatially varying regularization, triangulation-based GTV segmentation and HU-based segmentation of bone, soft tissue and lung was used for assigning

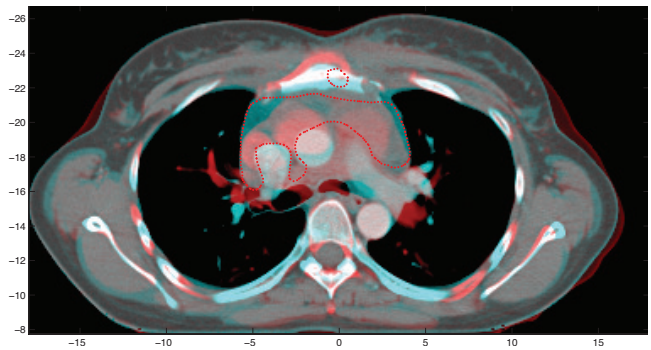

Spatially constant regularization

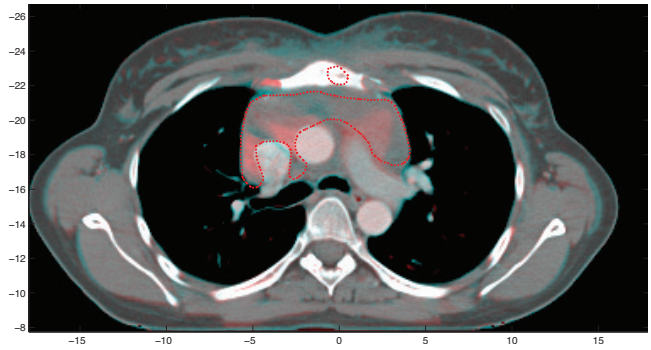

Spatially varying regularization

Figure 7.1: Overlay of transverse slice of pre-chemo CT and deformed post-chemo CT. The red, dotted line is the PET-positive contour.

Table 7.1: POPI-model registration results

#	Initial mean distance [mm]	mean TRE [mm] (spatially constant)	mean TRE [mm] (spatially varying)
1	0.48 ± 0.54	0.65 ± 0.33	0.64 ± 0.31
2	0.49 ± 0.62	0.65 ± 0.42	0.63 ± 0.39
3	2.19 ± 1.84	1.19 ± 0.68	1.19 ± 0.70
4	4.33 ± 2.54	1.01 ± 0.50	1.02 ± 0.50
5	5.75 ± 2.67	1.08 ± 0.62	1.08 ± 0.63
6	6.10 ± 2.96	0.98 ± 0.53	1.00 ± 0.54
7	5.03 ± 2.36	1.08 ± 0.50	1.09 ± 0.53
8	3.68 ± 1.59	0.80 ± 0.40	0.77 ± 0.41
9	2.07 ± 1.07	0.84 ± 0.42	0.82 ± 0.43
All	3.35 ± 2.82	0.92 ± 0.49	0.92 ± 0.49

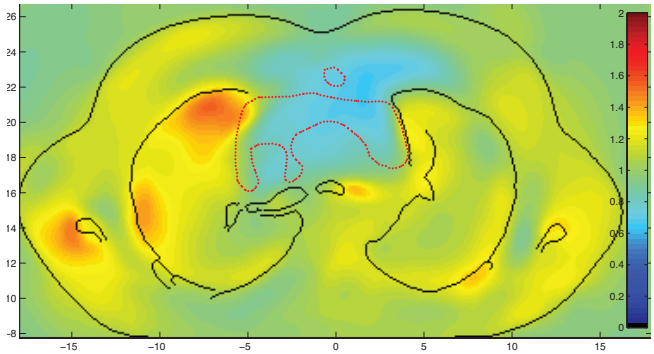

Spatially constant regularization

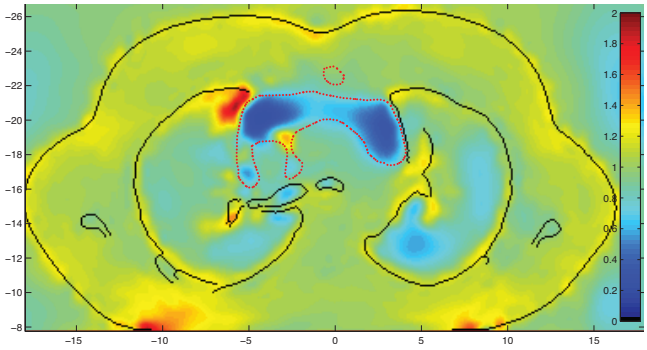

Spatially varying regularization

Figure 7.2: Volume change in the transverse slice in 7.1. Values of 1 indicate no local volume change. The black contour is gradients extracted from the CT.

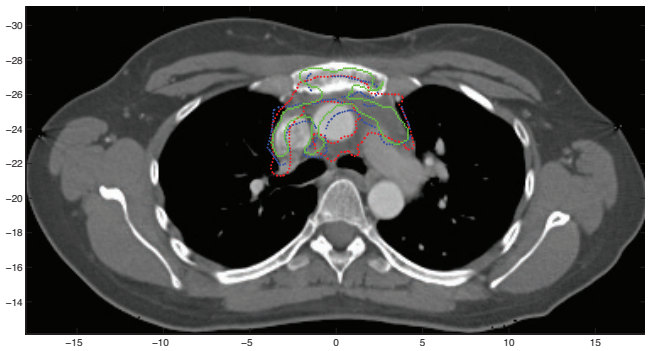

Figure 7.3: Post-chemo CT with manually propagated and adapted contour (red) and contours propagated automatically using spatially constant (blue) and varying (green) regularization.

local Lamé regularization parameters. Rigidity was encouraged only for bone, by setting $\mu_{\text{bone}} \gg \mu_{\text{soft tissue}}$. Volume change was encouraged for both GTV and lung by setting $\lambda_{\text{GTV}}, \lambda_{\text{lung}} \ll \lambda_{\text{soft tissue}}, \lambda_{\text{bone}}$. Figure 7.1 displays a fusion of a single transverse slice of the pre-chemo CT and the deformed post-chemo CT. Figure 7.2 shows the Jacobian determinant of the transformation field, i.e. the local volume change, in the same slice. The initial tumor volume was 140cm^2. Using spatially constant regularization, the volume of the propagated contour was 120cm^2. Using spatially varying regularization, the volume of the propagated contour was 99cm^2. Comparing segmentations from the propagated contours to a manual post-chemo GTV segmentation resulted in Dice similarity coefficients of 0.43 in both cases versus 0.39 using rigid registration.

7.5 Discussion & Conclusion

For the POPI-model we achieved a total mean TRE smaller than what has been reported in the literature. The standard deviation is also small. For the breathing phases with low initial mean distance, deformation resulted in a mean TRE larger than the initial distance. This was expected as the registration was based on downsampled images. The standard deviation, however, was significantly decreased in these cases. There was no difference between the results obtained using spatially constant and varying regularization, most likely due to the absence of significant volume changes. In that respect, this data set is not troublesome. For the HL case we demonstrated that local volume change can be encouraged in volumes where it is expected (GTV, lungs, etc.). The Dice similarity coefficients between the manual post-chemo GTV segmentation and

those based on deformable registration were relatively low, primarily due to the clinician choosing to include a larger area on the planning scan. Still, the coefficients were higher than that of the rigid registration, suggesting that this would be a better starting point for the clinician who is manually propagating and modifying the contour. By visual inspection it is apparent that qualitatively, the registration result using spatially varying regularization is superior. The method could very well be suitable for registration to low-quality scans with deranged image gradients, in order to minimize local volume change, e.g. CBCT scans for daily contour propagation in adaptive RT. As with all parametric image registration methods, the main drawback is parameter optimization. In this regard, the use of spatially varying regularization parameters is a further encumbrance.

Chapter 8

Demons Registration of CT Volume and CBCT Projections for Adaptive Radiotherapy: Avoiding CBCT Reconstruction

T. Bjerre, M. Aznar, P. Munck af Rosenschöld, L. Specht, R. Larsen, M.O. Fogtmann. 'Demons registration of CT volume and CBCT projections for adaptive radiotherapy: Avoiding CBCT reconstruction'. In: *Radiotherapy and Oncology*, 103 (2012), pp. S561-S562.

Purpose
In ART, the dose plan is adapted throughout the fractionation schedule to accommodate for anatomical changes. This can be achieved by deformable image registration of the planning PET/CT scan with segmented tumor and organs to daily CBCT scans. CBCT scans, are typically reconstructed using the filtered back-projection algorithm, which introduces significant artefacts, causing deteriorated image quality and registration results. We study the feasibility of per-

forming demons registration without tomographic reconstruction of the CBCT projections.

Materials
We demonstrate demons registration (Thirion 1998) of a CT volume and CBCT projections of the same subject. For simplicity, instead of measured projections, we used synthetic projections of the CT deformed by a known deformation. A volume from Vandemeulebroucke et al. 2007 was used [1]. The iterative registration is performed by repeating steps 1-4:

1. Simulate CBCT projections of deformed planning CT.
2. Back-project difference between simulated and measured projections.
3. Perform demons update based on back-projected difference.
4. Apply deformation to the planning CT.

We used an additive demons update schemes with adaptive fluidity (smoothing kernel width). For forward/back-projection, the separable footprints algorithm with trapezoid functions was applied. The similarity between the simulated and measured projections was measured as the SSD.

Results
Figure 8.1 shows a slice of; the CT volume (reference), the CT deformed by the known deformation (target), the relative Euclidean error of the true and estimated deformation fields, and the CT volume registered to the projections of the deformed CT. Interestingly, the deformation was accurately estimated from only 24 projections. The MSE between the target and registered image was $1.4 \cdot 10^{-3}$ HU^2. The mean absolute difference between the Jacobian determinant of the true and estimated deformation field was $4 \cdot 10^{-4}$. Time consumption was 11 min. using 8 2.3 GHz AMD Opteron cores.

Conclusion
In this feasibility study, using a known deformation and synthetic noise-less projection data, it was possible to estimate the deformation with good accuracy. For real projection data it might be necessary to use the mutual information similarity measure. Using few projections, daily dose burden could be decreased, or photon fluence for each projection increased. Time consumption was low compared to the alternative scheme of iterative reconstruction followed by registration, but can be reduced by further code parallelisation.

[1] The Léon Bérard Cancer Center & CREATIS Lab, Lyon France.

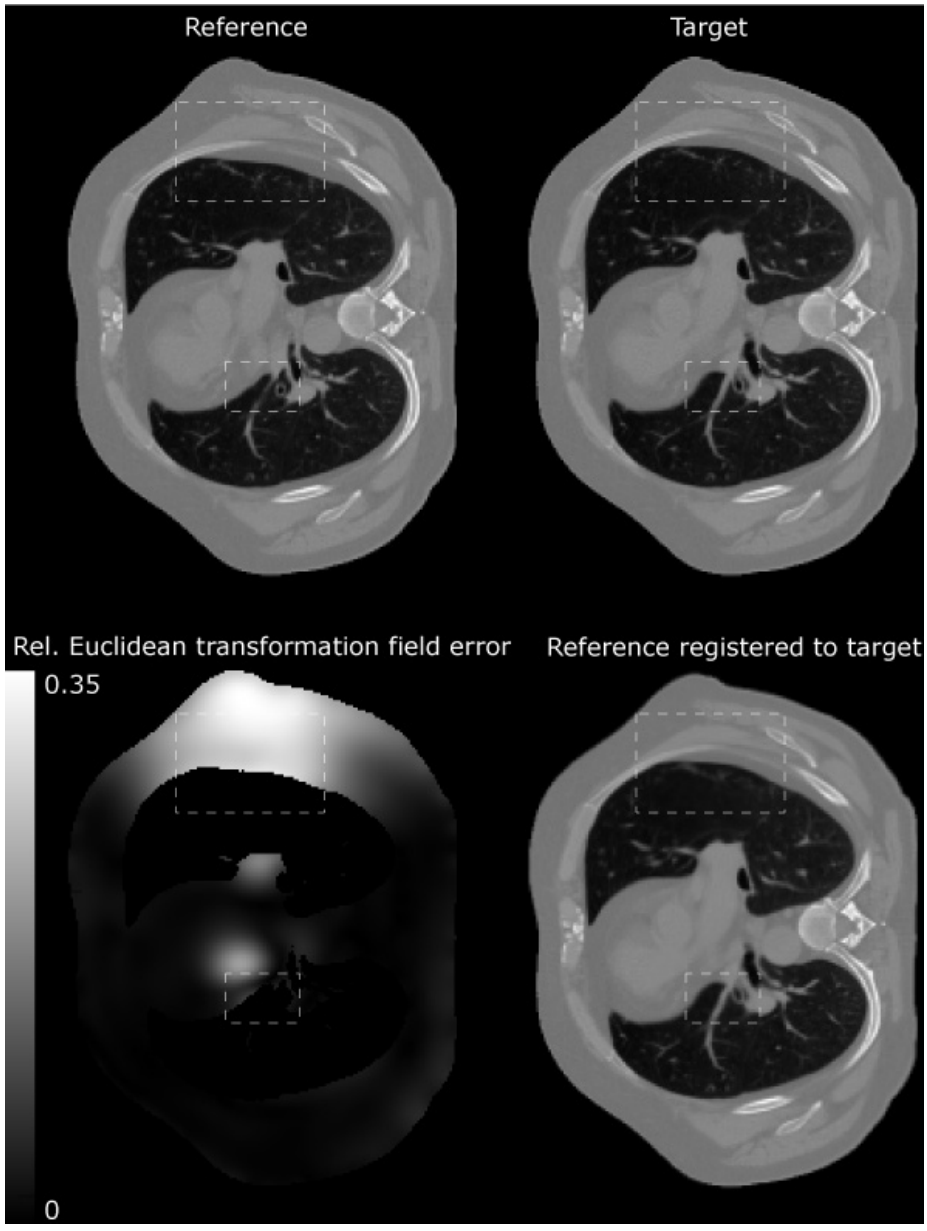
Reference
Target
Rel. Euclidean transformation field error
0.35
0
Reference registered to target

Figure 8.1

Chapter 9

Three-dimensional MRI-linac intra-fraction guidance using multiple orthogonal cine-MRI planes

T. Bjerre, S. Crijns, P. Munck af Rosenschöld, M. Aznar, L. Specht, R. Larsen and P. Keall. 'Three-dimensional MRI-linac intra-fraction guidance using multiple orthogonal cine-MRI planes'. In: *Physics in medicine and biology*, 58.14 (2013), pp. 4943-4950.

Abstract

Introduction: The introduction of integrated MRI-radiation therapy systems will offer live intra-fraction imaging. We propose a feasible low-latency multi-plane MRI-linac guidance strategy. In this work we demonstrate how interleaved acquired, orthogonal cine-MRI planes can be used for low-latency tracking of the 3D trajectory of a soft-tissue target structure. **Methods:** The proposed strategy relies on acquiring a pre-treatment 3D breath-hold scan, extracting a

3D target template and performing template matching between this 3D template and pairs of orthogonal 2D cine-MRI planes intersecting the target motion path. **Results:** For a 60 second free-breathing series of orthogonal cine-MRI planes, we demonstrate that the method was capable of accurately tracking the respiration related 3D motion of the left kidney. Quantitative evaluation of the method using a dataset designed for this purpose revealed a translational error of 1.15 mm for a translation of 39.9 mm. **Conclusions:** We have demonstrated how interleaved acquired, orthogonal cine-MRI planes can be used for online tracking of soft tissue target volumes.

Online supplementary data available from `http://stacks.iop.org/PMB/58/4943/mmedia`

9.1 Introduction

Integrated MRI-radiotherapy systems are currently under development, as described by Lagendijk et al. 2008, Raaymakers et al. 2009, Fallone et al. 2009, Dempsey et al. 2011, Dempsey et al. 2005. While not widely available, such systems offer live intra-fraction imaging, thus facilitating non-invasive, non-surrogate based, low-latency tumor motion tracking with no additional imaging radiation dose. Online tracking of target volumes in image-guided radiotherapy (IGRT) has great potential to increase conformality when treating tumors affected by respiratory motion. Tumor dose is thereby maximized while the dose to surrounding healthy tissue is minimized, Verellen et al. 2007. This enables dose escalation, providing for a higher tumor control probability.

The AAPM Task Group 76 report by Keall et al. 2006 concluded that lung tumors can follow complex 3D trajectories. An intra-fraction tracking method should therefore preferably provide 3D coordinates of the tumor. Possible breathing irregularities necessitate that the latency of an online tracking system be kept as low as possible. Keall et al. 2006 suggest that an upper latency limit for an online tracking system should be 0.5 seconds. Ries et al. 2010 show that an MRI tracking system with a 10 Hz imaging rate, 100 ms processing latency and a Kalman predictor provides a 0.9 mm tracking error for tracking the motion of a kidney. Such tracking error will be close to the voxel size delivered by most MRI systems.

Acquisition of high-quality live 3D images with subsequent low-latency deformable image registration (DIR) would be optimal, but is currently not feasible due to the lack of appropriate MRI acquisition sequences and DIR algorithms.

Previous efforts have focused on tracking in 2D cine-MRI planes. Cerviño et al. 2011 suggested the use of template matching for real-time lung tumor tracking in sagittal cine-MRI scans. An inherent drawback of tracking a 3D structure in a 2D plane is the inability to detect out-of-plane motion. They suggest addressing out-of-plane motion by surrogate tracking of the diaphragm. Yun et al. 2012b investigated the use of an intra-fractional lung tumor auto-contouring algorithm for a phantom study using sagittal cine-MRI planes. Yun et al. 2012a describes how the auto-contouring algorithm of Yun et al. 2012b can be extended with an artificial neural network (ANN)-based motion prediction algorithm.

Ries et al. 2010 performed 3D target tracking by combining 2D-plane imaging with prospective slice tracking based on pencil-beam navigator sequences. The effect of the update latency was reduced using a Kalman-predictor for trajectory anticipation. One limitation they find is that since the detected beam signal is predominantly spin-density weighted, it suffers from poor tissue contrast, which can potentially lead to poor tracking performance.

We have developed and investigated a 3D tracking strategy feasible for low-latency, intra-fraction magnetic resonance imaging-linear accelerator (MRI-linac) guidance. The proposed strategy is based on template matching between a 3D target template obtained from a pre-treatment breath-hold MRI scan and sets of orthogonal cine-MRI planes. We use interleaved acquired coronal and sagittal cine-MRI scan planes, intersecting the motion path of the tracked structure in the subject.

We seek to illustrate that the method facilitates 3D motion tracking, that the use of orthogonal planes is superior to tracking 2D target templates on a single cine-MRI plane, and that the method is feasible for online tracking of soft tissue target volumes.

9.2 Methods

The clinical scenario under which this method would operate involves the acquisition of a pre-treatment breath-hold 3D MRI scan from which a 3D template containing the target is extracted.

The similarity between the 3D template and pairs of cine-MRI 2D coronal and sagittal planes is calculated for each combination of investigated [posterior-anterior (PA), right-left (RL), inferior-superior (IS)] translations of the 3D template. If the resolution of the 3D template differs from the resolution of the 2D planes, interpolation is required.

The 3D bounding box, V_{C}, with dimensions $N_{\mathrm{PA}} \times N_{\mathrm{RL}} \times N_{\mathrm{IS}}$ encompasses the entire irregularly shaped target volume V_T.

The 3D target template can be thought of as a set of 2D coronal target slices as well as a set of sagittal target slices encompassing the segmented target

$$S_{\mathrm{cor}} = \{s_{\mathrm{cor},1}, .., s_{\mathrm{cor},N_{\mathrm{PA}}}\}, \tag{9.1}$$
$$S_{\mathrm{sag}} = \{s_{\mathrm{sag},1}, .., s_{\mathrm{sag},N_{\mathrm{RL}}}\}, \tag{9.2}$$

where each slice spans the target volume in that particular orientation and plane, e.g.

$$s_{\mathrm{cor},1} = V_C(1, i_{\mathrm{RL}}, i_{\mathrm{IS}}) \tag{9.3}$$
$$i_{RL} = [\min_{\mathrm{RL}} - b, .., \max_{\mathrm{RL}} + b] \tag{9.4}$$
$$i_{IS} = [\min_{\mathrm{IS}} - b, .., \max_{\mathrm{IS}} + b)], \tag{9.5}$$

where $\min_{\mathrm{RL}}, \max_{\mathrm{RL}}, \min_{\mathrm{IS}}, \max_{\mathrm{IS}}$ are the minimum and maximum voxel indices of segmented target volume voxels in that particular slice. This means that the set of target slices in one orientation are not necessarily of the same dimension. Here, b is an additional border that can be added to improve tracking robustness if necessary. On the other hand, adding too wide a border might deteriorate accuracy.

For each set of interleaved acquired coronal and sagittal 2D cine-MRI planes, $P_{\mathrm{cor}}, P_{\mathrm{sag}}$, a similarity measure is evaluated between P_{cor} and the individual slices of the coronal target slice set S_{cor} and between P_{sag} and the slices of S_{sag}. The similarity measure is evaluated for all investigated combinations of PA, RL and IS translations of the target template, with $T_{\mathrm{PA}}, T_{\mathrm{RL}}, T_{\mathrm{IS}}$ being the total number of investigated translations in each direction. This results in T_{PA} 2D coronal similarity arrays d_{cor} of size $T_{\mathrm{RL}} \times T_{\mathrm{IS}}$ and T_{RL} 2D sagittal similarity arrays d_{sag} of size $T_{\mathrm{PA}} \times T_{\mathrm{IS}}$. The arrays are normalized by subtracting each array by the lowest of the array itself.

The coronal and sagittal 2D similarity arrays are coalesced into two 3D similarity arrays, $D_{\mathrm{cor}}, D_{\mathrm{sag}}$ both of size $T_{\mathrm{PA}} \times T_{\mathrm{RL}} \times T_{\mathrm{IS}}$. Subsequently, the combined similarity array, D_{total}, is determined by adding the normalized coronal and sagittal similarity arrays,

$$D_{\mathrm{total}} = D_{\mathrm{cor,normalized}} + D_{\mathrm{sag,normalized}}. \tag{9.6}$$

The optimal translation is the one with the highest combined similarity measure,

$$\max_t(D_{\mathrm{total}}) \Rightarrow t_{\mathrm{optimal}}. \tag{9.7}$$

The normalization is performed in order for the similarity values of the coronal and sagittal array to be approximately on the same scale. If not normalized, one

array might dominate D_{total}. If the orthogonal slices have different resolutions, further normalization might be needed.

As similarity measure for the template matching we applied mean-absolute-difference (MAD). Other methods, including mean-squared-error (MSE) and normalized cross-correlation (NCC) were considered, but generally gave inferior results for the data at hand. Note that MAD and MSE are actually dissimilarity measures for which equation 9.6 is minimized in order to maximize similarity.

Breath-hold scans and cine-MRI scans were acquired using the same sequence so that normalization was not required. In order to apply traditional template matching algorithms, the template was interpolated to the same pixel size as the orthogonal planes.

A basic assumption for this method is local rigidity of the target volume. The method should be suitable for target sites where this approximately holds. We acquired coronal and sagittal planes, but all directions could be used, as long as the tracked structure is intersected by the orthogonal planes at all times. If the target volume is too small to ensure this, additional border can be added to the target template as described above.

9.2.1 Qualitative evaluation

For a qualitative evaluation of the method, we acquired a 3D exhale MRI scan and a series of interleaved acquired orthogonal cine-MRI planes. We segmented the 3D target structure from the exhale scan by manual delineation, and then performed tracking on all pairs of cine planes in a one-minute sequence, thus estimating the position of the target center in 3D. Since the true position of the target volume center in 3D cannot be known during this type of acquisition, the result is evaluated using visual inspection, by superimposing the target volume delineation on the cine-MRI scans according to the estimated translation of the volume.

The true position can only be known for acquisition of 3D volumes with no motion, ie. during breath-hold or using very fast sequences with inherently poor signal-to-noise ratio.

9.2.2 Quantitative evaluation

In order to quantify the accuracy of the method, we acquired 3D inhale and exhale breath-hold MRI scans and segmented the target structure in both breathing phases by manual delineation. This gives us the true difference in position of the target structure in these two breath-hold states. We then compared the true difference in location of the center of the target volume to the one approximated using tracking of the 3D target template from the exhale scan on a sagittal and coronal slice pair, extracted from the 3D inhale breath-hold scan. This approach simulates tracking on cine-MRI planes while knowing the actual true position of the target center of volume.

The true difference in location of the target center of volume is established by delineating the 3D target volume in the 3D inhale and exhale scans, calculating the center of the target volume and calculating the posterior-anterior, right-left and inferior-superior differences in location.

We compared our multi-plane 3D tracking method to 2D tracking as demonstrated by Cerviño et al. 2011. This was done by using the segmented target on one sagittal or coronal slice in the exhale scan as template and tracking this template in the same coronal or sagittal slice plane of the inhale scan.

9.2.3 Data for qualitative evaluation

This method is applicable to all tumor sites affected by respiratory motion. We tested the method in a healthy subject, tracking the left kidney during respiration.

All data was acquired on a 1.5T Philips Achieva system using an 8 channel torso receive coil.

The orthogonal cine-MRI planes were interleaved acquired during free breathing using a balanced steady-state free precession (bSSFP) sequence with the following parameters TR/TE = 2.7/1.34 ms, FOV = 40×40 cm, flip angle = $35°$, slice thickness = 7 mm, in-plane voxel size = 1.05 mm, parallel imaging factor 2, acquisition time per plane = 0.252 s.

At the intersection between the orthogonal planes, less signal is received which results in a dark line. This is compensated for prior to the template matching, by multiplying each line of the cine-MRI plane by $1 + 0.4 * G$, where $G = \exp(-0.5 \cdot \frac{x-c}{w})$ is a (non-normalized) 1D Gaussian kernel with a kernel width of

3 pixel widths and center c at the intersection between the orthogonal planes. The optimal kernel width has been chosen by visual inspection. This is an ad hoc empirical solution.

A 3D exhale breath-hold scan was acquired using a bSSFP sequence similar to the one used for the cine-MRI planes using the following parameters TR/TE = 2.7/1.34 ms, FOV = $12 \times 31 \times 31$ cm (PA, LR, IS), flip angle = 35°, slice thickness = 2 mm, in-plane voxel size = 1.1 mm, acquisition time = 25 s.

The target structure, the left kidney, was manually contoured using the Varian Eclipse software (Varian Medical Systems Inc.). For a clinical implementation, target auto-segmentation could be employed. Using MATLAB for further pre-processing, the 3D scan was interpolated to the same resolution as the orthogonal cine-MRI planes, and filtered with a Gaussian kernel for improving tracking robustness. By applying this low pass filtering operation we sought to ensure that the algorithm reach a global similarity maximum and not a local one by enhancing the dominant features of the template.

9.2.4 Data for quantitative evaluation

3D exhale and inhale breath-hold scans were acquired using the same 3D sequence as for the qualitative evaluation data. The target structure, the left kidney, was manually contoured in both scans and pre-processed in the same manner as the scan for qualitative evaluation.

9.3 Results

9.3.1 Qualitative evaluation

Fig. 9.1 displays the measured translation of the left kidney during a one-minute interleaved acquisition sequence of coronal and sagittal cine-MRI planes. The initial use of no additional voxel border on the sets of target slices resulted in a few deviations (discontinuities of center of volume trajectory). By using a border width of 3 voxels these few deviations were avoided due to added robustness. By visual inspection, tracking accuracy on the remaining frames did not seem deteriorated by the use of the border. Correlation between the time-series of inferior-superior and posterior-anterior translation was -0.83. Correlation between inferior-superior and right-left translation was 0.83. The maximum

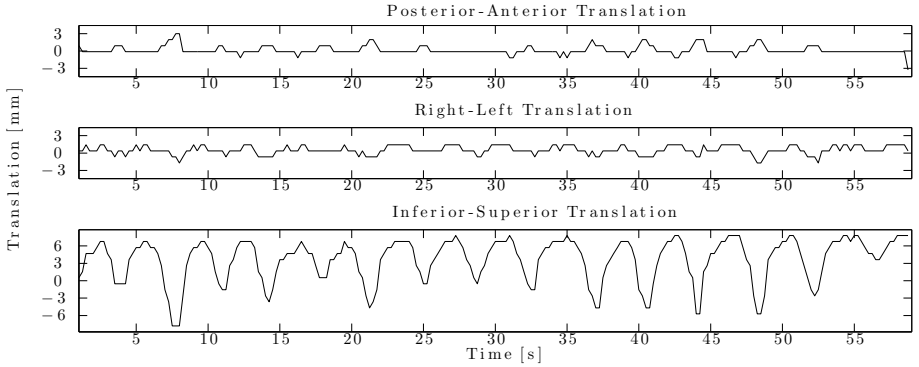

Figure 9.1: This figure displays posterior-anterior, right-left and inferior-superior translation of the left kidney as a function of time during free breathing. In the plot of inferior-superior position the peaks represent exhalation while the troughs represent inhalation. The translation was determined using the multi-plane guidance method for pairs of interleaved acquired coronal and sagittal cine-MRI planes. Acquisition frequency was 4 Hz.

peak-to-peak translations in [PA, LR, IS] directions were $[4.2, 3.2, 16]$ mm respectively. The standard deviation of target position in [PA, LR, IS] directions were $[0.70, 0.75, 3.8]$ mm respectively.

Fig. 9.2 displays two pairs of coronal and sagittal cine-MRI planes from the sequence. The 3D kidney delineation from the exhale breath-hold scan is superimposed on the cine-MRI planes, according to the translation providing maximum similarity, using our multi-plane 3D tracking method.

See supplementary material for a video that shows all orthogonal cine-MRI pairs of the acquired one-minute sequence with superimposed delineation.

The mean processing time for a slice pair was 153 ms for a $53 \times 83 \times 111$ voxel template with a non-parallelized Matlab implementation on an Intel I7-620M processor.

9.3.2 Quantitative evaluation

Table 9.1 presents the results of the quantitative evaluation. The table compares the difference in accuracy between 3D tracking on orthogonal cine-MRI planes

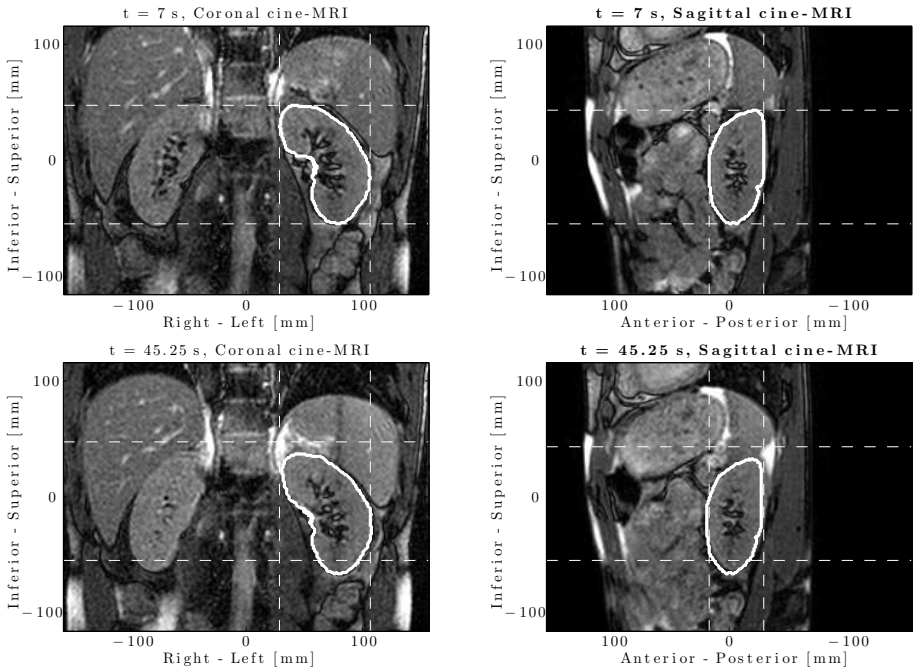

Figure 9.2: For two points in time during free breathing, $t = [7, 45.25]$ seconds, this figure displays pairs of interleaved acquired coronal and sagittal cine-MRI planes. The 3D kidney delineation from the exhale breath-hold scan is superimposed on the cine-MRI planes (solid white), according to translation determined using our multi-plane 3D tracking method. The dotted white lines are at the same positions in the scans and are included only to emphasize the soft tissue motion between the time points.

	True difference in location [mm]	Appr. difference [mm]			Error [mm]		
		S	C	S+C	S	C	S+C
Posterior-Anterior	10.5	9.38	0	9.38	1.09	10.5	1.09
Right-Left	-3.46	0	-6.25	-3.13	-3.46	2.79	-0.34
Inferior-Superior	-38.3	-38.5	-38.5	-38.5	0.20	0.20	0.20
Total (Euclidean)	39.9	39.7	39.0	39.8	3.63	10.8	1.15

Table 9.1: This table compares the true difference in location of the center of volume of the left kidney between 3D inhale and exhale breath-hold MRI scans with the approximated difference in location. The difference is approximated using 3D tracking of the 3D kidney template from the exhale scan on a sagittal and coronal slice pair from the inhale scan, emulating cine-MRI planes (denoted by S+C) as well as by using 2D tracking of single sagittal or coronal slice kidney templates from the exhale scan tracked on the same sagittal or coronal slice of the inhale scan (denoted S and C respectively). The calculated error is the Euclidean difference between the true and estimated position.

and 2D tracking on a single sagittal or coronal plane.

The use of different border widths around the delineated area in the slices of the 3D template was investigated. The use of no border gave the most accurate result.

9.4 Discussion & Conclusions

We have developed a low-latency MRI-linac guidance strategy, feasible for intra-fraction image-guidance during radiotherapy. Obtaining low-latency information about the 3D target trajectory is the single most important feature of our multi-plane tracking method.

Intra-fraction image guidance allows for improved conformality and maximization of the therapeutic ratio by increasing dose to target tissues and decreasing dose to healthy tissue. We have shown that by using orthogonal, interleaved acquired cine-MRI planes it is possible to track the 3D trajectory of a soft tissue target structure. From visual inspection, tracking of the kidney in the one-minute cine-MRI sequence appears very accurate and robust.

It is interesting but not surprising that there was a relatively large correlation between motion in the 3 dimensions. However, based on the translations in

Fig. 1, it is not possibly to predict the P-A and L-R translations from the I-S translation alone.

The quantitative evaluation results indicate errors of total 3D motion on the scale of the width of a cine-MRI pixel (1.04 mm). The use of orthogonal planes was superior to using only a sagittal or coronal plane. Investigations using 3D breath-hold scans at different inhalation states or 4D MRI could be used to further validate these results. This is merely the overall translational error, assuming local rigidity, and does not reflect on any delineation uncertainty or deformation between the phases, nor the uncertainty related to the breath-hold acquisition.

It is noteworthy that any number and orientation of intersecting live planes could be used, as long as the target is intersected by the planes at all times. Further investigation on a variety of patient cases and target sizes/locations will be needed to more broadly characterize the performance of this guidance strategy.

The use of two orthogonal cine-MRI planes inherently increases the time between two successive scans of the same plane. In cases with linear trajectory of the target volume it would be possible to avoid the out-of-plane motion when using a single cine-MRI plane by choosing an appropriate orientation. In these cases, using a single cine-MRI plane could be superior to using the proposed multi-plane method due to the higher temporal resolution.

The processing time for the current implementation allows the total system delay to be below the 0.5 seconds prescribed by Keall et al. 2006, thus allowing the method to be fast enough for online tracking. It should be straightforward to implement parallel processing for a further reduction of processing time. Parallel processing could also facilitate rotation-invariant template matching by processing 3D templates with different rotation. For further robustness, and in order to prevent any eventual deviations, the described method could be extended with a prediction algorithm. The adoption of a scale-space strategy might be appropriate for improving tracking robustness and further reduce processing time, see e.g. Witkin 1984.

While this work focuses on MRI-linac guidance, the described method is relevant for other applications as well, including MRI high-intensity focused ultrasound (HIFU) systems.

References

[1] J. R. Adler Jr, M. J. Murphy, S. D. Chang and S. L. Hancock. 'Image-guided robotic radiosurgery'. In: *Neurosurgery* 44.6 (1999), pp. 1299–1306.

[2] J. R. Adler Jr, S. D. Chang, M. J. Murphy, J Doty, P Geis and S. L. Hancock. 'The Cyberknife: a frameless robotic system for radiosurgery'. In: *Stereotactic and functional neurosurgery* 69.1-4 (1997), pp. 124–128.

[3] E. E. Ahunbay, C. Peng, A. Godley, C. Schultz and X. A. Li. 'An on-line replanning method for head and neck adaptive radiotherapy'. In: *Medical Physics* 36.10 (2009), p. 4776.

[4] E. E. Ahunbay, C. Peng, G.-P. Chen, S. Narayanan, C. Yu, C. Lawton and X. A. Li. 'An on-line replanning scheme for interfractional variations'. In: *Medical Physics* 35.8 (2008), p. 3607.

[5] V. Arsigny, X. Pennec and N. Ayache. 'Polyrigid and polyaffine transformations: A new class of diffeomorphisms for locally rigid or affine registration'. In: *Medical Image Computing and Computer-Assisted Intervention - MICCAI* (2003), pp. 829–837.

[6] M. C. Aznar, G. F. Persson, I. M. Kofoed, D. E. Nygaard and S. S. Korreman. 'Irregular breathing during 4DCT scanning of lung cancer patients: Is the midventilation approach robust?' In: *Physica Medica* (2013).

[7] J. L. Barker, A. S. Garden, K. K. Ang, J. C. O'Daniel, H. Wang, L. E. Court, W. H. Morrison, D. I. Rosenthal, K. S. C. Chao, S. L. Tucker, R. Mohan and L. Dong. 'Quantification of volumetric and geometric changes occurring during fractionated radiotherapy for head-and-neck cancer using an integrated CT/linear accelerator system'. In: *International Journal of Radiation Oncologyâ€¢ Biologyâ€¢ Physics* 59.4 (July 2004), pp. 960–970.

[8] A Bel, M. V. Herk, H Bartelink and J. Lebesque. 'A verification procedure to improve patient set-up accuracy using portal images'. In: *Radiotherapy and Oncology* 29 (1993), pp. 253–260.

[9] J. Beutel, H. L. Kundel and R. L. Van Metter. 'Handbook of Medical Imaging, volume 1: Physics and Psychophysics'. In: (2000).

[10] T Beyer, D. W. Townsend, T Brun, P. E. Kinahan, M Charron, R Roddy, J Jerin, J Young, L Byars and R Nutt. 'A combined PET/CT scanner for clinical oncology.' In: *Journal of nuclear medicine : official publication, Society of Nuclear Medicine* 41.8 (Aug. 2000), pp. 1369–79.

[11] T. Bjerre, M. O. Fogtmann, M. Aznar, P Munck af Rosenschold, L. Specht and R. Larsen. 'Spatially varying Riemannian elasticity regularization: Application to thoracic CT registration in image-guided radiotherapy'. In: *Biomedical Imaging (ISBI), 2012 9th IEEE International Symposium on*. IEEE, 2012, pp. 1224–1227.

[12] D. Boehmer, P. Maingon, P. Poortmans, M.-H. Baron, R. Miralbell, V. Remouchamps, C. Scrase, A. Bossi and M. Bolla. 'Guidelines for primary radiotherapy of patients with prostate cancer'. In: *Radiotherapy and oncology* 79.3 (2006), pp. 259–269.

[13] H. C. de Boer and B. J. Heijmen. 'A protocol for the reduction of systematic patient setup errors with minimal portal imaging workload.' In: *International journal of radiation oncology, biology, physics* 50.5 (Aug. 2001), pp. 1350–65.

[14] T. Bortfeld, S. B. Jiang and E. Rietzel. 'Effects of motion on the total dose distribution'. In: *Seminars in radiation oncology*. Vol. 14. 1. Elsevier, 2004, pp. 41–51.

[15] T. S. Bray, A. Kaczynski, K. Albuquerque, F. Cozzi and J. C. Roeske. 'Role of image guided radiation therapy in obese patients with gynecologic malignancies'. In: *Practical Radiation Oncology* (2012).

[16] C. Broit. 'Optimal registration of deformed images'. PhD thesis. University of Pennsylvania, 1981.

[17] R. Brooks and M. Keller. 'Progress toward quantitative computed tomography'. In: *IEEE Transactions on Nuclear Science* 27.3 (1980), pp. 1121–1127.

[18] N. Burridge, A. Amer, T. Marchant, J. Sykes, J. Stratford, A. Henry, C. McBain, P. Price and C. Moore. 'Online adaptive radiotherapy of the bladder: small bowel irradiated-volume reduction'. In: *International journal of radiation oncology, biology, physics* 66.3 (Nov. 2006), pp. 892–897.

[19] L. I. Cerviño, J. Du and S. B. Jiang. 'MRI-guided tumor tracking in lung cancer radiotherapy'. In: *Phys. Med. Biol.* 56 (2011), pp. 3773–3785.

[20] X. Chai, M. van Herk, J. B. van de Kamer, P. Remeijer, A. Bex, A. Betgen, T. M. De Reijke, M. C. C. M. Hulshof, F. J. Pos and A. Bel. 'Behavior of lipiodol markers during image guided radiotherapy of bladder cancer'. In: *International Journal of Radiation Oncology* Biology* Physics* 77.1 (2010), pp. 309–314.

[21] S. D. Chang, W. Main, D. P. Martin, I. C. Gibbs and M. P. Heilbrun. 'An analysis of the accuracy of the CyberKnife: a robotic frameless stereotactic radiosurgical system'. In: *Neurosurgery* 52.1 (2003), pp. 140–147.

[22] S. Cherry, Y. Shao, K. Meadors, S. Siegel, A. Chatziioannou, J. Young, W. Jones, J. Moyers, D. Newport, T. Farquhar, M. Andreaco, M. Paulus, D. Binkley, R. Nutt and M. Phelps. 'MicroPET: a high resolution PET scanner for imaging small animals'. In: *IEEE Transactions on Nuclear Science* 44.3 (1997), pp. 1161–1166.

[23] I. J. Chetty, B. Curran, J. E. Cygler, J. J. DeMarco, G. Ezzell, B. a. Faddegon, I. Kawrakow, P. J. Keall, H. Liu, C.-M. C. Ma, D. W. O. Rogers, J. Seuntjens, D. Sheikh-Bagheri and J. V. Siebers. 'Report of the AAPM Task Group No. 105: Issues associated with clinical implementation of Monte Carlo-based photon and electron external beam treatment planning'. In: *Medical Physics* 34.12 (2007), p. 4818.

[24] H. Choi, C. Charnsangavej, S. de Castro Faria, E. P. Tamm, R. S. Benjamin, M. M. Johnson, H. A. Macapinlac and D. A. Podoloff. 'CT evaluation of the response of gastrointestinal stromal tumors after imatinib mesylate treatment: a quantitative analysis correlated with FDG PET findings'. In: *American Journal of Roentgenology* 183.6 (2004), pp. 1619–1628.

[25] S Clippe, D Sarrut, C Malet, S Miguet, C Ginestet and C Carrie. 'Patient setup error measurement using 3D intensity-based image registration techniques'. In: *International Journal of Radiation OncologyBiologyPhysics* 56.1 (May 2003), pp. 259–265.

[26] a. M. Cormack. 'Representation of a Function by Its Line Integrals, with Some Radiological Applications'. In: *Journal of Applied Physics* 34.9 (1963), p. 2722.

[27] S. P. M. Crijns, B. W. Raaymakers and J. J. W. Lagendijk. 'Proof of concept of MRI-guided tracked radiation delivery: tracking one-dimensional motion'. In: *Physics in medicine and biology* 57.23 (2012), p. 7863.

[28] S. P. M. Crijns, J. G. M. Kok, J. J. W. Lagendijk and B. W. Raaymakers. 'Towards MRI-guided linear accelerator control: gating on an MRI accelerator'. In: *Physics in medicine and biology* 56.15 (2011), p. 4815.

[29] S. Crijns. 'On-line MRI guidance for Radiotherapy'. PhD Thesis. University Medical Center Utrecht, 2013.

[30] W. D. D'Souza, S. A. Naqvi and X. Y. Cedric. 'Real-time intra-fraction-motion tracking using the treatment couch: a feasibility study'. In: *Physics in medicine and biology* 50.17 (2005), p. 4021.

[31] J.-F. Daisne, T. Duprez, B. Weynand, M. Lonneux, M. Hamoir, H. Reychler and V. Grégoire. 'Tumor Volume in Pharyngolaryngeal Squamous Cell Carcinoma: Comparison at CT, MR Imaging, and FDG PET and Validation with Surgical Specimen1'. In: *Radiology* 233.1 (2004), pp. 93–100.

[32] R Damadian, M Goldsmith and L Minkoff. 'NMR in cancer: XVI. FONAR image of the live human body.' In: *Physiological chemistry and physics* 9.1 (1976), pp. 97–100.

[33] R. Damadian. 'Tumor detection by nuclear magnetic resonance'. In: *Science* 171.3976 (1971), pp. 1151–1153.

[34] B. Delhay, P. Clarysse and I. Magnin. 'Locally adapted spatio-temporal deformation model for dense motion estimation in periodic cardiac image sequences'. In: *Functional Imaging and Modeling of the Heart* (2007), pp. 393–402.

[35] J. Dempsey, D. Benoit, J. Fitzsimmons, A. Haghighat, J. Li, D. Low, S. Mutic, J. Palta, H. Romeijn and G. Sjoden. 'A device for realtime 3D image-guided IMRT'. In: *International Journal of Radiation Oncology Biology Physics* 63 (2005), pp. 202–202.

[36] J. Dempsey and 'VIEWRAY Inc.'. *System and Method for Image Guidance During Medical Procedures*. 2011.

[37] G. X. Ding, D. M. Duggan, C. W. Coffey, M. Deeley, D. E. Hallahan, A. Cmelak and A. Malcolm. 'A study on adaptive IMRT treatment planning using kV cone-beam CT.' In: *Radiotherapy and oncology : journal of the European Society for Therapeutic Radiology and Oncology* 85.1 (Oct. 2007), pp. 116–25.

[38] P. Dirix, V. Vandecaveye, F. De Keyzer, S. Stroobants, R. Hermans and S. Nuyts. 'Dose painting in radiotherapy for head and neck squamous cell carcinoma: value of repeated functional imaging with (18)F-FDG PET, (18)F-fluoromisonidazole PET, diffusion-weighted MRI, and dynamic contrast-enhanced MRI.' In: *Journal of nuclear medicine : official publication, Society of Nuclear Medicine* 50.7 (July 2009), pp. 1020–7.

[39] S. Erridge, Y. Seppenwoolde, S. Muller, M. van Herk, K. De Jaeger, J. Belderbos, L. Boersma and J. Lebesque. 'Portal imaging to assess set-up errors, tumor motion and tumor shrinkage during conformal radiotherapy of non-small cell lung cancer'. In: *Radiotherapy and oncology* 66.1 (2003), pp. 75–85.

[40] S. Faivre, M. Zappa, V. Vilgrain, E. Boucher, J.-Y. Douillard, H. Y. Lim, J. S. Kim, S.-A. Im, Y.-K. Kang and M. Bouattour. 'Changes in tumor density in patients with advanced hepatocellular carcinoma treated with sunitinib'. In: *Clinical Cancer Research* 17.13 (2011), pp. 4504–4512.

[41] B. G. Fallone, B. Murray, S. Rathee, T. Stanescu, S. Steciw, S. Vidakovic, E. Blosser and D. Tymofichuk. 'First MR images obtained during megavoltage photon irradiation from a prototype integrated linac-MR system'. In: *Medical Physics* 36.6 (2009), p. 2084.

[42] M. Feng, J. M. Balter, D. Normolle, S. Adusumilli, Y. Cao, T. L. Chenevert and E. Ben-Josef. 'Characterization of pancreatic tumor motion using cine MRI: surrogates for tumor position should be used with caution'. In: *International Journal of Radiation Oncology* Biology* Physics* 74.3 (2009), pp. 884–891.

[43] Y. Feng, C. Castro-Pareja, R. Shekhar and C. Yu. 'Direct aperture deformation: An interfraction image guidance strategy'. In: *Medical Physics* 33.12 (2006), p. 4490.

[44] L. Fokdal, H. Honoré, M. Høyer, P. Meldgaard, K. Fode and H. von der Maase. 'Impact of changes in bladder and rectal filling volume on organ motion and dose distribution of the bladder in radiotherapy for urinary bladder cancer'. In: *International Journal of Radiation Oncology* Biology* Physics* 59.2 (2004), pp. 436–444.

[45] M. Fornefett, K. Rohr and H. Stiehl. 'Radial basis functions with compact support for elastic registration of medical images'. In: *Image and Vision Computing* 19.1-2 (Jan. 2001), pp. 87–96.

[46] T. Fox, E. L. Simon, E. Elder, R. H. Riffenburgh and P. A. S. Johnstone. 'Free breathing gated delivery (FBGD) of lung radiation therapy: Analysis of factors affecting clinical patient throughput'. In: *Lung cancer* 56.1 (2007), pp. 69–75.

[47] T. Girinsky, R. van der Maazen, L. Specht, B. Aleman, P. Poortmans, Y. Lievens, P. Meijnders, M. Ghalibafian, J. Meerwaldt and E. Noordijk. 'Involved-node radiotherapy (INRT) in patients with early Hodgkin lymphoma: concepts and guidelines'. In: *Radiotherapy and oncology* 79.3 (2006), pp. 270–277.

[48] B. Glocker, A. Sotiras, N. Komodakis and N. Paragios. 'Deformable Medical Image Registration : Setting the State of the Art with Discrete Methods â^—'. In: *Annual Review of Biomedical Engineering* 13 (2011), pp. 219–244.

[49] V Grégoire and T. R. Mackie. 'State of the art on dose prescription, reporting and recording in Intensity-Modulated Radiation Therapy (ICRU report No. 83).' In: *Cancer radiothérapie : journal de la Société française de radiothérapie oncologique* 15.6-7 (Oct. 2011), pp. 555–9.

[50] V. Grégoire, E. Coche, G. Cosnard, M. Hamoir and H. Reychler. 'Selection and delineation of lymph node target volumes in head and neck conformal radiotherapy. Proposal for standardizing terminology and procedure based on the surgical experience'. In: *Radiotherapy and Oncology* 56.2 (2000), pp. 135–150.

[51] B. A. Groh, J. H. Siewerdsen, D. G. Drake, J. W. Wong and D. A. Jaffray. 'A performance comparison of flat-panel imager-based MV and kV cone-beam CT'. In: *Medical physics* 29 (2002), p. 967.

[52] J. Hajnal, D. Hill and D. Hawkes, eds. *Medical image registration*. 2010.

[53] E. C. Halperin, C. A. Perez and L. W. Brady. *Perez and Bradyâ€™s principles and practice of radiation oncology*. 5th ed. Lippincott William's and Wilkins, 2008.

[54] E. K. Hansen, M. K. Bucci, J. M. Quivey, V. Weinberg and P. Xia. 'Repeat CT imaging and replanning during the course of IMRT for head-and-neck cancer.' In: *International journal of radiation oncology, biology, physics* 64.2 (Feb. 2006), pp. 355–62.

[55] M. F. Hansen. 'The Virtual Knife'. PhD thesis. Technical University of Denmark, 2009.

[56] M. van Herk. 'Errors and margins in radiotherapy.' In: *Seminars in radiation oncology* 14.1 (Jan. 2004), pp. 52–64.

[57] M. Hofmann, B. Pichler, B. Schölkopf and T. Beyer. 'Towards quantitative PET/MRI: a review of MR-based attenuation correction techniques'. In: *European journal of nuclear medicine and molecular imaging* 36.1 (2009), pp. 93–104.

[58] C. Hollensen. 'Planning and Evaluation of Radio-Therapeutic Treatment of Head-and-Neck Cancer Using PET/CT scanning'. PhD Thesis. Technical University of Denmark, 2012.

[59] B. K. P. Horn and B. G. Schunck. 'Determining optical flow'. In: *Artificial intelligence* 17.1 (1981), pp. 185–203.

[60] G. Hounsfield. 'Computerized transverse axial scanning (tomography): Part 1. Description of system'. In: *British Journal of Radiology* (1973).

[61] G. Hounsfield. *Method and apparatus for measuring X-or Y-radiation absorption or transmission at plural angles and analyzing the data.* 1972.

[62] J. Hsieh, R. C. Molthen, C. A. Dawson and R. H. Johnson. 'An iterative approach to the beam hardening correction in cone beam CT'. In: *Medical physics* 27 (2000), p. 23.

[63] T. Hu. 'Reality-based soft tissue probing: experiments and computational model for application to minimally invasive surgery'. PhD thesis. Drexel University, 2006.

[64] S. Hughes, J. McClelland, A. Chandler, M. Adams, J. Boutland, D. Withers, S. Ahmad, J. Blackall, S. Tarte, D. Hawkes and D. Landau. 'A comparison of internal target volume definition by limited four-dimensional computed tomography, the addition of patient-specific margins, or the addition of generic margins when planning radical radiotherapy for lymph node-positive non-small cell lung'. In: *Clinical Oncology* 20.4 (2008), pp. 293–300.

[65] G. D. Hugo, N. Agazaryan and T. D. Solberg. 'The effects of tumor motion on planning and delivery of respiratory-gated IMRT'. In: *Medical physics* 30 (2003), p. 1052.

[66] C. Hurkmans and P. Remeijer. 'Set-up verification using portal imaging; review of current clinical practice'. In: *Radiotherapy and Oncology* 58 (2001), pp. 105–120.

[67] C. W. Hurkmans, I. Dijckmans, M. Reijnen, J. van der Leer, C. van Vliet-Vroegindeweij and M. van der Sangen. 'Adaptive radiation therapy for breast IMRT-simultaneously integrated boost: three-year clinical experience.' In: *Radiotherapy and oncology : journal of the European Society for Therapeutic Radiology and Oncology* 103.2 (May 2012), pp. 183–7.

[68] T Ido, C. N. Wan, V Casella, J. Fowler, A. Wolf, M Reivich and D. Kuhl. 'Labeled 2-deoxy-D-glucose analogs. 18F-labeled 2-deoxy-2-fluoro-D-glucose, 2-deoxy-2-fluoro-D-mannose and 14C-2-deoxy-2-fluoro-D-glucose'. In: *Journal of Labelled Compounds and Radiopharmaceuticals* 14.2 (1978), pp. 175–183.

[69] M. K. Islam, T. G. Purdie, B. D. Norrlinger, H. Alasti, D. J. Moseley, M. B. Sharpe, J. H. Siewerdsen and D. A. Jaffray. 'Patient dose from kilovoltage cone beam computed tomography imaging in radiation therapy'. In: *Medical physics* 33 (2006), p. 1573.

[70] D. a. Jaffray, J. H. Siewerdsen, J. W. Wong and A. a. Martinez. 'Flat-panel cone-beam computed tomography for image-guided radiation therapy.' In: *International journal of radiation oncology, biology, physics* 53.5 (Aug. 2002), pp. 1337–49.

[71] A. Jemal, F. Bray, M. M. Center, J. Ferlay, E. Ward and D. Forman. 'Global cancer statistics'. In: *CA: a cancer journal for clinicians* 61.2 (2011), pp. 69–90.

[72] X. Jia, Y. Lou, R. Li, W. Y. Song and S. B. Jiang. 'GPU-based fast cone beam CT reconstruction from undersampled and noisy projection data via total variation'. In: *Medical physics* 37 (2010), p. 1757.

[73] J.-Y. Jin, F.-F. Yin, S. Tenn, P. Medin and T. Solberg. 'Use of the BrainLab ExacTrac X-ray 6D System in Image-Guided Radiotherapy'. In: *Medical dosimetry : official journal of the American Association of Medical Dosimetrists* 33.2 (Jan. 2008), pp. 124–34.

[74] S. C. Joshi and M. I. Miller. 'Landmark matching via large deformation diffeomorphisms'. In: *Image Processing, IEEE Transactions on* 9.8 (2000), pp. 1357–1370.

[75] M. S. Judenhofer, H. F. Wehrl, D. F. Newport, C. Catana, S. B. Siegel, M. Becker, A. Thielscher, M. Kneilling, M. P. Lichy and M. Eichner. 'Simultaneous PET-MRI: a new approach for functional and morphological imaging'. In: *Nature medicine* 14.4 (2008), pp. 459–465.

[76] S. Kabus, a Franz and B Fischer. 'Spatially varying elasticity in image registration.' In: *Methods of information in medicine* 46.3 (Jan. 2007), pp. 287–91.

[77] P. J. Keall, S. Joshi, S. S. Vedam, J. V. Siebers, V. R. Kini and R. Mohan. 'Four-dimensional radiotherapy planning for DMLC-based respiratory motion tracking'. In: *Medical Physics* 32.4 (2005), p. 942.

[78] P. J. Keall, G. S. Mageras, J. M. Balter, R. S. Emery, K. M. Forster, S. B. Jiang, J. M. Kapatoes, D. a. Low, M. J. Murphy, B. R. Murray, C. R. Ramsey, M. B. Van Herk, S. S. Vedam, J. W. Wong and E. Yorke. 'The management of respiratory motion in radiation oncology report of AAPM Task Group 76'. In: *Medical Physics* 33.10 (2006), p. 3874.

[79] K. Kitamura, H. Shirato, Y. Seppenwoolde, T. Shimizu, Y. Kodama, H. Endo, R. Onimaru, M. Oda, K. Fujita and S. Shimizu. 'Tumor location, cirrhosis, and surgical history contribute to tumor movement in the liver, as measured during stereotactic irradiation using a real-time tumor-tracking radiotherapy system'. In: *International Journal of Radiation Oncology* Biology* Physics* 56.1 (2003), pp. 221–228.

[80] A. Kjær, A. Loft, I. Law, A. K. Berthelsen, L. Borgwardt, J. Löfgren, C. B. Johnbeck, A. E. Hansen, S. Keller, S. Holm and L. Højgaard. 'PET/MRI in cancer patients: first experiences and vision from Copenhagen.' In: *Magma (New York, N.Y.)* 26.1 (Feb. 2013), pp. 37–47.

[81] N. Koch, H. H. Liu, G. Starkschall, M. Jacobson, K. Forster, Z. Liao, R. Komaki and C. W. Stevens. 'Evaluation of internal lung motion for respiratory-gated radiotherapy using MRI: Part Iâ€"Correlating internal lung motion with skin fiducial motion'. In: *International Journal of Radiation Oncology* Biology* Physics* 60.5 (2004), pp. 1459–1472.

[82] S. S. Korreman, T. Juhler-Nøttrup and A. L. Boyer. 'Respiratory gated beam delivery cannot facilitate margin reduction, unless combined with respiratory correlated image guidance'. In: *Radiotherapy and Oncology* 86.1 (2008), pp. 61–68.

[83] S. Korreman, G. Persson, D. Nygaard, C. Brink and T. Juhler-Nøttrup. 'Respiration-correlated image guidance is the most important radiotherapy motion management strategy for most lung cancer patients'. In: *International Journal of Radiation Oncology* Biology* Physics* 83.4 (2012), pp. 1338–1343.

[84] C. J. Kovacs, H. a. Hopkins, M. J. Evans and W. B. Looney. 'Changes in cellularity induced by radiation in a solid tumour.' In: *International journal of radiation biology and related studies in physics, chemistry, and medicine* 30.2 (Aug. 1976), pp. 101–13.

[85] J. J. W. Lagendijk, B. W. Raaymakers, A. J. E. Raaijmakers, J. Overweg, K. J. Brown, E. M. Kerkhof, R. W. van der Put, B. Hårdemark, M. van Vulpen and U. a. van der Heide. 'MRI/linac integration.' In: *Radiotherapy and oncology : journal of the European Society for Therapeutic Radiology and Oncology* 86.1 (Jan. 2008), pp. 25–9.

[86] P. C. Lauterbur. 'Image formation by induced local interactions: examples employing nuclear magnetic resonance'. In: *Nature* 242.5394 (1973), pp. 190–191.

[87] R. Li, J. H. Lewis, X. Jia, X. Gu, M. Folkerts, C. Men, W. Y. Song and S. B. Jiang. '3D tumor localization through real-time volumetric x-ray imaging for lung cancer radiotherapy'. In: *Medical Physics* 38 (2011), p. 2783.

[88] K. Lim, P. Chan, R. Dinniwell, A. Fyles, M. Haider, Y.-B. Cho, D. Jaffray, L. Manchul, W. Levin and R. P. Hill. 'Cervical cancer regression measured using weekly magnetic resonance imaging during fractionated radiotherapy: radiobiologic modeling and correlation with tumor hypoxia'. In: *International Journal of Radiation Oncology* Biology* Physics* 70.1 (2008), pp. 126–133.

[89] J. M. Links, L. S. Beach, B. Subramaniam, M. A. Rubin, J. G. Hennessey and A. L. Reiss. 'Edge complexity and partial volume effects'. In: *Journal of computer assisted tomography* 22.3 (1998), pp. 450–458.

[90] D. Liu and J. Nocedal. 'On the limited memory BFGS method for large scale optimization'. In: *Mathematical programming* 45.1 (1989), pp. 503–528.

[91] D. Loeckx, F. Maes, D. Vandermeulen and P. Suetens. 'Nonrigid image registration using free-form deformations with a local rigidity constraint'. In: *Medical Image Computing and Computer-Assisted Interventionâ€"MICCAI 2004*. Springer, 2004, pp. 639–646.

[92] Y. Long, J. a. Fessler and J. M. Balter. '3D forward and back-projection for X-ray CT using separable footprints.' In: *IEEE transactions on medical imaging* 29.11 (Nov. 2010), pp. 1839–50.

[93] W. Looney, J. Trefil, J. Schaffner, C. Kovacs and H. Hopkins. 'Solid tumor models for the assessment of different treatment modalities: 1. Radiation-induces changes in growth rate characteristics of a solid tumor model'. In: *Proceedings of the National Academy of Sciences of the United States of America* 72.7 (1975), pp. 2662–2666.

[94] D. G. Lowe. 'Distinctive image features from scale-invariant keypoints'. In: *International journal of computer vision* 60.2 (2004), pp. 91–110.

[95] M. Lyksborg, R. Paulsen, C. Brink and R. Larsen. '4D lung reconstruction with phase optimization'. In: *World Congress on Medical Physics and Biomedical Engineering, September 7-12, 2009, Munich, Germany*. Springer, 2010, pp. 2227–2230.

[96] J. T. Lyman. 'Complication probability as assessed from dose-volume histograms'. In: *Radiation Research* 104.2s (1985), S13–S19.

[97] J. T. Lyman and A. B. Wolbarst. 'Optimization of radiation therapy, III: A method of assessing complication probabilities from dose-volume histograms'. In: *International Journal of Radiation Oncology* Biology* Physics* 13.1 (1987), pp. 103–109.

[98] J. T. Lyman and A. B. Wolbarst. 'Optimization of radiation therapy, IV: A dose-volume histogram reduction algorithm'. In: *International Journal of Radiation Oncology* Biology* Physics* 17.2 (1989), pp. 433–436.

[99] F. Maes, A. Collignon, D. Vandermeulen, G. Marchal and P. Suetens. 'Multimodality image registration by maximization of mutual information'. In: *Medical Imaging, IEEE Transactions on* 16.2 (1997), pp. 187–198.

[100] P. Mansfield. 'Multi-planar image formation using NMR spin echoes'. In: *Journal of Physics C: Solid State Physics* 10.3 (1977), p. L55.

[101] N. A. Mayr, J. Z. Wang, S. S. Lo, D. Zhang, J. C. Grecula, L. Lu, J. F. Montebello, J. M. Fowler and W. T. C. Yuh. 'Translating response during therapy into ultimate treatment outcome: a personalized 4-dimensional MRI tumor volumetric regression approach in cervical cancer'. In: *International Journal of Radiation Oncology* Biology* Physics* 76.3 (2010), pp. 719–727.

[102] G. Meijer, P. V. D. Toorn and M. Bal. 'High precision bladder cancer irradiation by integrating a library planning procedure of 6 prospectively generated SIB IMRT plans with image guidance using lipiodol'. In: *Radiotherapy and Oncology* 105.2 (2012), pp. 174–179.

[103] S Midgley, R. M. Millar and J Dudson. 'A feasibility study for megavoltage cone beam CT using a commercial EPID'. In: *Physics in medicine and biology* 43.1 (1998), p. 155.

[104] R. Mohan, X. Zhang, H. Wang, Y. Kang, X. Wang, H. Liu, K. K. Ang, D. Kuban and L. Dong. 'Use of deformed intensity distributions for on-line modification of image-guided IMRT to account for interfractional anatomic changes.' In: *International journal of radiation oncology, biology, physics* 61.4 (Mar. 2005), pp. 1258–66.

[105] V. Murthy, Z. Master, P. Adurkar, I. Mallick, U. Mahantshetty, G. Bakshi, H. Tongaonkar and S. Shrivastava. ''Plan of the day' adaptive radiotherapy for bladder cancer using helical tomotherapy.' In: *Radiotherapy and oncology : journal of the European Society for Therapeutic Radiology and Oncology* 99.1 (Apr. 2011), pp. 55–60.

[106] J. Nijkamp, M. Swellengrebel, B. Hollmann, R. de Jong, C. Marijnen, C. van Vliet-Vroegindeweij, B. van Triest, M. van Herk and J.-J. Sonke. 'Repeat CT assessed CTV variation and PTV margins for short- and long-course pre-operative RT of rectal cancer.' In: *Radiotherapy and oncology : journal of the European Society for Therapeutic Radiology and Oncology* 102.3 (Mar. 2012), pp. 399–405.

[107] T. J. Nowak, A. G. Handford and G. M. Whitelegg. *Pathophysiology: concepts and applications for health care professionals.* McGraw-Hill Higher Education, 2004.

[108] D. Pace, A. Enquobahrie, H. Yang, S. Aylward and M. Niethammer. 'Deformable Image Registration of Sliding Organs Using Anisotropic Diffusive Regularization'. In: *Biomedical Imaging: From Nano to Macro, 2011 IEEE International Symposium on Biomedical Imaging*. IEEE, 2011, pp. 407–413.

[109] X Pennec, R Stefanescu, V Arsigny, P Fillard and N Ayache. 'Riemannian elasticity: a statistical regularization framework for non-linear registration.' In: *MICCAI 2005* 8.Pt 2 (Jan. 2005), pp. 943–50.

[110] M. E. Phelps, S. C. Huang, E. J. Hoffman, C Selin, L Sokoloff and D. E. Kuhl. 'Tomographic measurement of local cerebral glucose metabolic rate in humans with (F-18)2-fluoro-2-deoxy-D-glucose: validation of method'. In: *Annals of neurology* 6.5 (1979), pp. 371–388.

[111] M. Phelps and E. Hoffman. 'Application of annihilation coincidence detection to transaxial reconstruction tomography'. In: *Journal of nuclear medicine : official publication, Society of Nuclear Medicine* 16.3 (1975), pp. 210–224.

[112] B. W. Raaymakers, J. J. W. Lagendijk, J Overweg, J. G. M. Kok, a. J. E. Raaijmakers, E. M. Kerkhof, R. W. van der Put, I Meijsing, S. P. M. Crijns, F Benedosso, M van Vulpen, C. H. W. de Graaff, J Allen and K. J. Brown. 'Integrating a 1.5 T MRI scanner with a 6 MV accelerator: proof of concept.' In: *Physics in medicine and biology* 54.12 (June 2009), N229–37.

[113] N. Reynaert, S. van der Marck, D. Schaart, W. van der Zee, C. van Vliet-Vroegindeweij, M. Tomsej, J. Jansen, B. Heijmen, M. Coghe and C. de Wagter. 'Monte Carlo treatment planning for photon and electron beams'. In: *Radiation Physics and Chemistry* 76 (2007), pp. 643–686.

[114] M. Ries, B. D. de Senneville, S. Roujol, Y. Berber, B. Quesson and C. Moonen. 'Real-time 3D target tracking in MRI guided focused ultrasound ablations in moving tissues.' In: *Magnetic resonance in medicine : official journal of the Society of Magnetic Resonance in Medicine* 64.6 (Dec. 2010), pp. 1704–12.

[115] J. S. Robertson, R. B. Marr, M Rosenblum, V Radeka and Y. L. Yamamoto. '32-Crystal positron transverse section detector'. In: *Tomographic Imaging in Nuclear Medicine*. Ed. by G. Freedman. New York: The Society of Nuclear Medicine, 1972, pp. 142–153.

[116] A. Roche, G. Malandain, X. Pennec and N. Ayache. 'The correlation ratio as a new similarity measure for multimodal image registration'. In: *Medical Image Computing and Computer-Assisted Interventation*. Springer, 1998, pp. 1115–1124.

[117] S. Roels, W. Duthoy, K. Haustermans, F. Penninckx, V. Vandecaveye, T. Boterberg and W. De Neve. 'Definition and delineation of the clinical target volume for rectal cancer'. In: *International Journal of Radiation Oncology* Biology* Physics* 65.4 (2006), pp. 1129–1142.

[118] T. Rohlfing, C. R. Maurer Jr, D. A. Bluemke and M. A. Jacobs. 'Volume-preserving nonrigid registration of MR breast images using free-form deformation with an incompressibility constraint'. In: *Medical Imaging, IEEE Transactions on* 22.6 (2003), pp. 730–741.

[119] K Rohr, H. S. Stiehl, R Sprengel, T. M. Buzug, J Weese and M. H. Kuhn. 'Landmark-based elastic registration using approximating thin-plate splines.' In: *IEEE transactions on medical imaging* 20.6 (June 2001), pp. 526–34.

[120] D. Ruan, J. A. Fessler, M. Roberson, J. Balter and M. Kessler. 'Nonrigid registration using regularization that accomodates local tissue rigidity'. In: *Proceedings of SPIE* 6144 (2006), pp. 614412–614412–9.

[121] D Rueckert, L. I. Sonoda, C Hayes, D. L. Hill, M. O. Leach and D. J. Hawkes. 'Nonrigid registration using free-form deformations: application to breast MR images.' In: *IEEE transactions on medical imaging* 18.8 (Aug. 1999), pp. 712–21.

[122] P. Sarma, R. Pidaparti, P. Moulik and R. Meiss. 'Non-linear material models for tracheal smooth muscle tissue'. In: *Bio-medical materials and engineering* 13.3 (Jan. 2003), p. 235.

[123] D. Sarrut, V. Boldea, S. Miguet and C. Ginestet. 'Simulation of four-dimensional CT images from deformable registration between inhale and exhale breath-hold CT scans'. In: *Medical physics* 33 (2006), p. 605.

[124] D. Sarrut, V. Boldea, S. Miguet and C. Ginestet. 'Simulation of four-dimensional CT images from deformable registration between inhale and exhale breath-hold CT scans'. In: *Medical Physics* 33.3 (2006), p. 605.

[125] A. Sawant, R. L. Smith, R. B. Venkat, L. Santanam, B. Cho, P. Poulsen, H. Cattell, L. J. Newell, P. Parikh and P. J. Keall. 'Toward submillimeter accuracy in the management of intrafraction motion: the integration of real-time internal position monitoring and multileaf collimator target tracking'. In: *International Journal of Radiation Oncology* Biology* Physics* 74.2 (2009), pp. 575–582.

[126] M. Schmand, L. Eriksson, M. Casey, M. Andreaco, C. Melcher, K. Wienhard, G. Flügge and R. Nutt. 'Performane results of a new DOI detector block for a High Resulution PET - LSO research Tomograph HRRT'. In: *IEEE transactions on medical imaging* 45.6 (1998), pp. 3000–3006.

[127] R Schulze, U Heil, D Gross, D. D. Bruellmann, E Dranischnikow, U Schwanecke and E Schoemer. 'Artefacts in CBCT: a review'. In: *Dento-maxillofacial Radiology* 40.5 (2011), pp. 265–273.

[128] D. L. Schwartz and L. Dong. 'Adaptive radiation therapy for head and neck cancer-can an old goal evolve into a new standard?' In: *Journal of oncology* 2011 (Jan. 2011).

[129] A. Schweikard, G. Glosser, M. Bodduluri, M. J. Murphy and J. R. Adler. 'Robotic motion compensation for respiratory movement during radiosurgery'. In: *Computer Aided Surgery* 5.4 (2000), pp. 263–277.

[130] Y. Seppenwoolde, R. I. Berbeco, S. Nishioka, H. Shirato and B. Heijmen. 'Accuracy of tumor motion compensation algorithm from a robotic respiratory tracking system: a simulation study'. In: *Medical physics* 34 (2007), p. 2774.

[131] D. Shepard, M. Earl, X. Li, S. Naqvi and C. Yu. 'Direct aperture optimization: a turnkey solution for step-and-shoot IMRT'. In: *Medical physics* 29.6 (2002), pp. 1007–1018.

[132] P. C. Shrimpton, M. C. Hillier, M. A. Lewis and M Dunn. 'National survey of doses from CT in the UK: 2003'. In: *British Journal of Radiology* 79.948 (2006), pp. 968–980.

[133] J. H. Siewerdsen, M. J. Daly, B Bakhtiar, D. J. Moseley, S Richard, H Keller and D. A. Jaffray. 'A simple, direct method for x-ray scatter estimation and correction in digital radiography and cone-beam CT'. In: *Medical physics* 33 (2006), p. 187.

[134] S. M. Smith, M. Jenkinson, M. W. Woolrich, C. F. Beckmann, T. E. J. Behrens, H. Johansen-Berg, P. R. Bannister, M. De Luca, I. Drobnjak and D. E. Flitney. 'Advances in functional and structural MR image analysis and implementation as FSL'. In: *Neuroimage* 23 (2004), S208–S219.

[135] J.-J. Sonke, L. Zijp, P. Remeijer and M. van Herk. 'Respiratory correlated cone beam CT'. In: *Medical physics* 32 (2005), p. 1176.

[136] L. Specht. 'Onkologi'. In: *Basisbog i Medicin & Kirurgi*. Ed. by T. Schroeder, S. Schulze, J. Hilsted and L. Gøtzsche. 5th ed. Munksgaard, 2012, pp. 735–750.

[137] M. K. Stam, S. P. M. Crijns, B. A. Zonnenberg, M. M. Barendrecht, M. van Vulpen, J. J. W. Lagendijk and B. W. Raaymakers. 'Navigators for motion detection during real-time MRI-guided radiotherapy'. In: *Physics in Medicine and Biology* 57.21 (2012), p. 6797.

[138] W. Swindell, R. G. Simpson, J. R. Oleson, C.-T. Chen and E. A. Grubbs. 'Computed tomography with a linear accelerator with radiotherapy applications'. In: *Medical physics* 10 (1983), p. 416.

[139] J.-P. Thirion. 'Image matching as a diffusion process: an analogy with Maxwell's demons'. In: *Medical image analysis* 2.3 (Sept. 1998), pp. 243–260.

[140] S. Turner, R Swindell and N Bowl. 'Bladder movement during radiation therapy for bladder cancer: implications for treatment planning'. In: *International journal of radiation oncology, biology, physics* 3016.February (1997), pp. 355–360.

[141] M. Uematsu, T. Fukui, A. Shioda, H. Tokumitsu, K. Takai, T. Kojima, Y. Asai and S. Kusano. 'A dual computed tomography linear accelerator unit for stereotactic radiation therapy: A new approach without cranially fixated stereotactic frames'. In: *International Journal of Radiation Oncology* Biology* Physics* 35.3 (1996), pp. 587–592.

[142] M. Uematsu, A. Shioda, K. Tahara, T. Fukui, F. Yamamoto, G. Tsumatori, Y. Ozeki, T. Aoki, M. Watanabe and S. Kusano. 'Focal, high dose, and fractionated modified stereotactic radiation therapy for lung carcinoma patients'. In: *Cancer* 82.6 (1998), pp. 1062–1070.

[143] J. Vandemeulebroucke, D. Sarrut and P. Clarysse. 'The POPI-model, a point-validated pixel-based breathing thorax model'. In: *ICCR 2007*. 2007, pp. 1–8.

[144] S. S. Vedam, P. J. Keall, V. R. Kini, H Mostafavi, H. P. Shukla and R Mohan. 'Acquiring a four-dimensional computed tomography dataset using an external respiratory signal.' In: *Physics in medicine and biology* 48.1 (Jan. 2003), pp. 45–62.

[145] S. S. Vedam, P. J. Keall, V. R. Kini, H Mostafavi, H. P. Shukla and R Mohan. 'Acquiring a four-dimensional computed tomography dataset using an external respiratory signal'. In: *Physics in medicine and biology* 48.1 (2003), p. 45.

[146] T. Vercauteren, X. Pennec, A. Perchant and N. Ayache. 'Diffeomorphic demons: efficient non-parametric image registration.' In: *NeuroImage* 45.1 Suppl (Mar. 2009), S61–72.

[147] D. Verellen, M. De Ridder, N. Linthout, K. Tournel, G. Soete and G. Storme. 'Innovations in image-guided radiotherapy.' In: *Nature reviews. Cancer* 7.12 (Dec. 2007), pp. 949–60.

[148] R. Wagman, E. Yorke, E. Ford, P. Giraud, G. Mageras, B. Minsky and K. Rosenzweig. 'Respiratory gating for liver tumors: use in dose escalation'. In: *International Journal of Radiation Oncology* Biology* Physics* 55.3 (2003), pp. 659–668.

[149] C. Walter, J. Boda-Heggemann, H. Wertz, I. Loeb, A. Rahn, F. Lohr and F. Wenz. 'Phantom and in-vivo measurements of dose exposure by image-guided radiotherapy (IGRT): MV portal images vs. kV portal images vs. cone-beam CT'. In: *Radiotherapy and Oncology* 85.3 (2007), pp. 418–423.

[150] J. Wang, T. Li and L. Xing. 'Iterative image reconstruction for CBCT using edge-preserving prior'. In: *Medical physics* 36 (2009), p. 252.

[151] W. M. Wells, P. Viola, H. Atsumi, S. Nakajima and R. Kikinis. 'Multi-modal volume registration by maximization of mutual information'. In: *Medical image analysis* 1.1 (1996), pp. 35–51.

[152] A. P. Witkin. 'Scale-Space Filtering: A New Approach To Multi-Scale Description'. In: *Acoustics, Speech, and Signal Processing, IEEE International Conference on ICASSP* 9 (1984), pp. 150–153.

[153] J. Wolthaus, J. Sonke, M. van Herk, J. Belderbos, M. Rossi, J. Lebesque and E. Damen. 'Comparison of different strategies to use four-dimensional computed tomography in treatment planning for lung cancer patients'. In: *International Journal of Radiation Oncology * Biology * Physics* 70.4 (2008), pp. 1229–1238.

[154] J. Xuan, Y. Wang, M. T. Freedman, T. Adali and P. Shields. 'Nonrigid medical image registration by finite-element deformable sheet-curve models.' In: *International journal of biomedical imaging* 2006.2 (Jan. 2006), p. 73430.

[155] J. Yahalom. 'Transformation in the use of radiation therapy of Hodgkin lymphoma: new concepts and indications lead to modern field design and are assisted by PET imaging and intensity modulated radiation therapy (IMRT)'. In: *European Journal of Haematology* 75.s66 (2005), pp. 90–97.

[156] J. Yun, M. Mackenzie, S. Rathee, D. Robinson and B. G. Fallone. 'An artificial neural network (ANN)-based lung-tumor motion predictor for intrafractional MR tumor tracking.' In: *Medical physics* 39.7 (July 2012), pp. 4423–33.

[157] J. Yun, E. Yip, K. Wachowicz, S. Rathee, M. Mackenzie, D. Robinson and B. G. Fallone. 'Evaluation of a lung tumor autocontouring algorithm for intrafractional tumor tracking using low-field MRI: a phantom study.' In: *Medical physics* 39.3 (Mar. 2012), pp. 1481–94.

[158] R. Zeng, J. a. Fessler and J. M. Balter. 'Estimating 3-D respiratory motion from orbiting views by tomographic image registration.' In: *IEEE transactions on medical imaging* 26.2 (Feb. 2007), pp. 153–63.

[159] Q. Zhang, Y.-C. Hu, F. Liu, K. Goodman, K. E. Rosenzweig and G. S. Mageras. 'Correction of motion artifacts in cone-beam CT using a patient-specific respiratory motion model'. In: *Medical physics* 37 (2010), p. 2901.

[160] J. R. van Sörnsen de Koste, S. Senan, C. E. Kleynen, B. J. Slotman and F. J. Lagerwaard. 'Renal mobility during uncoached quiet respiration: an analysis of 4DCT scans'. In: *International Journal of Radiation Oncology* Biology* Physics* 64.3 (2006), pp. 799–803.